Master's thesis

NTNU
Norwegian University of Science and Technology
Faculty of Information Technology and Electrical Engineering
Department of Engineering Cybernetics

Erling Syversveen Lie

Formation Path Following of Autonomous Underwater Vehicles using the Second-Order Null-Space-Based Behavioral Algorithm

Master's thesis in Cybernetics and Robotics
Supervisor: Kristin Y. Pettersen
Co-supervisor: Josef Matouš
June 2023

NTNU
Norwegian University of
Science and Technology

Erling Syversveen Lie

Formation Path Following of Autonomous Underwater Vehicles using the Second-Order Null-Space-Based Behavioral Algorithm

Master's thesis in Cybernetics and Robotics
Supervisor: Kristin Y. Pettersen
Co-supervisor: Josef Matouš
June 2023

Norwegian University of Science and Technology
Faculty of Information Technology and Electrical Engineering
Department of Engineering Cybernetics

NTNU
Norwegian University of
Science and Technology

Problem description

Introduction: This project aims to develop a method for multi-agent control of Autonomous Underwater Vehicles (AUVs) by combining the 3D hand position concept with a selected multi-agent control algorithm. The goal is to enable accurate formation control, path following, and collision avoidance for AUVs in a multi-agent system.

Objective:

- Perform a literature study on control methods for multi-agent systems with double integrator dynamics, including relevant papers on the 3D hand position concept and multi-agent control algorithms.
- Select a suitable multi-agent control algorithm and integrate it with the 3D hand position concept to develop a control strategy for multi-agent control of AUVs.
- Develop the theory for the combined control method, including stability analysis.
- Conduct simulation studies to validate the effectiveness and performance of the developed control method in formation control, path following, and collision avoidance tasks.

Expected Outcome: The expected outcome of this project is an advanced control method that combines the 3D hand position concept with a selected multi-agent control algorithm to achieve accurate and robust multi-agent control of AUVs. The developed control method will be validated through simulation studies, demonstrating its effectiveness in various scenarios.

Conclusion: By combining the 3D hand position concept with a selected multi-agent control algorithm, this project aims to provide a novel control method for AUVs in a multi-agent system. The proposed method has the potential to significantly enhance the formation control, path following, and collision avoidance capabilities of AUVs, contributing to advancements in autonomous underwater robotics.

Abstract

This thesis presents a novel control law for formation path following with autonomous underwater vehicles (AUVs) using a second-order null-space-based behavioral (NSB) method. AUVs pose unique challenges in formation control due to their nonlinear and underactuated nature. This thesis aims to leverage the input-output linearizing hand-position controller to enable the application of formation control methods designed for double-integrator systems, that would otherwise not be applicable to AUVs.

The main contribution of this work is the extension of the NSB method to directly handle the inherent second-order dynamics of AUVs, addressing the double-integrator nature of the system. By directly accounting for these dynamics, the method eliminates the presence of hidden dynamics from low-level control, encountered in first-order methods. The control algorithm utilizes a hand-position controller that transforms the underactuated six-degrees-of-freedom AUV model into a double-integrator system. The NSB method is a behavioral control algorithm that enables the creation of a hierarchy of prioritized tasks. To solve the formation-path-following problem, we create three tasks: collision avoidance, formation keeping, and path following. The second-order formulation enables the expression of all dynamics directly in task space.

The method is initially developed centralized, closely linked to the first-order NSB methods in the literature. However, due to practical limitations in real-world applications, a novel distributed version of the NSB algorithm is proposed. This distributed method reformulates the formation-keeping task as a consensus problem, enabling different communication topologies without requiring each vehicle to communicate

with all others. The control law leverages techniques from sliding mode control to eliminate errors resulting from non-complete communication graphs.

The closed-loop formation-control and path-following systems are analyzed using Lyapunov theory. The centralized method is shown to give a uniformly semi-globally exponentially stable (USGES) system while the decentralized method is shown to provide trajectories that are ultimately bounded to an arbitrarily small set depending on the approximation of the switching term in the sliding mode controller. With an ideal switching controller, the system is shown to be asymptotically stable.

The method's effectiveness is then demonstrated through extensive MATLAB simulation studies. Both the centralized and distributed methods are tested under a range of different scenarios, and the distributed method is compared with existing methods from the literature. The second-order NSB method is demonstrated to have lower steady-state errors compared to other methods. The results demonstrate the potential of the second-order NSB method for achieving accurate formation control and path following with AUVs.

Sammendrag

Denne oppgaven presenterer en ny styringsmetode for formasjonsbanefølging med autonome undervannsfartøy ved hjelp av en andreordens nullromsbasert atferdsmetode. Autonome undervannsfartøy byr på unike utfordringer innen formasjonsbanefølging på grunn av deres ulineære og underaktuerte natur. Målet med oppgaven er å utnytte inngang-utgang-linearisering ved hjelp av håndposisjonskonseptet for å muliggjøre anvendelse av formasjonsstyringsmetoder som er utviklet for dobbelt-integrator-systemer, som ellers ikke ville vært anvendelige for autonome undervannsfartøy.

Det viktigste bidraget i dette arbeidet er utvidelsen av den nullromsbaserte metoden til å direkte håndtere den iboende andreordens dynamikken til undervannsfartøy gjennom det inngang-utgang lineariserte dobbelt-integrator systemet. Ved å ta hensyn til all dynamikken i oppgaverommet, eliminerer metoden tilstedeværelsen av skjulte dynamikker fra lavnivåkontroll, som man støter på i førsteordens metoder. Styringsmetoden bruker håndposisjonskonseptet for å tranformere den underaktuerte seks-graders-frihet fartøymodellen til et dobbelt-integrator-system. Den nullromsbaserte atferdsmetoden muliggjør opprettelsen av et hierarki av prioriterte oppgaver. For å løse formasjonsbanefølgingsproblemet definerer vi tre oppgaver: kollisjonsungåelse, formasjonsvedlikehold og banefølging. Den andreordens formuleringen av den nullromsbaserte atferdsmetoden muliggjør å uttrykke all dynamikken til systemet direkte i oppgaverommet.

Først utvikles en sentralisert metode som likner mye på de førsteordens nullromsbaserte metodene som allerede finnes i litteraturen. Deretter, på grunn av praktiske

begrensninger i virkelige anvendelser, presenterer vi en ny distribuert versjon av metoden. Denne distribuerte metoden omformulerer formasjonsvedlikeholdsoppgaven som et konsensusproblem, og muliggjør ulike kommunikasjonstopologier uten krav om at hvert fartøy må kommunisere med alle andre. Styringsloven utnytter teknikker fra "sliding mode" regulatorer for å eliminere feil grunnet ukomplett kommunikasjons graf.

Lukket-sløyfe-systemet for formasjonsvedlikehold og baneføIging analyseres ved hjelp av Lyapunov-teori. Vi viser at den sentraliserte metoden gir et uniformt semiglobalt asymptotisk stabilt system, mens løsningene til systemet under den desentraliserte metoden er til slutt avgrenset til et vilkårlig lite område avhengig av valg av approksimasjon av det diskontinuerlige leddet i "sliding mode" regulatoren. Med en ideell diskontinuerlig regulator er systemet asymptotisk stabilt.

Metodens effektivitet demonstreres gjennom omfattende simuleringsstudier i MATLAB. Både den sentraliserte og distribuerte metoden testes under ulike scenarioer, og den distribuerte metoden sammenliknes med eksisterende metoder fra litteraturen. Det demonstreres at den andreordens nullromsbaserte atferdsmetoden har lavere feil i likevekt sammenliknet med andre metoder. Resultatene viser potensialet til den andreordens nullromsbaserte metoden for å oppnå nøyaktig formasjonsbaneføIging for autonome undervannsfartøy.

Contents

List of Tables

List of Figures

Acronyms

ASV autonomous surface vehicle.

AUV autonomous underwater vehicle.

BLF barrier Lyapunov function.

CB center of buoyancy.

CG center of gravity.

CLIK closed-loop inverse kinematics.

COLAV collision avoidance.

DOF degrees-of-freedom.

DUNE Unified Navigation Environment.

GES globally exponentially stable.

LAUV light autonomous underwater vehicle.

LOS line-of-sight.

NED north-east-down.

NSB null-space-based behavioral.

PP pivot point.

ROV remotely operated vehicle.

SOCLIK second-order closed-loop inverse kinematics.

UGAS uniformly globally asymptotically stable.

UGES uniformly globally exponentially stable.

ULES uniformly locally exponentially stable.

USGES uniformly semi-globally exponentially stable.

Preface

This master's thesis is submitted as a part of the requirements for the master's degree at the Department of Engineering Cybernetics at the Norwegian University of Science and Technology. The work presented in this thesis has been carried out under the supervision of Prof. Kristin Y. Pettersen and Ph.D. candidate Josef Matouš at the Department of Engineering Cybernetics, NTNU.

During the project, I have been provided Simulink models for the 6-DOF hand-position controller and the first-order NSB method by Josef Matouš. The Simulink models as well as the included MATLAB code served as a foundation for the Matlab simulator used in Chapter 10. The simulator was modified and extended to combine both the centralized and decentralized NSB methods with the hand-position controller.

Unless otherwise stated, all figures and illustrations have been created by the author, however, the SVG object for the yellow AUVs found in several of the figures was provided by Josef Matouš.

I would like to thank my supervisors Kristin Y. Pettersen and Josef Matouš for providing advice throughout my thesis. Their expertise and feedback have been instrumental in shaping the direction and quality of this work. I would also like to extend my appreciation to my friends for their support, and encouragement, and for being a source of motivation throughout my academic journey. Their presence and willingness to listen have made the last five years of university truly enjoyable.

Erling Syversveen Lie
Trondheim, June 2023

Chapter 1

Introduction

This introductory chapter motivates the work by discussing the various applications of cooperating autonomous underwater vehicles (AUVs). The formation path-following problem is motivated, and limitations posed on existing methods by the nonlinear equations of motion are discussed. The thesis problem is further motivated by briefly discussing the features of the hand-position controller and its possible applications. Then, a literature study on formation control methods for double-integrator systems is presented. These methods are viable candidates to be combined with the hand-position controller. The main contributions are listed and the chapter is concluded with an outline of the rest of the thesis.

1.1 Motivation

AUVs have become increasingly important for ocean research and exploration. AUVs are able to perform tasks in harsh and remote environments that may be too dangerous or difficult for human divers, such as collecting data on ocean temperatures, salinity, and currents, mapping the ocean floor, and conducting underwater inspections for the oil and gas industry. They have also been used for studying marine biology and geosciences (Das et al.; 2015; Wynn et al.; 2014). The use of AUVs has the potential to

significantly improve our understanding of the ocean and its processes, as well as aid in the development of sustainable ocean practices. Unlike remotely operated vehicles (ROVs), AUVs are not tethered to the research vessel they are deployed from, which enables opportunities for explorations in areas that were previously inaccessible, such as beneath the ice in polar regions (Dowdeswell et al.; 2008).

The cooperation of multiple AUVs can enhance their capabilities and enable them to perform tasks that are difficult or impossible for a single AUV to accomplish. Cooperation among AUVs can increase mission efficiency, allows the exploration of larger areas, and provide redundancy in case of system failures. One example is the use of fleets of AUVs for oceanographic studies as mobile sensor networks (Leonard et al.; 2007). Other applications include the use of multiple AUVs for the inspection of underwater structures or pipelines, in which each vehicle can be equipped with sensors and work together to cover a larger area more quickly.

Our work concerns the multi-agent formation path-following problem. The vehicles are controlled to follow a desired path while keeping a predefined formation. The path can be preplanned or it can be provided by a higher-level control layer. Formation path following can be achieved using numerous different control strategies, including leader-follower approaches, where one AUV acts as a leader and the others follow its trajectory (Soorki et al.; 2011; Cui et al.; 2010; Wang et al.; 2009), distributed path-following approaches using consensus algorithms (Skjetne et al.; 2002; Ghabcheloo et al.; 2006; Borhaug and Pettersen; 2006), and behavioral approaches that define the behaviors each AUV should exhibit to achieve a desired formation (Monteiro and Bicho; 2002; Balch and Arkin; 1998).

What makes formation path following with AUVs especially complex compared to ground vehicles are the nonlinear underactuated dynamics. The dynamic constraints must be taken into account when designing formation-control algorithms for the systems to remain stable. The nonlinear and underactuated dynamics make many existing formation-control algorithms developed for other types of vehicles impossible or difficult to apply to AUVs. A promising approach is to use a hand-position input-output linearizing controller to transform the nonlinear equations into kinematic double-integrator systems (Matouš, Paliotta, Pettersen and Varagnolo; 2023; Paliotta

et al.; 2019), which may enable the application of a varied number of control strategies that could otherwise not be applied directly to AUVs. Restrepo et al. (2022) successfully applied an edge-agreement-based distributed formation control law to 3-degrees-of-freedom (DOF) autonomous surface vehicles (ASVs), using the hand-position to transfer the ASV models into linear double-integrator dynamics. In this thesis, we will further explore formation control algorithms for multi-agent systems with double-integrator dynamics. We first present a literature study of control methods and then develop a formation control algorithm for double-integrator systems based on the null-space-based behavioral (NSB) control method.

1.2 Literature review

This section presents a literature study on control methods for multi-agent systems with double-integrator dynamics. The methods can be grouped into three main categories: consensus-based methods, rigidity-based methods, and NSB methods.

Various consensus algorithms have been proposed to solve the formation-keeping problem in double-integrator systems. The consensus problem is a problem in which multiple agents must coordinate to reach a common value in some information state. The information state can be for instance position, velocity, or a path-progress parameter. The formation path-following problem can be considered a special case of the consensus problem with the following objective:

$$\lim_{t\to\infty} \mathbf{p}_i(t) - \mathbf{p}_j(t) - \mathbf{d}_{ij} = \mathbf{0}, \quad \lim_{t\to\infty} \mathbf{v}_i(t) - \mathbf{v}_j(t) = \mathbf{0}, \tag{1.1}$$

where $\mathbf{p}_i$ and $\mathbf{v}_i$ are the position and velocity vectors for vehicle i and d_{ij} is the desired relative displacement between vehicle i and j. For double-integrator systems, the general consensus controller will take the form

$$\dot{\mathbf{p}}_i = \mathbf{v}_i, \tag{1.2a}$$

$$\dot{\mathbf{v}}_i = \boldsymbol{\mu}_i \tag{1.2b}$$

$$\boldsymbol{\mu}_i = -k_1 \sum_{j\in\mathcal{N}_i} (\mathbf{p}_i - \mathbf{p}_j - \mathbf{d}_{ij}) - k_2 \sum_{j\in\mathcal{N}_i} (\mathbf{v}_i - \mathbf{v}_j), \tag{1.2c}$$

where k_1 and k_2 are constant controller gains and $\mathcal{N}_i$ is the set of all neighboring agents of agent i. Specific consensus algorithms can typically take slightly different forms depending on the goal, but will generally keep terms based on the difference in position and velocity with neighboring vehicles. A review of general consensus problems is found in Ren et al. (2005).

Restrepo et al. (2022) developed a consensus control law that works directly with ASVs and AUVs equipped with the hand-position controller moving in the horizontal plane. It combines techniques from integrator backstepping, barrier Lyapunov functions (BLFs), and sliding-mode-like switching control. While the paper primarily addresses the tracking of an external target vehicle, it can easily be adapted to track a predefined trajectory using a virtual target. The method can be applied to path following by employing a leader-follower scheme, where the leader controls the progress along the path while the other vehicles act as followers. Moreover, in addition to addressing formation keeping and target tracking, the method explicitly tackles collision avoidance and the maintenance of a maximum communication range. The communication between neighboring agents is assumed to be undirected, allowing bidirectional information flow.

Other consensus algorithms for control of multi-agent systems subject to double-integrator dynamics share many commonalities with each other. For instance, in Miao and Wang (2019), a consensus algorithm is proposed in which a controller utilizes the gradient of a potential field to maintain communication radius, resembling the concept of BLFs in Restrepo et al. (2022). Despite using different notations, the control methods in both papers exhibit clear similarities. Furthermore, in Montañez-Molina et al. (2022), a consensus algorithm is presented for formations with directed communication, employing a backstepping-like controller. Additionally, Girejko and Malinowska (2019) introduces a leader-follower tracking consensus controller with a virtual leader. In Mohammadi et al. (2021), a leader-follower tracking controller is proposed, where positions and velocities of the leader and other agents are estimated instead of being precisely known. Similar to Restrepo et al. (2022), a switching controller is applied to handle estimate uncertainties.

A different category of formation control methods is rigidity-based methods. Cai

and Queiroz (2015) proposed a graph rigidity-based adaptive formation control law for vehicles moving in the plane. The robots' dynamics are modeled using Euler-Lagrange-like equations of motion and simplified using the hand position as the system output. The backstepping-based control law with inter-agent distances as controlled variables ensures asymptotic convergence to the desired formation without global position measurements. The rigid graph theory ensures the uniqueness of the formation shape under distance constraints. Because the method is adaptive, it allows for parametric uncertainty. Li et al. (2021) formulate a similar method, but based on a bearing-rigid graph instead of a distance-rigid graph. They argue that bearing-only-based control methods have strong appeal due to the natural connection with vision-based control problems.

A third category of formation-control methods is the NSB method. The method has so far been developed for multi-agent control of vehicles following single-integrator dynamics, but, as will be shown throughout this thesis, the method can be modified to work with double-integrator dynamics instead. The method was developed for 3-DOF ASVs in Arrichiello et al. (2006), and has been applied in various other works (Pereda et al.; 2011; Arrichiello et al.; 2010; Eek et al.; 2021). It was extended for AUVs moving in 6-DOF in Matouš, Pettersen, Varagnolo and Paliotta (2023b). The main idea is to formulate a prioritized hierarchy of tasks the vehicle should follow in order to exhibit the desired behavior. The desired velocities generated by the lower-priority tasks are projected into the null space of the higher-priority tasks so that they are only satisfied within the subspace where they do not conflict.

1.3 Contributions

This thesis presents a novel control method for the formation path-following problem with AUVs. The main contributions can be summarized as follows:

- A literature review on multi-agent control methods for systems following double-integrator dynamics.
- An extended second-order NSB control method that works directly with double-

integrator dynamics.

- An extension to the specific behavioral tasks developed in Matouš, Pettersen, Varagnolo and Paliotta (2023b) to work at the acceleration level to be compatible with the second-order NSB method.
- A closed-loop stability analysis of the joint formation-control and path-following system with the extended NSB controller.
- A novel approach to reformulating the NSB algorithm into a distributed method.
- A closed-loop stability analysis of the proposed distributed NSB method.
- An extensive MATLAB simulation study of the centralized and decentralized second-order NSB method.
- A submitted conference paper to the 62nd IEEE Conference on Decision and Control with the initial results of the centralized second-order NSB method (Lie et al.; 2023).

In this work, we develop an extended NSB method for vehicles with double-integrator dynamics and propose an algorithm that uses a second-order closed-loop inverse kinematics (SOCLIK) equation to control the task variables through acceleration inputs. The procedure is inspired by robotic manipulators, where second-order methods are more common, due to the inherent second-order dynamics of mechanical systems (Siciliano et al.; 2009; Chiaverini et al.; 2008). Although existing NSB methods are developed for first-order systems, AUV dynamics are inherently second-order. Therefore, any first-order solution is necessarily perturbed by the dynamics of the maneuvering controller. In contrast, our formulation handles the second-order dynamics directly in the task space as interpretable spring-damper systems.

We apply the 3D hand position method proposed in Matouš, Paliotta, Pettersen and Varagnolo (2023), which transforms the underactuated six-degrees-of-freedom AUV model into a double-integrator system. The transformation enables us to develop the formation-control algorithm for simple kinematic point systems. Subsequently, through the design of specific path-following, formation-keeping, and

collision-avoidance tasks, the fleet is controlled to follow a preplanned path in formation while avoiding collisions both within the fleet and with external obstacles. Because our reformulated NSB method works directly with the second-order system given by the hand position controller, there is no need to transform desired velocities or accelerations into surge and orientation references, as has been done in previous works. Thus, the complexity level of the control design is reduced.

We review two different methods for compensating for unknown ocean currents. The stability of the system under both ocean current compensation methods is studied when the collision avoidance task is inactive. Two methods for external obstacle avoidance are developed for the double-integrator formulation. The first enables the fleet to avoid obstacles as one unit, keeping formation throughout the avoidance maneuver. In the second method, the vehicles are allowed to break formation in order to avoid collisions.

The NSB method is inherently centralized, meaning there must be a central node that communicates and coordinates with all the vehicles in the fleet. We develop a novel decentralized reformulation of the NSB algorithm. The key insight lies in reformulating the formation-keeping task as a consensus algorithm. Our resulting distributed method requires inter-vehicle communication of a path progress parameter as well as measurements of relative positions and velocities with neighboring vehicles. The proposed control law uses a sliding mode term in the formation-keeping subcontroller to eliminate formation-keeping errors introduced by the path-following task under non-complete communication graphs.

The closed-loop system is analyzed under both the centralized and the decentralized control law. We demonstrate that the formation-keeping and path-following subsystems can be analyzed independently, and analyze the stability for each of them using Lyapunov theory. The system is shown to be uniformly semi-globally exponentially stable (USGES) under the centralized controller, whereas the decentralized controller ensures that the trajectories of the system remain bounded when the sliding-mode controller is approximated with a saturation function. With the ideal switching controller, the system is shown to be asymptotically stable.

We provide an extensive set of MATLAB simulation studies, in which both the

centralized and decentralized NSB methods are tested under different scenarios. The centralized method is tested with two different obstacle avoidance approaches. The decentralized method is first simulated in a general scenario and then compared to two other existing formation path-following methods from the literature. The MATLAB code for one of the external works was handed to us, while we implemented the other controller ourselves following details in the paper.

1.4 Outline

The report is organized as follows. In Chapter 2, the mathematical AUV model is presented, as well as all necessary assumptions. Chapter 3 presents the 3D hand-position input-output linearization method which transforms the highly non-linear equations of motion of the underactuated vehicles into a double-integrator system in position. Chapter 4 introduces notation, assumptions, and mathematical tools for formation path following of fleets of AUVs. The chapter introduces the mathematical description of a path as a continuous, differentiable parametric function, and it defines the fleet formation as a set of reference vectors relative to the barycenter of the fleet. The chapter also introduces some simple graph theory, which serves as a basis for the development of the distributed NSB method. In Chapter 5, background theory for the NSB algorithm is presented before the general NSB method for second-order systems is developed as a natural extension of the first-order NSB method. Chapter 6 presents the centralized NSB method. Collision-avoidance, formation-keeping, and path-following tasks are developed for the second-order formulation so that the task solution provides desired accelerations. Then, modifications to the tasks that enable the fleet to compensate for unknown ocean currents and avoid external obstacles are presented. In Chapter 7, the closed loop properties of the centralized control algorithm presented in Chapter 6 are studied. In Chapter 8, the NSB method is modified to work in a distributed setting. The closed-loop stability analysis for this method is provided in Chapter 9. Both the centralized and decentralized control algorithms are simulated in various configurations in MATLAB (The MathWorks Inc.; 2022) in Chapter 10. Finally, Chapter 11 presents conclusions and future work.

Chapter 2

Vehicle Model

This chapter presents the notation and assumptions for the vehicle models in this work. Because the high-level goal of the thesis is to study multi-agent control algorithms suitable to combine with the 3D hand-position method presented in Chapter 3, the assumptions on the vehicle models will be similar to those of the original 3D hand-position paper (Matouš, Paliotta, Pettersen and Varagnolo; 2023).

We consider a standard six-degrees-of-freedom AUV model with an unknown irrotational current. The position of the vehicle in the north-east-down (NED) coordinate frame is denoted by $\boldsymbol{\eta} \in \mathbb{R}^3$, the attitude is parameterized using a rotation matrix $\mathbf{R} \in SO(3)$, and the translational and rotational velocities in the vehicle's body-fixed coordinate frame are denoted by $\boldsymbol{\nu} \in \mathbb{R}^3$ and $\boldsymbol{\omega} \in \mathbb{R}^3$, respectively.

The AUV is affected by an unknown constant irrotational ocean current $\mathbf{v}_c \in \mathbb{R}^3$. We define the relative velocity between the AUV and the current as $\boldsymbol{\nu}_r = \boldsymbol{\nu} - R^{\mathrm{T}}\mathbf{v}_c$, and the concatenated velocity vector as $\boldsymbol{\zeta}_r^{\mathrm{T}} = [\boldsymbol{\nu}_r^{\mathrm{T}}, \boldsymbol{\omega}^{\mathrm{T}}]$. The AUV is subject to external forces and moments due to hydrodynamic forces, gravitational forces, and control inputs. We assume that we can control the surge thrust and torque around all three axes, and denote the control input vector $\mathbf{f} = [T_u, T_p, T_q, T_r]^{\mathrm{T}}$, where T_u is the surge thrust and T_p, T_q, T_r denote the torques produced by the fins. The AUV dynamics can

be written as follows (Fossen; 2021):

$$\dot{\boldsymbol{\eta}} = \mathbf{R}\boldsymbol{\nu}_r + \mathbf{v}_c, \tag{2.1a}$$

$$\dot{\mathbf{R}} = \mathbf{R}\mathbf{S}(\boldsymbol{\omega}), \tag{2.1b}$$

$$\mathbf{M}\dot{\boldsymbol{\zeta}}_r + \mathbf{C}(\boldsymbol{\zeta}_r)\boldsymbol{\zeta}_r + \mathbf{D}(\boldsymbol{\zeta}_r)\boldsymbol{\zeta}_r + \mathbf{g}(\mathbf{R}) = \mathbf{B}\mathbf{f}, \tag{2.1c}$$

where $\mathbf{M} \in \mathbb{R}^{6\times6}$ is the mass and inertia matrix, $\mathbf{C}(\boldsymbol{\zeta}_r) \in \mathbb{R}^{6\times6}$ is the Coriolis and centripetal matrix, $\mathbf{D}(\boldsymbol{\zeta}_r) \in \mathbb{R}^{6\times6}$ is the hydrodynamic damping matrix, $\mathbf{g}(\mathbf{R}) \in \mathbb{R}^6$ represents the gravitational and buoyancy forces, $\mathbf{B} \in \mathbb{R}^{4\times6}$ is the control allocation matrix, and $\mathbf{S} : \mathbb{R}^3 \mapsto \mathfrak{so}(3)$ is the skew-symmetric matrix operator. Note that for any two vectors $\mathbf{a}, \mathbf{b} \in \mathbb{R}^3$, it follows that $\mathbf{S}(\mathbf{a})\mathbf{b} = \mathbf{a} \times \mathbf{b}$, where $\times$ is the vector cross product.

Next, we present the modeling assumptions.

Assumption 2.1. *The vehicle is slender, torpedo-shaped with port-starboard and top-bottom symmetry.*

Assumption 2.2. *The vehicle is neutrally buoyant, with the center of gravity (CG) and center of buoyancy (CB) on the same vertical axis. The distance from CB to CG is given by the positive constant z_{bg}, meaning the center of gravity is located below the center of buoyancy.*

Assumption 2.3. *The origin of the body-fixed coordinate frame is located at neutral point (also commonly referred to as pivot point (PP)) which has relative position $[x_o,\ 0,\ 0]^T$ from the center of gravity, with x_o such that the actuators produce no sway or heave acceleration. Then, there exist $f_u,\ t_p,\ t_q$, and t_r such that*

$$\mathbf{M}^{-1}\mathbf{B}\mathbf{f} = [f_u,\ 0,\ 0,\ t_p,\ t_q,\ t_r]^T. \tag{2.2}$$

It was shown in Borhaug et al. (2007) that there exists a coordinate transformation that satisfies (2.2) for a 5-DOF model satisfying Assumption 2.1. The result is trivially extended to 6-DOF because roll is decoupled from the other degrees of freedom under

Assumption 2.1. The coefficients ϵ_1 and ϵ_2 are defined as

$$\epsilon_1 \triangleq -\frac{m_{55}b_{23} - m_{25}b_{53}}{m_{22}b_{53} - m_{25}b_{23}}, \quad \epsilon_2 \triangleq -\frac{m_{44}b_{32} - m_{34}b_{42}}{m_{33}b_{42} - m_{34}b_{32}}, \tag{2.3}$$

where m_{ij} and b_{ij} are the elements on row i, column j of M and B, respectively. The coordinate transformation matrix to the pivot point from the existing coordinate origin (CO) is then given by the matrix $\mathbf{H}_{PP}$ such that $\boldsymbol{\zeta}_r^{PP} = \mathbf{H}_{PP}\boldsymbol{\zeta}_r^{CO}$:

$$\mathbf{H}_{PP} = \begin{bmatrix} 1 & 0 & 0 & 0 & 0 & 0 \\ 0 & 1 & 0 & 0 & 0 & -\epsilon_1 \\ 0 & 0 & 1 & 0 & -\epsilon_2 & 0 \\ 0 & 0 & 0 & 1 & 0 & 0 \\ 0 & 0 & 0 & 0 & 1 & 0 \\ 0 & 0 & 0 & 0 & 0 & 1 \end{bmatrix}. \tag{2.4}$$

We note that for most cylindrical-shaped AUVs, $\epsilon_1 = -\epsilon_2$. Then $\mathbf{H}_{PP}$ corresponds to a physical translation of the coordinate origin along the x-axis of the ship as detailed in (Fossen; 2021, Appendix C). The points of interest from Assumption 2.2 and 2.3 are illustrated in Figure 2.1.

Assumption 2.4. *The AUV is operating at sufficiently fast ocean-current relative speeds so that it remains fully controllable.*

Because the torques are produced by fins attached to the AUV, the vehicle must maintain a minimum ocean current-relative velocity to remain controllable.

Assumption 2.5. *The AUV is operating at sufficiently slow speeds so that the hydrodynamic damping can be considered linear.*

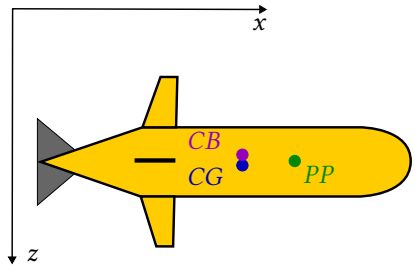

Figure 2.1: Illustration of the AUV with different points of interest. The marked points are the center of gravity (CG), the center of buoyancy (CB), and the pivot point (PP). The coordinate axes show the orientation of the body-fixed coordinate system, however, the origin would be at the pivot point according to Assumption 2.3.

The structure of the matrices **M**, **B**, and **D** under Assumptions 2.1, 2.3, and 2.5 are

$$\mathbf{M} = \begin{bmatrix} m_{11} & 0 & 0 & 0 & 0 & 0 \\ 0 & m_{22} & 0 & 0 & 0 & m_{26} \\ 0 & 0 & m_{33} & 0 & m_{35} & 0 \\ 0 & 0 & 0 & m_{44} & 0 & 0 \\ 0 & 0 & m_{35} & 0 & m_{55} & 0 \\ 0 & m_{26} & 0 & 0 & 0 & m_{66} \end{bmatrix}, \tag{2.5a}$$

$$\mathbf{B} = \begin{bmatrix} b_{11} & 0 & 0 & 0 \\ 0 & 0 & 0 & b_{24} \\ 0 & 0 & b_{33} & 0 \\ 0 & b_{42} & 0 & 0 \\ 0 & 0 & b_{53} & 0 \\ 0 & 0 & 0 & b_{64} \end{bmatrix}, \tag{2.5b}$$

$$\mathbf{D} = \begin{bmatrix} d_{11} & 0 & 0 & 0 & 0 & 0 \\ 0 & d_{22} & 0 & 0 & 0 & d_{26} \\ 0 & 0 & d_{33} & 0 & d_{35} & 0 \\ 0 & 0 & 0 & d_{44} & 0 & 0 \\ 0 & 0 & d_{53} & 0 & d_{55} & 0 \\ 0 & d_{62} & 0 & 0 & 0 & d_{66} \end{bmatrix}. \tag{2.5c}$$

Assumption 2.6. *The effect of gravity and buoyancy on the linear velocities is negligible.*

Therefore, under Assumptions 2.2 and 2.6, the following approximation

$$\mathbf{M}^{-1}\mathbf{g}(\mathbf{R}) \approx \begin{bmatrix} 0_3 \\ \mathbf{M}'_{22}(W z_{bg} \mathbf{e}_3 \times R^T \mathbf{e}_3) \end{bmatrix} \tag{2.6}$$

can be used to simplify dynamics, where $\mathbf{M}'_{22}$ is the lower right part of M^{-1}, and $\mathbf{e}_3 = [0,\ 0,\ 1]^T$ is the third axis unit vector.

Assumption 2.7. *The full state* $\{\boldsymbol{\eta},\ \mathbf{R},\ \boldsymbol{\zeta}_r\}$ *is available for feedback.*

We do not consider the state estimation problem and assume that the full state is available for feedback.

Chapter 3

Hand Position Transformation

This chapter details the hand-position input-output feedback linearization transformation used herein to transform the non-linear underactuated AUV model (2.1) to a double-integrator with a constant ocean-current velocity disturbance.

The hand position concept was first introduced in Pomet et al. (1992) to stabilize nonholonomic vehicles with unicycle dynamics. The method was extended to marine vehicles moving in the horizontal plane by Paliotta et al. (2019), which was then used as the basis for a formation control method in Restrepo et al. (2022). The method was further extended to 6-DOF underwater vehicles in Matouš, Paliotta, Pettersen and Varagnolo (2023). In this chapter, we will present the method as derived for AUVs.

The linearization involves choosing the hand-position point as the system's output. The hand-position point is located a given distance from the vehicle's pivot point along the x-axis. Figure 3.1 illustrates an AUV with the center of gravity, pivot point, and hand-position point marked. With reference to the AUV equations of motion (2.1), the hand-position point is defined in terms of the following change of coordinates:

$$\mathbf{p} = \boldsymbol{\eta} + \mathbf{R}\mathbf{L}, \tag{3.1a}$$

$$\mathbf{v} = \mathbf{R}\boldsymbol{\nu}_r + \mathbf{R}(\boldsymbol{\omega} \times \mathbf{L}), \tag{3.1b}$$

where $\mathbf{L} = [h, 0, 0]^{\mathrm{T}}$ and $h > 0$ is the hand length.

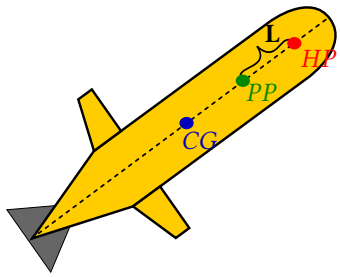

Figure 3.1: Illustration of the AUV with different points of interest. The marked points are the center of gravity (CG), pivot point (PP), and hand-position point (HP). Additionally, the hand length **L** is marked. The dashed line illustrates the vehicle's center line, which contains all the points of interest.

To derive the feedback linearized equations of motion, we first introduce some notation. Let

$$\mathbf{M}^{-1} = \begin{bmatrix} \mathbf{M}'_{11} & \mathbf{M}'_{12} \\ \mathbf{M}'_{21} & \mathbf{M}'_{22}, \end{bmatrix} \tag{3.2}$$

and

$$\begin{bmatrix} \mathcal{D}_\nu \\ \mathcal{D}_\omega \end{bmatrix} = \mathbf{M}^{-1}\mathbf{D}(\zeta_r)\zeta_r, \quad \begin{bmatrix} C_\nu \\ C_\omega \end{bmatrix} = \mathbf{M}^{-1}\mathbf{C}(\zeta_r)\zeta_r. \tag{3.3}$$

Then, we can rewrite (2.1c) in the following form

$$\dot{\boldsymbol{\nu}}_r = [f_u, 0, 0]^{\mathrm{T}} - \mathcal{D}_\nu(\zeta_r) - C_\nu(\zeta_r), \tag{3.4a}$$

$$\dot{\boldsymbol{\omega}} = [t_p, t_q, t_r]^{\mathrm{T}} - \mathcal{D}_\omega(\zeta_r) - C_\omega(\zeta_r) - \mathbf{M}'_{22}\left(W z_{bg}\mathbf{e}_3 \times R^{\mathrm{T}} e_3\right). \tag{3.4b}$$

Differentiating (3.1) with respect to time and inserting for (3.4) yields:

$$\dot{\mathbf{p}} = \mathbf{v} + \mathbf{v}_c, \tag{3.5a}$$

$$\begin{aligned}\dot{\mathbf{v}} &= \mathbf{R}\left(\dot{\boldsymbol{\nu}}_r + \boldsymbol{\omega} \times \boldsymbol{\nu}_r + \dot{\boldsymbol{\omega}} \times \mathbf{L} + \boldsymbol{\omega} \times (\boldsymbol{\omega} \times \mathbf{L})\right), \\ &= \mathbf{R}\Big([f_u, ht_r, -ht_q]^{\mathrm{T}} - \mathcal{D}_{\boldsymbol{\nu}}(\boldsymbol{\zeta}_r) - C_{\boldsymbol{\nu}}(\boldsymbol{\zeta}_r) + \boldsymbol{\omega} \times \boldsymbol{\nu}_r \\ &\quad + \mathbf{L} \times \left(\mathcal{D}_{\boldsymbol{\omega}}(\boldsymbol{\zeta}_r) + C_{\boldsymbol{\omega}}(\boldsymbol{\zeta}_r) + \mathbf{M}'_{22}\left(W z_{bg} \mathbf{e}_3 \times R^{\mathrm{T}} e_3\right)\right) + \boldsymbol{\omega} \times (\boldsymbol{\omega} \times \mathbf{L})\Big).\end{aligned} \tag{3.5b}$$

We note that $\dot{\mathbf{v}}$ is independent of the roll torque t_p. Therefore, t_p is used independently to stabilize the roll dynamics by canceling the Coriolis effect

$$t_p = \mathbf{e}_1^{\mathrm{T}} C_{\boldsymbol{\omega}}(\boldsymbol{\zeta}_r). \tag{3.6}$$

The following change of input linearizes the output dynamics (3.5):

$$\begin{aligned}\begin{bmatrix} f_u \\ t_q \\ t_r \end{bmatrix} = \begin{bmatrix} 1 & 0 & 0 \\ 0 & 0 & -\frac{1}{h} \\ 0 & \frac{1}{h} & 0 \end{bmatrix} \Big(&\mathbf{R}^{\mathrm{T}} \boldsymbol{\mu} + \mathcal{D}_{\boldsymbol{\nu}}(\boldsymbol{\zeta}_r) + C_{\boldsymbol{\nu}}(\boldsymbol{\zeta}_r) - \boldsymbol{\omega} \times \boldsymbol{\nu}_r \\ &- \mathbf{L} \times \left(\mathcal{D}_{\boldsymbol{\omega}}(\boldsymbol{\zeta}_r) + C_{\boldsymbol{\omega}}(\boldsymbol{\zeta}_r) + \mathbf{M}'_{22}\left(W z_{bg} \mathbf{e}_3 \times \mathbf{R}^{\mathrm{T}} \mathbf{e}_3\right)\right) \\ &- \boldsymbol{\omega} \times (\boldsymbol{\omega} \times \mathbf{L}) \Big),\end{aligned} \tag{3.7}$$

where $\boldsymbol{\mu} \in \mathbb{R}^3$ is the new control input. The resulting output feedback linearized system is given by:

$$\dot{\mathbf{p}} = \mathbf{v} + \mathbf{v}_c, \tag{3.8a}$$

$$\dot{\mathbf{v}} = \boldsymbol{\mu}, \tag{3.8b}$$

$$\dot{\mathbf{R}} = \mathbf{R}\mathbf{S}(\boldsymbol{\omega}), \tag{3.8c}$$

$$\begin{aligned}\dot{\boldsymbol{\omega}} &= \mathbf{f}_0(\boldsymbol{\mu}, \boldsymbol{\omega}, \mathbf{R}, \mathbf{v}) \\ &= \bar{\mathbf{L}} \times \left(\mathbf{R}^T \boldsymbol{\mu} + \mathcal{D}_{\boldsymbol{\nu}}(\boldsymbol{\zeta}_r) + C_{\boldsymbol{\nu}}(\boldsymbol{\zeta}_r) - \boldsymbol{\omega} \times \mathbf{R}^T \mathbf{v}\right) \\ &\quad - \left(\bar{\mathbf{L}} \mathbf{L}^T\right) \left(\mathcal{D}_{\boldsymbol{\omega}}(\boldsymbol{\zeta}_r) + \mathbf{M}'_{22}(W \mathbf{z}_{gb} \mathbf{e}_3 \times \mathbf{R}^T \mathbf{e}_3)\right),\end{aligned} \tag{3.8d}$$

where $\bar{\mathbf{L}} = [1/h,\ 0,\ 0]^T$, $[\mathbf{p}, \mathbf{v}]^{\mathrm{T}}$ is the external part of the system and $[\mathbf{R},\ \boldsymbol{\omega}]^{\mathrm{T}}$ is the internal part. The dynamics of the external part of the system are linear, with the ocean current as an unknown disturbance. Because the internal dynamics (3.8d) are affected by the input $\boldsymbol{\mu}$, the internal stability properties of $\mathbf{R}$ and $\boldsymbol{\omega}$ must be verified for the specific choice of control law for $\boldsymbol{\mu}$.

Chapter 4

Formation Path-Following

The main objective of this work is to study control methods for multi-agent systems. Specifically, the work herein aims to examine existing methods and develop new methods for the formation path following of fleets of AUVs. This chapter will introduce the necessary assumptions for the paths, the relevant coordinate frames, and the notation used herein to describe fleets of AUVs.

4.1 Equations of motion and coordinate frames

We consider a fleet of n AUVs equipped with output-feedback-linearization hand-position controllers. Each vehicle follows the equations of motion (3.8). We define the stacked position, velocity, and control input vectors of the fleet $\mathbf{p} = [\mathbf{p}_1^\mathrm{T}, \ldots, \mathbf{p}_n^\mathrm{T}]^\mathrm{T}$, $\mathbf{v} = [\mathbf{v}_1^\mathrm{T}, \ldots, \mathbf{v}_n^\mathrm{T}]^\mathrm{T}$, and $\boldsymbol{\mu} = [\boldsymbol{\mu}_1^\mathrm{T}, \ldots, \boldsymbol{\mu}_n^\mathrm{T}]^\mathrm{T}$, respectively. We also define the stacked ocean current vector $\mathbf{V}_c = \mathbf{1}_{n,1} \otimes \mathbf{v}_c$, where $\mathbf{1}_{n,1}$ is an n-dimensional vector of ones, and $\otimes$ is the Kronecker product. The translational motion of the whole fleet can then be described in terms of the stacked variables

$$\dot{\mathbf{p}} = \mathbf{v} + \mathbf{V}_c, \tag{4.1a}$$

$$\dot{\mathbf{v}} = \boldsymbol{\mu}. \tag{4.1b}$$

The formation path-following objective will involve controlling the barycenter $\mathbf{p}_b$ of the fleet to follow a predetermined path. The barycenter is defined as follows:

$$\mathbf{p}_b = \frac{1}{n}\sum_{i=1}^{n} \mathbf{p}_i. \tag{4.2}$$

We let the path be given by a continuous parametric function $\mathbf{p}_p(\xi) : \mathbb{R} \mapsto \mathbb{R}^3$. The path is assumed to be smooth and regular, meaning that it is infinitely differentiable and the partial derivative with respect to ξ satisfies $\left\| \frac{\partial \mathbf{p}_p(\xi)}{\partial \xi} \right\| \neq 0$.

For every point $\mathbf{p}_p(\xi)$, there exists a path-tangential coordinate frame with a corresponding rotation matrix $\mathbf{R}_p$. The path-following error $\mathbf{p}_b^p$ is defined in terms of the barycenter of the fleet in the path-tangential coordinate frame:

$$\mathbf{p}_b^p = \mathbf{R}_p^{\mathrm{T}} \left(\mathbf{p}_b - \mathbf{p}_p(\xi) \right). \tag{4.3}$$

The formation is defined in the formation-centered coordinate frame, centered at $\mathbf{p}_b$ with the same orientation as the path-tangential frame. The position of a vehicle in the formation-centered frame is given by

$$\mathbf{p}_i^f = \mathbf{R}_p^{\mathrm{T}} \left(\mathbf{p}_i - \mathbf{p}_b \right), \tag{4.4}$$

and the desired positions are given by $\mathbf{p}_{f,1}^f, \ldots, \mathbf{p}_{f,n}^f$. By definition of $\mathbf{p}_b$, the following constraint always holds

$$\sum_{i=1}^{n} \mathbf{p}_i^f = \mathbf{0}. \tag{4.5}$$

Consequently, $n-1$ desired barycenter-relative positions $\mathbf{p}_{f,i}^f$ are sufficient to uniquely specify the formation, because the final vehicle's position is implied by (4.5). The formation is illustrated in Figure 4.1.

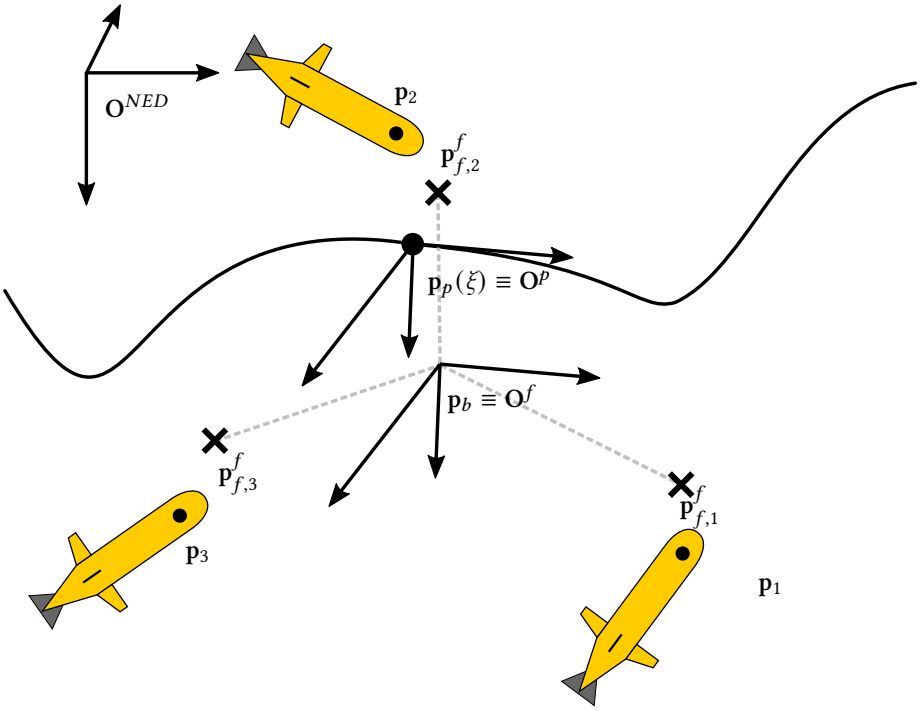

Figure 4.1: Definition of the formation. $\mathbf{O}^f$ denotes the origin of the formation-centered coordinate frame, $\mathbf{O}^p$ denotes the origin of the path-tangential frame and $\mathbf{O}^{NED}$ denotes the origin of the inertial NED frame, $\mathbf{p}_i$ denotes vehicle i, and $\mathbf{p}^f_{f,i}$ denotes the desired position of vehicle i relative to $\mathbf{p}_b$. Figure inspired by Matouš, Pettersen, Varagnolo and Paliotta (2023b).

4.2 Communication and graph theory

In this work, both centralized and decentralized methods are presented. Centralized methods require that each vehicle communicates with every other vehicle and the full state of every vehicle is needed for calculation of controller outputs. These methods are typically infeasible to implement in practice because of communication limitations, but they provide interesting theoretical results and may serve as a basis for developing decentralized controllers.

In decentralized methods, each vehicle calculates its own controller output, often with limited knowledge of the state of other vehicles. Each agent may have access to information from only a limited number of local neighbors. This communication topology is represented by a graph, $\mathcal{G} = (\mathcal{V}, \mathcal{E})$, where the set of vertices $\mathcal{V} \coloneqq \{1, 2, \ldots, N\}$ corresponds to the agents and the set of edges $\mathcal{E} \subseteq \mathcal{V}^2$ represents the communication between pairs of agents. Let M be the cardinality of $\mathcal{E}$. The set $\mathcal{E}$ is then given by $\{e_k | k = 1, \ldots, M\}$, where each edge e_k is an ordered pair $(i, j) \in \mathcal{E}$ indicating that agent j has access to information from agent i. If the graph is *undirected*, information flows in both directions meaning that if a vertex pair $(i, j) \in \mathcal{E}$ then so is (j, i). The graph is *connected* if there exists a path connecting every agent to every other agent, and it is *complete* (fully connected) if there exists an edge between every pair of agents. We let the set of neighbors of a vertex i be denoted by the set

$$\mathcal{N}_i = \{j \in \mathcal{V} : (i, j) \in \mathcal{E}\}. \tag{4.6}$$

The Laplacian matrix of the graph is a matrix $\mathbf{L} \in \mathbb{R}^{N \times N}$ such that

$$\mathbf{L}_{ij} = \begin{cases} \sum_{j=1}^{N} a_{ij}, & i = j. \\ -a_{ij}, & i \neq j, \end{cases}, \quad a_{ij} = \begin{cases} 1, & \text{if } (j, i) \in \mathcal{E}, \\ 0, & \text{otherwise.} \end{cases} \tag{4.7}$$

It is useful in multiple formation-control methods, particularly consensus methods such as the formation-keeping task in our distributed NSB method as presented in Chapter 8. For an undirected graph, the Laplacian matrix is symmetric positive-semidefinite. It has an eigenvalue $\lambda_0 = 0$ corresponding to the eigenvector $\mathbf{v}_0 = [1, \ldots, 1]^{\mathrm{T}}$.

Chapter 5

Null-Space-Projection

An important prerequisite to understanding the NSB method is to understand the null-space-projection method for task priority control of robot manipulators. The main concepts in the NSB method were first developed for robot manipulators and then applied to coordination tasks in fleets of autonomous mobile robots. Our extended NSB method for double integrator systems is also inspired by similar, existing second-order methods in robot manipulators.

The chapter is organized as follows. Sections 5.1-5.3 are background theory sections. Sections 5.1 and 5.2 present task priority control with null-space-projection as developed for robot-manipulators (Siciliano et al.; 2009; Chiaverini et al.; 2008). Section 5.3 details and discusses the first-order NSB algorithm for coordinated path-following control as presented in existing literature (Arrichiello et al.; 2006; Antonelli and Chiaverini; 2006; Matouš, Pettersen, Varagnolo and Paliotta; 2023b). Section 5.4 presents our novel method for NSB control with double-integrator systems.

5.1 Null-space-projection for first-order systems

The null-space-projection method was derived for redundant robot manipulators. The method enables the creation of additional objectives that are followed as well as possible,

without conflicting with the main objective. Because the manipulators are redundant, there will always be a null space of joint velocities that only affect the internal motion of the robot arm without affecting the end-effector motion. Additional tasks can be constructed in this null space such as obstacle- or singularity-avoidance. This section introduces the null-space-projection method as derived for robot manipulators. We refer to Siciliano et al. (2009) and Chiaverini et al. (2008) for further reading. The notation differs from the sources to remain consistent with the rest of our work.

We consider single-integrator (first-order) systems on the form

$$\dot{\mathbf{x}} = \mathbf{v}, \tag{5.1}$$

where $\mathbf{x}$ are the generalized coordinates of the system. We define task variables $\boldsymbol{\sigma}_i = f_i(\mathbf{x})$, with the desired values $\boldsymbol{\sigma}_{d,i}$. A typical choice of task variable for robot manipulators would be the end-effector position. Using the chain rule, the time derivative of the task variables is given by

$$\dot{\boldsymbol{\sigma}}_i = \mathbf{J}_i \mathbf{v}, \tag{5.2}$$

where $\mathbf{J}_i = \partial \boldsymbol{\sigma}_i / \partial \mathbf{x}$ is the task Jacobian. Because the system is redundant, there exists a vector space of feasible velocities that satisfy the task given by a desired task-space velocity $\dot{\boldsymbol{\sigma}}_1^*$:

$$\mathbf{v} = \mathbf{J}_1^\dagger \dot{\boldsymbol{\sigma}}_1^* + \mathbf{N}_1 \mathbf{v}_0, \tag{5.3}$$

where $\mathbf{J}_i^\dagger$ is the Moore-Penrose pseudo-inverse, and $\mathbf{N}_i = (\mathbf{I} - \mathbf{J}_i^\dagger \mathbf{J}_i)$ is a null-space projection matrix of $\mathbf{J}_i$ so that $\mathbf{J}_i \mathbf{N}_i = 0$. Because the additional velocities $\mathbf{v}_0$ are projected into the null space of the first task, they will not conflict with the fulfillment of that task.

Given an additional task defined by the task variable $\boldsymbol{\sigma}_2$, the optimal value of the additional velocity $\mathbf{v}_0$ is derived. First, to not violate the first objective, it must hold that:

$$\dot{\boldsymbol{\sigma}}_2 = \mathbf{J}_2 \mathbf{v} = \mathbf{J}_2 \left(\mathbf{J}_1^\dagger \dot{\boldsymbol{\sigma}}_1 + \mathbf{N}_1 \mathbf{v}_0 \right). \tag{5.4}$$

Solving for $\mathbf{v}_0$ gives

$$\mathbf{v}_0 = (\mathbf{J}_2\mathbf{N}_1)^\dagger\left(\dot{\boldsymbol{\sigma}}_2^* - \mathbf{J}_2\mathbf{J}_1^\dagger\dot{\boldsymbol{\sigma}}_1^*\right). \tag{5.5}$$

The term $-\mathbf{J}_2\mathbf{J}_1^\dagger\dot{\boldsymbol{\sigma}}_1^*$ can be interpreted as subtracting the parts of the second task that are already satisfied by the first task. The pseudo-inverse term $(\mathbf{J}_2\mathbf{N}_1)^\dagger$ optimizes the velocity $\mathbf{v}_0$ to satisfy the second task as well as possible within the null space of the first task.

Back-substituting (5.5) into (5.3) gives

$$\mathbf{v} = \mathbf{J}_1^\dagger\boldsymbol{\sigma}_1^* + \mathbf{N}_1(\mathbf{J}_2\mathbf{N}_1)^\dagger\left(\dot{\boldsymbol{\sigma}}_2^* - \mathbf{J}_2\mathbf{J}_1^\dagger\dot{\boldsymbol{\sigma}}_1^*\right). \tag{5.6}$$

If there are more than two tasks, the lower-priority tasks must be projected into the joint null space spanned by the stacked Jacobian of all higher-priority tasks. That leads to the following recursive solution:

$$\mathbf{v} = \sum_{i=1}^{n_t}\bar{\mathbf{N}}_{i-1}\mathbf{v}_i, \quad \text{with } \mathbf{v}_i = \left(\mathbf{J}_i\bar{\mathbf{N}}_{i-1}\right)^\dagger\left(\dot{\boldsymbol{\sigma}}_i^* - \mathbf{J}_i\sum_{k=1}^{i-1}\bar{\mathbf{N}}_{k-1}\mathbf{v}_k\right), \tag{5.7}$$

with $\bar{\mathbf{N}}_i$ being the null-space projection of the stacked Jacobian $\bar{\mathbf{J}}_i = [\mathbf{J}_1^\mathrm{T}\ \dots\ \mathbf{J}_i^\mathrm{T}]^\mathrm{T}$.

5.2 Null-space-projection for second-order systems

All mechanical systems that obey Newton's second law are inherently second-order, meaning they follow double-integrator dynamics. The first-order method derived in the previous section works well because there often exist controllers that enable us to accurately track desired velocities. Nevertheless, modeling the second-order dynamics enables us to interpretably express the dynamic motion in task space.

We consider a double-integrator (second-order) system on the form

$$\dot{\mathbf{x}} = \mathbf{v}, \tag{5.8}$$

$$\dot{\mathbf{v}} = \mathbf{a}. \tag{5.9}$$

With the definition of task variables $\boldsymbol{\sigma}_i$ from Section 5.1 the following differential relation holds

$$\ddot{\boldsymbol{\sigma}}_i = \mathbf{J}_i\dot{\mathbf{v}} + \dot{\mathbf{J}}_i\mathbf{v}. \tag{5.10}$$

With a similar derivation as for the single-integrator case, the desired accelerations given two tasks are

$$\dot{\mathbf{v}} = \mathbf{J}_1^{\dagger}(\ddot{\boldsymbol{\sigma}}_1^* - \dot{\mathbf{J}}_1\mathbf{v}) + \mathbf{N}_1(\mathbf{J}_2\mathbf{N}_1)^{\dagger}\left(\ddot{\boldsymbol{\sigma}}_2^* - \dot{\mathbf{J}}_2\mathbf{v} - \mathbf{J}_2\mathbf{J}_1^{\dagger}(\ddot{\boldsymbol{\sigma}}_1^* - \dot{\mathbf{J}}_1\mathbf{v})\right). \tag{5.11}$$

For multiple tasks, the recursive formulation is similar to the one derived for single-integrator systems (5.7):

$$\dot{\mathbf{v}} = \sum_{i=1}^{n_t} \bar{\mathbf{N}}_{i-1}\dot{\mathbf{v}}_i, \quad \text{with } \dot{\mathbf{v}}_i = \left(\mathbf{J}_i\bar{\mathbf{N}}_{i-1}\right)^{\dagger}\left(\ddot{\boldsymbol{\sigma}}_i^* - \dot{\mathbf{J}}_i\mathbf{v} - \mathbf{J}_i\sum_{k=1}^{i-1}\bar{\mathbf{N}}_{k-1}\dot{\mathbf{v}}_k\right). \tag{5.12}$$

5.3 NSB method for first-order systems

In the formation control literature, a slightly different method called the NSB method is commonly applied for formation control. The general method is presented and motivated in Chiaverini (1997) as a way to eliminate the problems resulting from *algorithmic singularities* in (5.6). An *algorithmic singularity* occurs when $\mathbf{J}_2\mathbf{N}_1$ looses rank despite $\mathbf{J}_1$ and $\mathbf{J}_2$ being full rank. This loss of rank happens if the task Jacobians are linearly dependent.

The NSB formulation which solves the *algorithmic singularity* problem is given by

$$\mathbf{v} = \mathbf{v}_1 + \mathbf{N}_1\mathbf{v}_2, \quad \text{with} \quad \mathbf{v}_i = \mathbf{J}_i^{\dagger}\dot{\boldsymbol{\sigma}}_i^*. \tag{5.13}$$

This formulation has a slightly different interpretation. The optimal velocity for the second task is first calculated globally, $\mathbf{v}_2 = \mathbf{J}_2^{\dagger}\boldsymbol{\sigma}_2^*$, and then projected into the null space of the first task, which is in contrast to the method (5.6), in which the second task velocity is optimized directly within the null space of the first task. Consequently, method (5.13) leads to larger task errors for the second task but avoids the problems of algorithmic singularities.

To recover the errors, the method is used with a closed-loop inverse kinematics (CLIK) implementation, which enables the recovery of the tracking errors. The CLIK solution is defined by choosing $\boldsymbol{\sigma}_i^*$ as follows:

$$\boldsymbol{\sigma}_i^* = \dot{\boldsymbol{\sigma}}_{d,i} - \boldsymbol{\Lambda}_i \tilde{\boldsymbol{\sigma}}_i, \tag{5.14}$$

where $\boldsymbol{\Lambda}_i$ is a positive definite gain matrix and $\tilde{\boldsymbol{\sigma}}_i = \boldsymbol{\sigma}_i - \boldsymbol{\sigma}_{d,i}$. We can interpret the CLIK as a linear feedback law in task space.

Most formation control literature concerning the NSB algorithm presents the following recursive formulation for more than two tasks (Arrichiello et al.; 2006; Antonelli and Chiaverini; 2006; Matouš, Pettersen, Varagnolo and Paliotta; 2023b):

$$\mathbf{v} = \mathbf{v}_1 + \mathbf{N}_1 \left(\mathbf{v}_2 + \mathbf{N}_2 \mathbf{v}_3 \right). \tag{5.15}$$

The formulation has a nice geometrical interpretation, in which the velocity of each task is projected into the null space of the immediate higher-priority task to remove those velocity components that would conflict with it. A problem with this formulation is that it does not behave fully as one might expect. The expected behavior is that the third task produces velocities that neither conflict with the first nor the second task. However, the null-space projection of $\mathbf{N}_2\mathbf{v}_3$ into the null space of the first task, $\mathbf{N}_1\mathbf{N}_2\mathbf{v}_3$, might produce motions that are no longer in the null space of the second task and therefore conflict with it. Antonelli et al. (2008) remark that the *correct* projection is given by:

$$\mathbf{v} = \mathbf{v}_1 + \mathbf{N}_1\mathbf{v}_2 + \bar{\mathbf{N}}_2\mathbf{v}_3, \tag{5.16}$$

with $\bar{\mathbf{N}}_2$ being the null-space projection of the stacked Jacobian $\bar{\mathbf{J}}_2 = [\mathbf{J}_1^{\mathrm{T}} \mathbf{J}_2^{\mathrm{T}}]^{\mathrm{T}}$. Unlike the former formulation, this formulation projects the velocity from the third task into the joint null space of the two first tasks so that it does not conflict with either of them. Furthermore, Antonelli et al. (2008) argue that the former approach only is stable whenever two out of the three tasks are *orthogonal*, however, in that case, the two formulations are equivalent. Also, Antonelli et al. (2008) presented general stability conclusions of the formulation (5.16) when extended to N tasks and argued

that similar general stability conclusions cannot be made for the formulation (5.15). The formulation (5.16) is preferable when there are non-orthogonal tasks, and will be used herein, but we note that in most formation control applications, the two formulations are equivalent due to orthogonality in task definitions.

In summary, the general NSB method for n_t tasks is given by

$$\mathbf{v} = \sum_{i=1}^{n_t} \bar{\mathbf{N}}_{i-1}\mathbf{v}_i, \quad \text{with} \quad \mathbf{v}_i = \mathbf{J}_i^{\dagger}\dot{\boldsymbol{\sigma}}_i^{*}. \tag{5.17}$$

5.4 NSB method for second-order systems

We develop the NSB method for double-integrator systems (5.8) by applying a similar solution to the *algorithmic singularity* problem as presented in Section 5.3 to the second-order method from Section 5.2. The general method is given by

$$\dot{\mathbf{v}} = \sum_{i=1}^{n_t} \bar{\mathbf{N}}_{i-1}\dot{\mathbf{v}}_i, \quad \text{with} \quad \dot{\mathbf{v}}_i = \mathbf{J}_i^{\dagger}\left(\ddot{\boldsymbol{\sigma}}_i^{*} - \dot{\mathbf{J}}_i\mathbf{v}\right). \tag{5.18}$$

Similarly to Section 5.3, we introduce feedback in task space to recover tracking errors. Since the underlying system (5.8) is second-order, we define a second-order linear controller

$$\ddot{\boldsymbol{\sigma}}_i^{*} = \ddot{\boldsymbol{\sigma}}_{d,i} - \boldsymbol{\Lambda}_{p,i}\tilde{\boldsymbol{\sigma}}_i - \boldsymbol{\Lambda}_{d,i}\dot{\tilde{\boldsymbol{\sigma}}}_i. \tag{5.19}$$

The resulting SOCLIK solution is given by:

$$\dot{\mathbf{v}}_i = \mathbf{J}_i^{\dagger}\left(\ddot{\boldsymbol{\sigma}}_{d,i} - \boldsymbol{\Lambda}_{p,i}\tilde{\boldsymbol{\sigma}}_i - \boldsymbol{\Lambda}_{d,i}\dot{\tilde{\boldsymbol{\sigma}}}_i - \dot{\mathbf{J}}_i\mathbf{v}\right). \tag{5.20}$$

where $\boldsymbol{\Lambda}_{p,i}$ and $\boldsymbol{\Lambda}_{d,i}$ are positive definite gain matrices. As with other second-order systems, $\boldsymbol{\Lambda}_{p,i}$ and $\boldsymbol{\Lambda}_{d,i}$ can be selected to specify closed-loop natural frequencies and relative damping ratios:

$$\boldsymbol{\Lambda}_{p,i} = \boldsymbol{\Omega}_{n,i}^2, \quad \boldsymbol{\Lambda}_{d,i} = 2\mathbf{Z}\boldsymbol{\Omega}_{n,i}, \tag{5.21}$$

with

$$\mathbf{\Omega}_{n,i} = \text{diag}\{\omega_{n_{i,1}} \dots \omega_{n_{i,t_i}}\}, \tag{5.22}$$

$$\mathbf{Z} = \text{diag}\{\zeta_{i,1} \dots \zeta_{i,t_i}\}, \tag{5.23}$$

where $\omega_{n_{i,j}}$ and $\zeta_{i,j}$ are the natural frequency and damping ratio for the j-th state of task i, and t_i is the dimension of task i. Because mechanical systems described by Newton-Euler equations are second-order, the entire error dynamics of the task are interpretably specified as spring-damper systems in task space. In contrast, the first-order method given by (5.17) gives a first-order error system in task space which will have additional error dynamics from the low-level velocity controller.

Chapter 6

The Centralized NSB Method

This chapter introduces the tasks considered in our implementation of the NSB algorithm for multi-vehicle formation control. These tasks represent the main objectives that the vehicles in the fleet must achieve to operate safely and efficiently. The tasks are similar to those presented by Matouš, Pettersen, Varagnolo and Paliotta (2023b), but we modify them to work with SOCLIK methods in double-integrator systems instead of CLIK methods in single-integrator systems. Most of the results from this chapter have been submitted to the 62nd IEEE Conference on Decision and Control (Lie et al.; 2023).

Three tasks are considered in decreasing order of priority: inter-vehicle collision avoidance, formation keeping, and path following. Inter-vehicle collision avoidance ensures that the fleet avoids dangerous collisions, which can result in severe damage to the involved vehicles and nearby property. The second task, formation keeping, is essential for maintaining a cohesive and stable fleet that can move as a single entity and achieve common goals. Path following requires the vehicles to track a desired trajectory while mitigating disturbances and external effects such as wind and currents, which is important for tasks such as search and rescue missions or environmental monitoring where the vehicles need to follow a pre-determined path. By incorporating all three tasks into the NSB algorithm, we can ensure that the fleet behaves in a coordinated and efficient manner while meeting its mission requirements.

The fleet consists of n AUVs following the assumptions and vehicle model from Chapter 2. Each vehicle is equipped with an input-output linearizing hand-position controller as described in Chapter 3, yielding double-integrator position dynamics. This chapter considers the notation and definitions for formation path following from Chapter 4 and the external dynamics of each vehicle in the fleet follow the model:

$$\begin{aligned} \dot{\mathbf{p}}_i &= \mathbf{v}_i + \mathbf{v}_c, \\ \dot{\mathbf{v}}_i &= \boldsymbol{\mu}_i. \end{aligned} \tag{6.1}$$

The chapter is organized as follows. Section 6.1 introduces the high-level combination of the three tasks, specifying the particular solution to the general NSB controller (5.18) for this problem. Sections 6.2, 6.3, and 6.4 introduce each of the three tasks in the NSB hierarchy. Section 6.5 introduces two different methods for estimating and compensating for the unknown ocean current, and Section 6.6 describes two methods for modifying the NSB method to include external obstacle avoidance.

6.1 Combined NSB controller

The three tasks inter-vehicle collision avoidance, formation keeping, and path following are combined using the NSB algorithm for second-order systems (5.18). We let the commanded acceleration from each task be given by $\dot{\mathbf{v}}_1$, $\dot{\mathbf{v}}_2$ and $\dot{\mathbf{v}}_3$ in order. These accelerations are generally given by SOCLIK (5.20) solutions and are defined in later sections. Note that $\dot{\mathbf{v}}_j$ is a stacked vector of accelerations for the whole fleet, and the commanded acceleration for a single vehicle will be denoted by double subscripts: $\dot{\mathbf{v}}_{j,i}$. The combined commanded acceleration is given by

$$\dot{\mathbf{v}}_{NSB} = \dot{\mathbf{v}}_1 + \mathbf{N}_1\dot{\mathbf{v}}_2 + \bar{\mathbf{N}}_2\dot{\mathbf{v}}_3, \tag{6.2}$$

where we recall that $\mathbf{N}_1 = (\mathbf{I} - \mathbf{J}_1^\dagger\mathbf{J}_1)$ is the null-space projector of task 1 and $\bar{\mathbf{N}}_2 = (\mathbf{I} - [\mathbf{J}_1^\mathrm{T}\mathbf{J}_2^\mathrm{T}]^{\mathrm{T}^\dagger}[\mathbf{J}_1^\mathrm{T}\mathbf{J}_2^\mathrm{T}]^\mathrm{T})$ is the null-space projector of the space spanned by the Jacobians the first and second tasks. In this particular setup, the third task is orthogonal to the first two tasks since they deal with the relative motion within the fleet, while the last

task addresses the collective motion of the entire fleet. Consequently, the combined commanded acceleration (6.2) can be simplified, and the stacked resulting control action $\boldsymbol{\mu}$ is given by

$$\boldsymbol{\mu} = \dot{\mathbf{v}}_{NSB} = \dot{\mathbf{v}}_1 + \mathbf{N}_1\dot{\mathbf{v}}_2 + \dot{\mathbf{v}}_3. \tag{6.3}$$

We note that the equations of motion for the barycenter $\mathbf{p}_b$ defined by (4.2) is dependent only on the third task acceleration because the within-fleet accelerations from the first two tasks cancel out when summing over the fleet. Differentiation (4.2) with respect to time, we get

$$\dot{\mathbf{p}}_b = \frac{1}{n}\sum_{i=1}^{n}\dot{\mathbf{p}}_i = \frac{1}{n}\sum_{i=1}^{n}\mathbf{v}_i + \mathbf{v}_c \triangleq \mathbf{v}_b + \mathbf{v}_c, \tag{6.4a}$$

$$\ddot{\mathbf{p}}_b = \dot{\mathbf{v}}_b = \frac{1}{n}\sum_{i=1}^{n}\boldsymbol{\mu}_i = \frac{1}{n}\sum_{i=1}^{n}\dot{\mathbf{v}}_{3,i} \triangleq \boldsymbol{\mu}_b. \tag{6.4b}$$

6.2 Inter-vehicle collision avoidance task

The highest-priority task is the inter-vehicle collision avoidance (COLAV) task. The task ensures that the minimum distance between two vehicles in the fleet remains larger than a predefined threshold d_{COLAV}, eliminating the chance of collisions.

The task is defined by its task variable $\boldsymbol{\sigma}_1 = [\sigma_{1,1}^{\mathrm{T}}, \ldots, \sigma_{1,l}^{\mathrm{T}}]^{\mathrm{T}}$, which is a stacked vector of relative distances between vehicles closer than the threshold d_{COLAV}:

$$\sigma_{1,k} = \|\mathbf{p}_i - \mathbf{p}_j\|, \quad \forall i, j \in 1, \ldots, n : j > i, \|\mathbf{p}_i - \mathbf{p}_j\| < d_{COLAV}. \tag{6.5}$$

The task size varies depending on the number of vehicles within the activation distance. It is empty when all vehicles are further than d_{COLAV} apart from each other. The desired values of the task are given by

$$\boldsymbol{\sigma}_{d,1} = d_{COLAV}\mathbf{1}_l, \tag{6.6}$$

and we note that $\ddot{\boldsymbol{\sigma}}_{d,1} = \dot{\boldsymbol{\sigma}}_{d,1} = 0$. Because the task only activates when the distance is below the threshold, the distance may temporarily violate the threshold due to the

system's response time before a safe distance is recovered. Therefore, the threshold should be chosen larger than the minimum safe distance by a small margin.

The stacked partial derivatives for each active collision make up the task Jacobian, which can be expressed as

$$\mathbf{J}_1 = \left[\left(\frac{\partial \sigma_{1,1}}{\partial \mathbf{p}} \right)^{\mathrm{T}}, \ldots, \left(\frac{\partial \sigma_{1,l}}{\partial \mathbf{p}} \right)^{\mathrm{T}} \right]^{\mathrm{T}}, \tag{6.7a}$$

$$\frac{\partial \sigma_{1,k}}{\partial \mathbf{p}_i} = \frac{(\mathbf{p}_i - \mathbf{p}_j)^{\mathrm{T}}}{\|\mathbf{p}_i - \mathbf{p}_j\|}, \ \frac{\partial \sigma_{1,k}}{\partial \mathbf{p}_j} = -\frac{(\mathbf{p}_i - \mathbf{p}_j)^{\mathrm{T}}}{\|\mathbf{p}_i - \mathbf{p}_j\|}. \tag{6.7b}$$

The partial derivative of each task variable with respect to vehicles that are not involved in the collision is zero. The derivative of the task Jacobian is similarly given by a stack of time-differentiated partial derivatives

$$\dot{\mathbf{J}}_1 = \left[\left(\frac{\mathrm{d}}{\mathrm{d}t} \frac{\partial \sigma_{1,1}}{\partial \mathbf{p}} \right)^{\mathrm{T}}, \ldots, \left(\frac{\mathrm{d}}{\mathrm{d}t} \frac{\partial \sigma_{1,l}}{\partial \mathbf{p}} \right)^{\mathrm{T}} \right]^{\mathrm{T}}, \tag{6.8a}$$

$$\frac{\mathrm{d}}{\mathrm{d}t} \frac{\partial \sigma_{1,k}}{\partial \mathbf{p}_i} = \left(\frac{\mathbb{I}_3}{\|\mathbf{p}_i - \mathbf{p}_j\|} - \frac{(\mathbf{p}_i - \mathbf{p}_j)(\mathbf{p}_i - \mathbf{p}_j)^{\mathrm{T}}}{\|\mathbf{p}_i - \mathbf{p}_j\|^3} \right) (\mathbf{v}_i - \mathbf{v}_j), \tag{6.8b}$$

$$\frac{\mathrm{d}}{\mathrm{d}t} \frac{\partial \sigma_{1,k}}{\partial \mathbf{p}_j} = -\left(\frac{\mathbb{I}_3}{\|\mathbf{p}_i - \mathbf{p}_j\|} - \frac{(\mathbf{p}_i - \mathbf{p}_j)(\mathbf{p}_i - \mathbf{p}_j)^{\mathrm{T}}}{\|\mathbf{p}_i - \mathbf{p}_j\|^3} \right) (\mathbf{v}_i - \mathbf{v}_j). \tag{6.8c}$$

The resulting SOCLIK equation for the task is

$$\dot{\mathbf{v}}_1 = -\mathbf{J}_1^{\dagger} \left(\mathbf{\Lambda}_{p,1} \tilde{\boldsymbol{\sigma}}_1 + \mathbf{\Lambda}_{d,1} \dot{\boldsymbol{\sigma}}_1 + \dot{\mathbf{J}}_1 (\mathbf{v} + \mathbf{V}_c) \right), \tag{6.9}$$

with $\dot{\boldsymbol{\sigma}}_1 = \mathbf{J}_1(\mathbf{v} + \mathbf{V}_c)$. Note that because $\partial \sigma_{1,k} / \partial \mathbf{p}_i = -\partial \sigma_{1,k} / \partial \mathbf{p}_j$, it follows that $\mathbf{J}_1 \mathbf{V}_c = \dot{\mathbf{J}}_1 \mathbf{V}_c = \mathbf{0}$. Consequently, $\dot{\mathbf{v}}_1$ is independent of the ocean current velocity and given by

$$\dot{\mathbf{v}}_1 = -\mathbf{J}_1^{\dagger} \left(\mathbf{\Lambda}_{p,1} \tilde{\boldsymbol{\sigma}}_1 + \mathbf{\Lambda}_{d,1} \dot{\boldsymbol{\sigma}}_1 + \dot{\mathbf{J}}_1 \mathbf{v} \right), \tag{6.10}$$

with $\dot{\boldsymbol{\sigma}}_1 = \mathbf{J}_1 \mathbf{v}$.

6.3 Formation-keeping task

The formation-keeping task is designed to move the vehicles into a predefined geometric configuration in the formation-centered frame. The task ensures initial convergence to the desired formation. After convergence, the vehicle velocities are adjusted to account for the curvature of the path. The velocities of vehicles in the outer turns are increased, while those in the inner turns are decreased, to ensure that the formation remains orthogonal to the path-tangential coordinate frame.

The task variable is given by the stacked vector of barycenter relative positions:

$$\boldsymbol{\sigma}_2 = \left[\boldsymbol{\sigma}_{2,1}^{\mathrm{T}}, ..., \boldsymbol{\sigma}_{2,n-1}^{\mathrm{T}}\right]^{\mathrm{T}}, \quad \boldsymbol{\sigma}_{2,i} = \mathbf{p}_i - \mathbf{p}_b, \tag{6.11}$$

and the desired values are given by the predefined formation vectors, rotated from the formation frame to the inertial frame:

$$\boldsymbol{\sigma}_{d,2} = [(\mathbf{R}_p \mathbf{p}_{f,1}^f)^{\mathrm{T}}, ..., (\mathbf{R}_p \mathbf{p}_{f,n-1}^f)^{\mathrm{T}}]^{\mathrm{T}}. \tag{6.12}$$

The desired positions in the formation-centered frame are constant, but the rotation matrix is time-varying, so the desired first and second derivatives of the task variable are given by

$$\dot{\boldsymbol{\sigma}}_{d,2} = [(\dot{\mathbf{R}}_p \mathbf{p}_{f,1}^f)^{\mathrm{T}}, ..., (\dot{\mathbf{R}}_p \mathbf{p}_{f,n-1}^f)^{\mathrm{T}}]^{\mathrm{T}}, \tag{6.13}$$

$$\ddot{\boldsymbol{\sigma}}_{d,2} = [(\ddot{\mathbf{R}}_p \mathbf{p}_{f,1}^f)^{\mathrm{T}}, ..., (\ddot{\mathbf{R}}_p \mathbf{p}_{f,n-1}^f)^{\mathrm{T}}]^{\mathrm{T}}. \tag{6.14}$$

There is one fewer task than AUVs to avoid singularities, as the last AUV's position is implied by the constraint $\sum_{i=1}^{n} \mathbf{p}_{f,i}^f = \mathbf{0}$, which comes as a result of the formation-keeping frame having the origin at the barycenter.

The Jacobian is constant and given by

$$\mathbf{J}_2 = \left(\begin{bmatrix} \mathbb{I}_{n-1} & \mathbf{0}_{n-1,1} \end{bmatrix} - \frac{\mathbf{1}_{n-1,n}}{N}\right) \otimes \mathbb{I}_3. \tag{6.15}$$

Because the Jacobian is constant, its derivative is zero. Then, the SOCLIK equation

reduces to

$$\dot{\mathbf{v}}_2 = \mathbf{J}_2^{\dagger}\big(\ddot{\boldsymbol{\sigma}}_{d,2} - \boldsymbol{\Lambda}_{p,2}\tilde{\boldsymbol{\sigma}}_2 - \boldsymbol{\Lambda}_{d,2}\dot{\tilde{\boldsymbol{\sigma}}}_2\big). \tag{6.16}$$

Like the inter-vehicle collision avoidance task, this task is independent of the ocean current because $\mathbf{J}_2\mathbf{V}_c = \mathbf{0}$.

The nominal task acceleration (6.16) may become arbitrarily large depending on the formation-keeping error, which may saturate the actuators. When combined with the other tasks, the full NSB controller may also lead to a loss of controllability if the formation-keeping velocities exactly cancel out the path-following velocities. Therefore, we introduce the saturated task acceleration

$$\dot{\mathbf{v}}_2 = \mathbf{J}_2^{\dagger}\big(\ddot{\boldsymbol{\sigma}}_{d,2} - v_{2_{\max}}\,\mathrm{sat}\big(\boldsymbol{\Lambda}_{p,2}\tilde{\boldsymbol{\sigma}}_2\big) - \boldsymbol{\Lambda}_{d,2}\dot{\tilde{\boldsymbol{\sigma}}}_2\big), \tag{6.17}$$

where $v_{2_{\max}}$ is a positive constant and sat is a saturation function given by

$$\mathrm{sat}\big(\mathbf{x}\big) = \mathbf{x}\frac{\tanh\|\mathbf{x}\|}{\|\mathbf{x}\|}. \tag{6.18}$$

With the saturated task acceleration, we further require that the product of the gain matrices $\boldsymbol{\Lambda}_{p,2}\boldsymbol{\Lambda}_{d,2}$ is symmetric positive definite. The reason for this requirement will become clear in the stability proof in Section 7.1.

The control action due to the task error is limited by the saturated task acceleration, reducing the chance of actuator saturation. Furthermore, the saturated task acceleration leads to a bounded task velocity which can be chosen sufficiently small so that it cannot exactly cancel out the path-following velocity, hence eliminating the problem of controllability loss.

6.4 Path-following task

The path-following task involves controlling the barycenter of the vehicle fleet to follow a given path. The task is designed to ensure that the vehicles remain on the desired trajectory while accounting for external disturbances such as ocean currents. The AUVs move in three dimensions and we apply the *coupled* line-of-sight (LOS)

method from Matouš, Pettersen, Varagnolo and Paliotta (2023b). Wheras *decoupled* LOS methods utilize two distinct guidance schemes to steer the vehicle separately in the horizontal and vertical planes (Caharija et al.; 2012), *coupled* LOS methods employ a single guidance scheme to steer the vehicle simultaneously in all three dimensions (Breivik and Fossen; 2005). LOS methods are generally defined at the first-order kinematic level, with velocity or orientation references as output. We differentiate the LOS method and introduce feedback so that it can work directly with double-integrator systems. The method views the entire fleet as one entity and provides a common path-following acceleration to every vehicle in the fleet. An advantage of using a LOS method for path following compared to a simpler alternative, like a PID controller in the path error, is that the LOS method provides a constant-speed approach to the path, which ensures that the vehicles remain at controllable velocities and furthermore mitigates actuator saturation at large path errors.

We let the path-following error be defined by the barycenter position in the path-tangential frame $\mathbf{p}_b^p$ and let its components be denoted by x_b^p, y_b^p and z_b^p. Inspired by Belleter et al. (2019), the error-dependent look-ahead distance is given by

$$\Delta(\mathbf{p}_b^p) = \sqrt{\Delta_0^2 + (x_b^p)^2 + (y_b^p)^2 + (z_b^p)^2}, \tag{6.19}$$

where Δ_0 is a positive constant. The LOS velocity is given by

$$\mathbf{v}_{LOS,d} = \mathbf{R}_p \left[\Delta(\mathbf{p}_b^p), -y_b^p, -z_b^p\right]^\mathrm{T} \frac{U_{LOS}}{D}, \tag{6.20}$$

where $U_{LOS} > 0$ is the desired path-following speed, and

$$D = \sqrt{\Delta(\cdot)^2 + (y_b^p)^2 + (z_b^p)^2} \tag{6.21}$$

is a normalization term.

Our method differs from that of Matouš, Pettersen, Varagnolo and Paliotta (2023b) in that we differentiate the desired LOS velocity (6.20) once to derive the desired LOS

acceleration

$$\begin{aligned}\dot{\mathbf{v}}_{LOS,d} = &\dot{\mathbf{R}}_p \left[\Delta(\mathbf{p}_b^p), -y_b^p, -z_b^p\right]^{\mathrm{T}} \frac{U_{LOS}}{D} \\ &+ \mathbf{R}_p \left[\dot{\Delta}(\mathbf{p}_b^p, \dot{\mathbf{p}}_b^p), -\dot{y}_b^p, -\dot{z}_b^p\right]^{\mathrm{T}} \frac{U_{LOS}}{D} \\ &- \mathbf{R}_p \left[\Delta(\mathbf{p}_b^p), -y_b^p, -z_b^p\right]^{\mathrm{T}} \frac{U_{LOS}}{D^2}\dot{D}.\end{aligned} \tag{6.22}$$

To mitigate drift from numerical integration, and because the initial velocity of the fleet can differ from the desired LOS velocity, we let the task acceleration be given by the following linear relation

$$\dot{\mathbf{v}}_{LOS} = \dot{\mathbf{v}}_{LOS,d} + \mathbf{\Lambda}_{LOS}(\mathbf{v}_{LOS,d} - \mathbf{v}_b - \mathbf{v}_c), \tag{6.23}$$

where $\mathbf{v}_b = \frac{1}{N}\sum_{i=1}^{N} \mathbf{v}_i$ is the barycenter velocity and $\mathbf{\Lambda}_{LOS}$ is a positive definite gain matrix. The same acceleration is applied to each vehicle, so the resulting task acceleration is given by a simple Kronecker product

$$\dot{\mathbf{v}}_3 = \mathbf{1}_{n,1} \otimes \dot{\mathbf{v}}_{LOS}. \tag{6.24}$$

Lemma 6.1. *Let $\mathbf{\Lambda}_{LOS}$ be a positive definite gain matrix. The ocean-current relative barycenter velocity $\mathbf{v}_b$ converges to the relative LOS desired velocity $\mathbf{v}_{LOS,d} - \mathbf{v}_c$ under the controller defined by the three equations* (6.3), (6.23), *and* (6.24).

Proof. The closed-loop dynamics of the barycenter velocity $\mathbf{v}_b$ under the controller (6.3) are given by (6.4). In (6.24), $\dot{\mathbf{v}}_3$ is defined as a stack of $\dot{\mathbf{v}}_{LOS}$ repeated n times. Consequently,

$$\boldsymbol{\mu}_b = \frac{1}{n}\sum_{i=1}^{n} \dot{\mathbf{v}}_{3,i} = \dot{\mathbf{v}}_{LOS}. \tag{6.25}$$

Inserting for (6.23), the closed-loop dynamics of the error $\tilde{\mathbf{v}}_b = \mathbf{v}_b + \mathbf{v}_c - \mathbf{v}_{LOS,d}$ are given by

$$\dot{\tilde{\mathbf{v}}}_b = -\mathbf{\Lambda}_{LOS}\tilde{\mathbf{v}}_b, \tag{6.26}$$

which is a linear system with a positive definite gain matrix. Then the system is

exponentially stable. □

The proof only holds if we know the ocean current $\mathbf{v}_c$, which is generally unknown. Section 6.5 will present approaches to overcome this shortcoming.

Like in Matouš, Pettersen, Varagnolo and Paliotta (2023b), the update of the path-parameter ξ is used as an extra degree of freedom to guarantee along-track stability:

$$\dot{\xi} = U_{LOS} \left\| \frac{\partial \mathbf{p}_p(\xi)}{\partial \xi} \right\|^{-1} \left(\frac{\Delta(\mathbf{p}_b^p)}{D} + k_\xi \frac{x_b^p}{\sqrt{1 + (x_b^p)^2}} \right). \tag{6.27}$$

This choice ensures that the desired LOS velocity (6.20) guarantees USGES of the path-following task, which we will rely on in the stability proof presented in Section 7.2.

6.5 Compensating unknown ocean currents

The AUV is subject to unknown ocean currents. The ocean currents are assumed constant and irrotational, which is often a reasonable assumption because the ocean current dynamics are much slower than the AUV dynamics. These currents can significantly affect the AUV's motion and make it difficult to achieve precise control and accurate navigation. To address this challenge, we propose two methods to estimate and compensate for the effect of ocean currents on AUV motion: integral action and ocean-current observer. Both methods require accurate measurement of the vehicle position. Because the ocean current is assumed to be equal for all vehicles, it is sufficient to compensate for it in the path-following task as it has no effect on the two tasks that concern the relative motion of vehicles within the fleet.

6.5.1 Integral action

Integral action is a common method in control theory to compensate for constant disturbances. The error between the desired fleet trajectory and the actual trajectory is continuously measured and used to update the control inputs in a way that accounts for the cumulative effect of past errors. As will be shown, the integral-error state will

grow until it exactly cancels out the ocean current resulting in the fleet following the desired absolute velocity.

We recall the feedback-linearized model (6.1):

$$\begin{aligned}\dot{\mathbf{p}}_i &= \mathbf{v}_i + \mathbf{v}_c,\\ \dot{\mathbf{v}}_i &= \boldsymbol{\mu}_i.\end{aligned}$$

We introduce the virtual integral state $\mathbf{p}_v$ defined by

$$\dot{\mathbf{p}}_v = \mathbf{v}_{LOS,d}, \tag{6.28}$$

and define the new input $\dot{\mathbf{v}}_{LOS,I}$

$$\dot{\mathbf{v}}_{LOS,I} = \dot{\mathbf{v}}_{LOS,d} + \boldsymbol{\Lambda}_{p,3}(\mathbf{v}_{LOS,d} - \mathbf{v}_b) + \boldsymbol{\Lambda}_{i,3}(\mathbf{p}_v - \mathbf{p}_b), \tag{6.29}$$

which replaces the previosly defined path-following task acceleration $\dot{\mathbf{v}}_{LOS}$ given by (6.23). The gain matrices $\boldsymbol{\Lambda}_{p,3}$ and $\boldsymbol{\Lambda}_{i,3}$ are positive definite.

Let the error variables be given by

$$\tilde{\mathbf{p}}_b = \mathbf{p}_b - \mathbf{p}_v - \boldsymbol{\Lambda}_{i,3}^{-1}\boldsymbol{\Lambda}_{p,3}\mathbf{v}_c, \tag{6.30a}$$

$$\tilde{\mathbf{v}}_b = \mathbf{v}_b + \mathbf{v}_c - \mathbf{v}_{LOS,d}. \tag{6.30b}$$

After applying the controller (6.3) with the path-following task-acceleration given by (6.24) and (6.29) to the fleet system (6.1), the barycenter equations of motion are given by (6.4) with control action $\boldsymbol{\mu}_b = \dot{\mathbf{v}}_{LOS,I}$. The resulting closed-loop error dynamics are

$$\begin{bmatrix}\dot{\tilde{\mathbf{p}}}\\ \dot{\tilde{\mathbf{v}}}\end{bmatrix} = \begin{bmatrix}\mathbf{0} & \mathbb{I}\\ -\boldsymbol{\Lambda}_{i,3} & -\boldsymbol{\Lambda}_{p,3}\end{bmatrix}\begin{bmatrix}\tilde{\mathbf{p}}\\ \tilde{\mathbf{v}}\end{bmatrix}. \tag{6.31}$$

For symmetric positive definite gain matrices $\boldsymbol{\Lambda}_{p,3}$ and $\boldsymbol{\Lambda}_{i,3}$ the system matrix is Hurwitz and the origin $[\tilde{\mathbf{p}}_b^{\mathrm{T}}\ \tilde{\mathbf{v}}_b^{\mathrm{T}}]^{\mathrm{T}} = \mathbf{0}$ is a globally exponentially stable (GES) equillibrium.

The position does not converge to the virtual integral state, however, that is not a problem. As long as the absolute velocity converges to the LOS velocity, the LOS method should ensure convergence to the path.

6.5.2 Ocean current observer

An alternative approach is to define an estimator of the ocean current $\mathbf{v}_c$ and insert it directly into equation (6.23). An advantage of this approach is that we can compensate for the ocean current in all tasks of the NSB algorithm if we were to define additional tasks that are dependent on the current.

We extend the observer by Aguiar and Pascoal (2002) to three dimensions. Additionally, we modify it to work with the hand-position feedback-linearized dynamics where the velocity is described in the NED coordinate frame. The observer gives estimates of the position $\hat{\mathbf{p}}$ and the ocean-current velocity $\hat{\mathbf{v}}_c$. We let the velocity and position of the observer be given by the barycenter of the fleet, and get the following observer

$$\dot{\hat{\mathbf{p}}}_b = \mathbf{v}_b + \hat{\mathbf{v}}_c + \mathbf{K}_1 \tilde{\mathbf{p}}_b, \tag{6.32a}$$

$$\dot{\hat{\mathbf{v}}}_c = \mathbf{K}_2 \tilde{\mathbf{p}}_b, \tag{6.32b}$$

where $\mathbf{K}_1$ and $\mathbf{K}_2$ are observer gains, $\tilde{\mathbf{p}}_b = \mathbf{p}_b - \hat{\mathbf{p}}_b$ is the estimation error of the position, and we let $\tilde{\mathbf{v}}_c = \mathbf{v}_c - \hat{\mathbf{v}}_c$ be the estimation error of the ocean-current velocity.

Inserting for the observer (6.32) and the barycenter system equations (6.4), the estimation-error dynamics are given by

$$\begin{bmatrix} \dot{\tilde{\mathbf{p}}}_b \\ \dot{\tilde{\mathbf{v}}}_c \end{bmatrix} = \begin{bmatrix} -\mathbf{K}_1 & \mathbb{I} \\ -\mathbf{K}_2 & \mathbf{0} \end{bmatrix} \begin{bmatrix} \tilde{\mathbf{p}}_b \\ \tilde{\mathbf{v}}_c \end{bmatrix}, \tag{6.33}$$

which is a GES linear system if the gain matrices $\mathbf{K}_1$ and $\mathbf{K}_2$ are chosen positive definite.

To apply the observer, we insert the estimate $\hat{\mathbf{v}}_c$ for the ocean current $\mathbf{v}_c$ in (6.23):

$$\dot{\mathbf{v}}_{LOS} = \dot{\mathbf{v}}_{LOS,d} + \mathbf{\Lambda}_{LOS}(\mathbf{v}_{LOS,d} - \mathbf{v}_b - \hat{\mathbf{v}}_c). \tag{6.34}$$

The full closed-loop error system consists of the control error $\tilde{\mathbf{v}}_b = \mathbf{v}_b + \mathbf{v}_c - \mathbf{v}_{LOS,d}$ and the observer errors $\tilde{\mathbf{p}}_b^{\mathrm{T}}$ and $\tilde{\mathbf{v}}_c$. First, the path-following task acceleration (6.24) with (6.34) is applied to barycenter system (6.4), which yields

$$\dot{\tilde{\mathbf{v}}}_b = -\mathbf{\Lambda}_{LOS}\tilde{\mathbf{v}}_b + \mathbf{\Lambda}_{LOS}\tilde{\mathbf{v}}_c. \tag{6.35}$$

Letting the ocean-current estimate $\hat{\mathbf{v}}_c$ be given by (6.32). The full system follows:

$$\begin{bmatrix} \dot{\tilde{\mathbf{v}}}_b \\ \dot{\tilde{\mathbf{p}}}_b \\ \dot{\tilde{\mathbf{v}}}_c \end{bmatrix} = \begin{bmatrix} -\mathbf{\Lambda}_{LOS} & \mathbf{0} & \mathbf{\Lambda}_{LOS} \\ \mathbf{0} & -\mathbf{K}_1 & \mathbb{I} \\ \mathbf{0} & -\mathbf{K}_2 & \mathbf{0} \end{bmatrix} \begin{bmatrix} \tilde{\mathbf{v}}_b \\ \tilde{\mathbf{p}}_b \\ \tilde{\mathbf{v}}_c \end{bmatrix}, \tag{6.36}$$

Lemma 6.2. *Let $\mathbf{\Lambda}_{LOS}$, $\mathbf{K}_1$ and $\mathbf{K}_2$ be positive definite matrices. Then, the origin $[\tilde{\mathbf{v}}_b^{\mathrm{T}} \ \tilde{\mathbf{p}}_b^{\mathrm{T}} \ \tilde{\mathbf{v}}_c^{\mathrm{T}}]^{\mathrm{T}} = \mathbf{0}$ is a uniformly globally exponentially stable (UGES) equilibrium of the closed-loop error system* (6.36).

Proof. The proof follows from the separation principle.

The full closed-loop system (6.36) is block-triangular with blocks

$$-\mathbf{\Lambda}_{LOS} \quad \text{and} \quad \begin{bmatrix} -\mathbf{K}_1 & \mathbb{I} \\ -\mathbf{K}_2 & \mathbf{0} \end{bmatrix}.$$

The union of the eigenvalues of the controller given by the three equations (6.3), (6.24), and (6.23) and the observer (6.32) gives the eigenvalues of the full error system. Hence, the full system is stable because the controller and the observer are separately stable under the positive definite gain matrix assumptions. □

6.6 Obstacle avoidance

We propose two different methods for obstacle avoidance. The first method is directly adapted from Matouš, Pettersen, Varagnolo and Paliotta (2023b) and involves using a planar collision cones method at the path-following stage of the NSB method. An

advantage of this method is that the fleet keeps its formation throughout the avoidance maneuver and the method works well with moving obstacles. A possible disadvantage is that the method only works in the horizontal (xy)-plane, and may lead to excessive avoidance maneuvers in cases where the obstacles could be easier avoided in the z-direction.

The second method is directly adapted from Arrichiello et al. (2006). It involves merging the inter-vehicle collision task from Section 6.2 and obstacle avoidance into one task. In this approach, the joint inter-vehicle and external obstacle collision avoidance tasks are now treated as distributed individual tasks for each vehicle instead of one centralized task. Some advantages are that obstacle avoidance now is the highest priority task, the formulation inherently allows for multiple obstacles and obstacle avoidance can now be conducted in all three directions rather than only the plane.

The second approach prioritizes obstacle avoidance over formation keeping, allowing the fleet to split up in order to avoid obstacles. While this approach may increase the safety of the fleet, it comes with both advantages and disadvantages. On the one hand, only the vehicle in danger of collision needs to make an avoidance maneuver, enabling a quicker return to the desired path, as each individual vehicle can avoid the obstacle with a smaller margin than the fleet would need if it were to avoid the obstacle in formation. On the other hand, splitting up the formation during an obstacle avoidance maneuver may lead to vehicles being out of communication range from each other, making it difficult to return to formation.

Both approaches have advantages and disadvantages, and different behaviors when encountering obstacles. The choice of collision avoidance method will depend on the application and desired behavior.

6.6.1 Collision cones

The first obstacle avoidance method is based on the collision cones concept and enables the fleet to avoid external obstacles while keeping the formation. The approach mitigates the issue of vehicles straying out of communication range during avoidance maneuvers. We modify the collision cones method from Matouš, Pettersen, Varagnolo

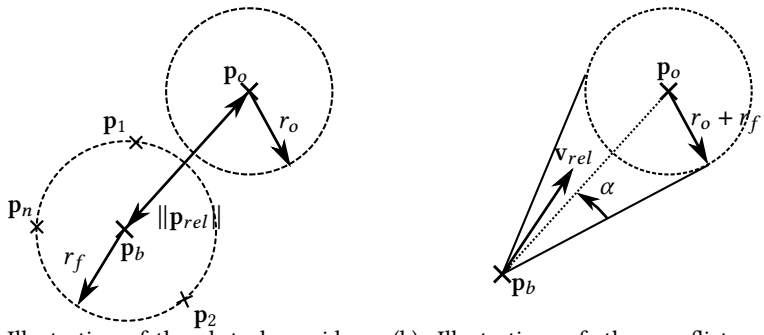

(a) Illustration of the obstacle avoidance constraint (6.37).

(b) Illustration of the conflict condition (6.38).

Figure 6.1: Illustrations of obstacle avoidance. From Lie et al. (2023), adapted from Matouš, Pettersen, Varagnolo and Paliotta (2023b).

and Paliotta (2023b) to be compatible with double integrator dynamics and focus on obstacle avoidance in the xy-plane.

We assume a constant velocity model for the obstacle. Its position and velocity vectors are denoted by $\mathbf{p}_o = [x_o, y_o, z_o]^{\mathrm{T}}$ and $\mathbf{v}_o = [\dot{x}_o, \dot{y}_o, \dot{z}_o]^{\mathrm{T}}$. We define an obstacle avoidance radius r_o that is large enough to account for both the size of the obstacle and the AUV. In addition, we define the formation radius r_f as the maximum distance between any vehicle in the fleet and the formation center, and it is assumed to be constant. We further define $\mathbf{p}_{rel} = [x_b - x_o, y_b - y_o]^{\mathrm{T}}$, $\mathbf{v}_{rel} = [\dot{x}_{LOS,d} - \dot{x}_o, \dot{y}_{LOS,d} - \dot{y}_o]^{\mathrm{T}}$, and $\dot{\mathbf{v}}_{rel} = \left[\ddot{x}_{LOS,d}, \ddot{y}_{LOS,d}\right]^{\mathrm{T}}$. Note that $\mathbf{v}_{rel}$ is defined in terms of the LOS desired velocity (6.20), so $\dot{\mathbf{p}}_{rel} \neq \mathbf{v}_{rel}$.

Collision is avoided if we ensure

$$||\mathbf{p}_{rel}|| \geq r_o + r_f \tag{6.37}$$

throughout the avoidance maneuver (see Fig. 6.1a). The formation is on a collision course (see Fig. 6.1b), if

$$|\angle(-\mathbf{p}_{rel}, \mathbf{v}_{rel})| \leq \alpha, \quad \alpha = \arcsin\Big(\frac{r_o + r_f}{||\mathbf{p}_{rel}||}\Big). \tag{6.38}$$

From (6.38), we see that for a given formation radius, the cone angle α increases as the distance decreases. The obstacle avoidance task is activated if the fleet is close enough so that $\alpha > \alpha_{\min}$. When the task is active, the x- and y-components of $\mathbf{v}_{LOS,d}$ and $\dot{\mathbf{v}}_{LOS,d}$ given by (6.20) and (6.22) are replaced with $\mathbf{v}_{OA,d}$ and $\dot{\mathbf{v}}_{OA,d}$, given by

$$\mathbf{v}_{OA,d} = ||\mathbf{v}_{rel}|| \left[\cos\left(\psi_{OA}\right), \sin\left(\psi_{OA}\right)\right]^{\mathrm{T}} + \left[\dot{x}_o, \dot{y}_o\right]^{\mathrm{T}}, \tag{6.39}$$

$$\begin{aligned}\dot{\mathbf{v}}_{OA,d} = {} & ||\dot{\mathbf{v}}_{rel}|| \left[\cos\left(\psi_{OA}\right), \sin\left(\psi_{OA}\right)\right]^{\mathrm{T}} \\ & + ||\mathbf{v}_{rel}|| \left[-\sin\left(\psi_{OA}\right)\dot{\psi}_{OA}, \cos\left(\psi_{OA}\right)\dot{\psi}_{OA}\right]^{\mathrm{T}},\end{aligned} \tag{6.40}$$

where

$$\psi_{OA} = \operatorname{atan}_2\left(y_o - y_b, x_o - x_b\right) \pm \alpha, \tag{6.41}$$

$$\dot{\psi}_{OA} = \frac{\det\left(\left[\mathbf{p}_{rel}\ \dot{\mathbf{p}}_{rel}\right]\right)}{||\mathbf{p}_{rel}||^2} \pm \dot{\alpha}, \tag{6.42}$$

$$\dot{\alpha} = \frac{r_o + r_f}{||\mathbf{p}_{rel}||^2 \sqrt{||\mathbf{p}_{rel}||^2 - \left(r_o + r_f\right)^2}} \mathbf{p}_{rel}^{\mathrm{T}} \dot{\mathbf{p}}_{rel}, \tag{6.43}$$

before entering into (6.23) or (6.28) and (6.29).

6.6.2 Individual vehicle collision avoidance

Our second obstacle avoidance approach is adapted from Arrichiello et al. (2006), but tailored to work with double-integrator dynamics. Instead of a centralized approach, the method builds the avoidance task individually for each vehicle, treating the other vehicles in the fleet as external obstacles. The task variables are similar to those defined in Section 6.2 but the controlled position $\mathbf{p}_i$ and velocity $\mathbf{v}_i$ are now those of one individual vehicle and not the entire fleet.

Let the set of obstacles O include all vehicles in the fleet and any external obstacles. Let the task variable be given by $\sigma_{1,o,i}$, where the first subscript denotes that it is the first task, the second subscript denotes the controlled vehicle, and the third subscript

is the obstacle index. The task and task Jacobians are given by

$$\sigma_{1,v,i} = \|\mathbf{p}_v - \mathbf{p}_i\|, \quad \forall i \in O : \|\mathbf{p}_v - \mathbf{p}_i\| < d_{COLAV}, \tag{6.44a}$$

$$\sigma_{1,v,i,d} = d_{COLAV}, \tag{6.44b}$$

$$\mathbf{J}_{1,v,i} = \hat{\mathbf{r}}_{v,i}^{\mathrm{T}}, \tag{6.44c}$$

$$\dot{\mathbf{J}}_{1,v,i} = \dot{\hat{\mathbf{r}}}_{v,i}^{\mathrm{T}}, \tag{6.44d}$$

where

$$\hat{\mathbf{r}}_{v,i} = \frac{\mathbf{p}_v - \mathbf{p}_i}{\|\mathbf{p}_v - \mathbf{p}_i\|}, \tag{6.45a}$$

$$\dot{\hat{\mathbf{r}}}_{v,i} = \frac{1}{\|\mathbf{p}_v - \mathbf{p}_i\|} \left(\mathbb{I}_3 - \hat{\mathbf{r}}_{v,i}\hat{\mathbf{r}}_{v,i}^{\mathrm{T}}\right) (\mathbf{v}_v + \mathbf{v}_c - \dot{\mathbf{p}}_i) \,. \tag{6.45b}$$

The obstacle absolute velocity is denoted by $\dot{\mathbf{p}}_i$, to not confuse it with the ocean-current relative velocity $\mathbf{v}_i$. We note that the pseudo-inverse of the Jacobian is given by $\mathbf{J}_{1,v,i}^{\dagger} = \mathbf{J}_{1,v,i}^{\mathrm{T}} = \hat{\mathbf{r}}_{v,i}$.

We now observe that the second derivative of the task variable is given by

$$\ddot{\sigma}_{1,v,i} = \begin{bmatrix}\mathbf{J}_{1,v,i} & -\mathbf{J}_{1,v,i}\end{bmatrix} \begin{bmatrix}\dot{\mathbf{v}}_v \\ \dot{\mathbf{v}}_i\end{bmatrix} + \begin{bmatrix}\dot{\mathbf{J}}_{1,v,i} & -\dot{\mathbf{J}}_{1,v,i}\end{bmatrix} \begin{bmatrix}\mathbf{v}_v + \mathbf{v}_c \\ \dot{\mathbf{p}}_i\end{bmatrix}, \tag{6.46}$$

which, given a desired second derivative of the task error $\ddot{\tilde{\sigma}}_{1,v,i}^{*}$, can be rearranged to find desired avoidance accelerations for each vehicle involved in the collision

$$\begin{bmatrix}\dot{\mathbf{v}}_{1,v,i} \\ \dot{\mathbf{v}}_{1,i,v}\end{bmatrix} = \frac{1}{2} \begin{bmatrix}\mathbf{J}_{1,v,i}^{\dagger} \\ -\mathbf{J}_{1,v,i}^{\dagger}\end{bmatrix} \left(\ddot{\tilde{\sigma}}_{1,v,i}^{*} - \begin{bmatrix}\dot{\mathbf{J}}_{1,v,i} & -\dot{\mathbf{J}}_{1,v,i}\end{bmatrix} \begin{bmatrix}\mathbf{v}_v + \mathbf{v}_c \\ \dot{\mathbf{p}}_i\end{bmatrix}\right). \tag{6.47}$$

Here, we applied the following relation

$$\begin{bmatrix}\mathbf{J}_{1,v,i} & -\mathbf{J}_{1,v,i}\end{bmatrix}^{\dagger} = \frac{1}{2} \begin{bmatrix}\mathbf{J}_{1,v,i}^{\dagger} \\ -\mathbf{J}_{1,v,i}^{\dagger}\end{bmatrix}. \tag{6.48}$$

The one-half constant comes from the fact that both vehicles involved in a collision

contribute to the avoidance maneuver, and consequently, each vehicle only applies half the control effort. Simulations showed that this scaling is essential for the method's success. If $\mathbf{p}_i$ is an external obstacle we do not apply the one-half scaling. After applying the SOCLIK solution, the desired COLAV acceleration is

$$\dot{\mathbf{v}}_{1,v,i} = -k_{scale}\hat{\mathbf{r}}_{v,i}\left(\lambda_{p,1}\tilde{\sigma}_{1,v,i} + \hat{\mathbf{r}}_{v,i}^{\mathrm{T}}\lambda_{d,1}\left(\mathbf{v}_v + \mathbf{v}_c - \dot{\mathbf{p}}_i\right) + \dot{\hat{\mathbf{r}}}_{v,i}^{\mathrm{T}}\left(\mathbf{v}_v + \mathbf{v}_c - \dot{\mathbf{p}}_i\right)\right), \tag{6.49}$$

where

$$k_{scale} = \begin{cases} \frac{1}{2}, & \text{Vehicle } i \text{ is part of fleet,} \\ 1, & \text{otherwise.} \end{cases} \tag{6.50}$$

The ocean-current velocity appears in this equation, but only in terms that describe the relative velocity between the vehicle and obstacle $\left(\mathbf{v}_v + \mathbf{v}_c - \dot{\mathbf{p}}_i\right)$. If the relative velocity can be measured directly, an estimate of the ocean current is not necessary. Otherwise, the ocean-current observer from Section 6.5.2 can be applied.

In the case of multiple obstacles acting simultaneously, the closest obstacle is prioritized. We apply the iterative null-space projection for each obstacle ordered by distance, with the closest obstacle first so that it has the highest priority. For instance, in the case of two obstacles in collision range, the final commanded acceleration for a vehicle v is

$$\boldsymbol{\mu}_v = \dot{\mathbf{v}}_{NSB,v} = \dot{\mathbf{v}}_{1,v,1} + \mathbf{N}_{1,v,1}\dot{\mathbf{v}}_{1,v,2} + \bar{\mathbf{N}}_{1,v,2}\left(\dot{\mathbf{v}}_{2,v} + \dot{\mathbf{v}}_{3,v}\right). \tag{6.51}$$

In this formulation, the third task acceleration is no longer orthogonal to the first task and must be projected into its null space, which results from external obstacles inducing collision avoidance maneuvers that move the barycenter of the fleet.

As discussed in both Arrichiello et al. (2006) and Antonelli and Chiaverini (2006) the null space projection of this task constrains the lower priority tasks to only produce motion tangent to the unit sphere of radius d_{COLAV} centered at the obstacle. Therefore, singular configurations exist where the desired direction from the other tasks is parallel to $\hat{\mathbf{r}}$. The vehicle will get stuck in these configurations with zero commanded acceleration. This problem is discussed in detail in Antonelli and Chiaverini (2006), and in particular, they note that the singular configuration is an unstable stationary

point, and any measurement errors or intentional actuator noise may pull the system away.

Chapter 7

Closed-Loop Analysis of the Centralized NSB Method

The closed-loop stability analysis is an essential step in the design of control systems. In this chapter, we will analyze the stability properties of the proposed formation control system for a fleet of autonomous vehicles. Specifically, we will study the stability of the formation-keeping and path-following task and also the boundedness of the internal states of the hand-position feedback-linearization model. The stability analysis will be conducted using Lyapunov theory, a powerful tool for the analysis of nonlinear systems. Most of the results from this chapter have been submitted to the 62nd IEEE Conference on Decision and Control (Lie et al.; 2023).

For the analysis, we assume that the vehicle is operating under safe conditions, that is, no collision avoidance task is active. As established in Section 6.1, the formation-keeping and path-following tasks are orthogonal because they produce common accelerations for the entire fleet and relative accelerations within the fleet. Since the collision avoidance task is inactive, the control action $\boldsymbol{\mu}$ defined in (6.3) can be simplified to

$$\boldsymbol{\mu} = \dot{\mathbf{v}}_{NSB} = \dot{\mathbf{v}}_2 + \dot{\mathbf{v}}_3, \tag{7.1}$$

where $\dot{\mathbf{v}}_2$ and $\dot{\mathbf{v}}_3$ are the task accelerations given by (6.17) and (6.24). As a result of the orthogonality, there exist the following independence relations

$$\ddot{\boldsymbol{\sigma}}_2 = \mathbf{J}_2\dot{\mathbf{v}}_2 + \dot{\mathbf{J}}_2\dot{\mathbf{v}}_3 = \mathbf{J}_2\dot{\mathbf{v}}_2, \tag{7.2}$$

$$\dot{\mathbf{v}}_b = \frac{1}{n}\sum_{i=1}^{n}(\dot{\mathbf{v}}_2 + \dot{\mathbf{v}}_3) = \frac{1}{n}\sum_{i=1}^{n}\dot{\mathbf{v}}_3 = \dot{\mathbf{v}}_{LOS}. \tag{7.3}$$

Consequently, the stability properties of each task can be studied independently.

The chapter is organized as follows. Section 7.1 investigates the closed-loop stability properties of the formation-keeping task using Lyapunov theory and LaSalle's invariance principle. Section 7.2 investigates the closed-loop stability properties of the path-following task using cascaded system theory. Finally, Section 7.3 analyzes the boundedness of the internal states of the hand-position feedback linearized system under the NSB controller.

7.1 Stability of the formation-keeping task

We recall the formation-keeping task variable $\boldsymbol{\sigma}_2$ defined in (6.11) and its desired value $\boldsymbol{\sigma}_{d,2}$ defined in (6.12). This section analyses the stability properties of the task error $\tilde{\boldsymbol{\sigma}}_2 = \boldsymbol{\sigma}_2 - \boldsymbol{\sigma}_{d,2}$ using Lyapunov theory.

The closed-loop dynamics of the formation-task error are found by inserting the task acceleration (6.17) into the second derivative of the task variable (7.2). The resulting closed-loop system is given by

$$\dddot{\tilde{\boldsymbol{\sigma}}}_2 = -v_{2_{\max}}\,\mathrm{sat}\big(\boldsymbol{\Lambda}_{p,2}\tilde{\boldsymbol{\sigma}}_2\big) - \boldsymbol{\Lambda}_{d,2}\ddot{\tilde{\boldsymbol{\sigma}}}_2. \tag{7.4}$$

We note the following relation which will be used to find a suitable Lyapunov function

$$\frac{\partial}{\partial \mathbf{x}}\log\left(\cosh\|\mathbf{x}\|\right) = \mathbf{x}\frac{\tanh\|\mathbf{x}\|}{\|\mathbf{x}\|} = \mathrm{sat}\big(\mathbf{x}\big). \tag{7.5}$$

Theorem 7.1. *Let $\boldsymbol{\Lambda}_{p,2}$, $\boldsymbol{\Lambda}_{d,2}$ be two symmetric positive definite matrices so that the product $\boldsymbol{\Lambda}_{p,2}\boldsymbol{\Lambda}_{d,2}$ is symmetric positive definite. Then, $\left[\dot{\tilde{\boldsymbol{\sigma}}}_2^{\mathrm{T}},\ \tilde{\boldsymbol{\sigma}}_2^{\mathrm{T}}\right]^{\mathrm{T}} = \mathbf{0}$ is a uniformly*

globally asymptotically stable (UGAS) equilibrium of the closed-loop system (7.4).

Proof. Consider the Lyapunov function

$$V(\tilde{\boldsymbol{\sigma}}_2, \dot{\tilde{\boldsymbol{\sigma}}}_2) = v_{2,\max} \log\left(\cosh \|\boldsymbol{\Lambda}_{p,2}\tilde{\boldsymbol{\sigma}}_2\|\right) + \frac{1}{2}\dot{\tilde{\boldsymbol{\sigma}}}_2^{\mathrm{T}}\boldsymbol{\Lambda}_{p,2}\dot{\tilde{\boldsymbol{\sigma}}}_2. \tag{7.6}$$

The time derivative of V along the trajectories of (7.4) is given by

$$\begin{aligned}\dot{V} &= v_{2,\max}\mathrm{sat}\left(\boldsymbol{\Lambda}_{p,2}\tilde{\boldsymbol{\sigma}}_2\right)^{\mathrm{T}}\boldsymbol{\Lambda}_{p,2}\dot{\tilde{\boldsymbol{\sigma}}}_2 \\ &\quad - \dot{\tilde{\boldsymbol{\sigma}}}_2^{\mathrm{T}}\boldsymbol{\Lambda}_{p,2}\left(v_{2,\max}\mathrm{sat}\left(\boldsymbol{\Lambda}_{p,2}\tilde{\boldsymbol{\sigma}}_2\right) + \boldsymbol{\Lambda}_{d,2}\dot{\tilde{\boldsymbol{\sigma}}}_2)\right), \\ &= -\dot{\tilde{\boldsymbol{\sigma}}}_2^{\mathrm{T}}\boldsymbol{\Lambda}_{p,2}\boldsymbol{\Lambda}_{d,2}\dot{\tilde{\boldsymbol{\sigma}}}_2.\end{aligned} \tag{7.7}$$

Let $S = \{\left[\dot{\tilde{\boldsymbol{\sigma}}}_2^{\mathrm{T}},\ \tilde{\boldsymbol{\sigma}}_2^{\mathrm{T}}\right]^{\mathrm{T}} \in \mathbb{R}^{6(n-1)} : \dot{V} = 0\}$. Because of the dynamics (7.4), no other solution can stay identically in S, other than the trivial solution $\left[\dot{\tilde{\boldsymbol{\sigma}}}_2^{\mathrm{T}},\ \tilde{\boldsymbol{\sigma}}_2^{\mathrm{T}}\right]^{\mathrm{T}} \equiv \mathbf{0}$. Thus, the origin is globally asymptotically stable according to (Khalil; 2002, Corollary 4.2). Furthermore, because (7.4) is time-invariant, the equilibrium is UGAS. □

7.2 Stability of the path-following task

This section studies the stability of the path-following error $\mathbf{p}_b^p$ defined in (4.3). The section will use cascaded-system theory and rely on results from Matouš, Pettersen, Varagnolo and Paliotta (2023b).

First, we define the error system. Let the derivative of the path-following error be given by

$$\begin{aligned}\dot{\mathbf{p}}_b^p &= f(\cdot) + g(\cdot)\tilde{\mathbf{v}}_b, \\ &= \mathbf{R}_p^{\mathrm{T}}(\mathbf{v}_b + \mathbf{v}_c - \dot{\mathbf{p}}_p) + \left(\mathbf{S}(\omega_p\xi)\right)^{\mathrm{T}}\mathbf{R}_p^{\mathrm{T}}(\mathbf{p}_b - \mathbf{p}_p), \\ &= \mathbf{R}_p^{\mathrm{T}}(\mathbf{v}_{LOS,d} - \dot{\mathbf{p}}_p) - \mathbf{S}(\omega_p\xi)\mathbf{p}_b^p + \mathbf{R}_p^{\mathrm{T}}\tilde{\mathbf{v}}_b,\end{aligned} \tag{7.8a}$$

$$\dot{\tilde{\mathbf{v}}}_b = h(\tilde{\mathbf{v}}_b, \cdot), \tag{7.8b}$$

where $\tilde{\mathbf{v}}_b = \mathbf{v}_b + \mathbf{v}_c - \mathbf{v}_{LOS,d}$ is the barycenter-velocity error. We recall that $\mathbf{v}_{LOS,d}$ is

given by (8.15). The dynamics (7.8b) of $\tilde{\mathbf{v}}_b$ differ depending on the choice of ocean-current compensation method. They are given by (6.31) or (6.36) for the choice of integral compensation or ocean-current observer, respectively. For both choices, the origin $\tilde{\mathbf{v}}_b = \mathbf{0}$ is an exponentially stable equilibrium as proved in Section 6.5.1 and 6.5.2.

Theorem 7.2. *Let $\tilde{\mathbf{v}}_b = \mathbf{0}$ be a uniformly globally exponentially stable (UGES) equilibrium of* (7.8b)*. Then, $[\tilde{\mathbf{v}}_b^{\mathrm{T}}, (\mathbf{p}_b^p)^{\mathrm{T}}]^{\mathrm{T}}$ is a USGES and UGAS equilibrium of the system* (7.8).

Proof. The system (7.8) is in a cascaded form where the velocity error $\tilde{\mathbf{v}}$ from (7.8b) perturbs the system (7.8a). By assumption, the dynamics of (7.8b) are UGES. The nominal system (7.8a) with $\tilde{\mathbf{v}}_b = 0$ and path-parameter update $\dot{\xi}$ given by (6.27) was proved to be USGES in Matouš, Pettersen, Varagnolo and Paliotta (2023b) using the Lyapunov function

$$V(\mathbf{p}_b^p) = \frac{1}{2}\left(\mathbf{p}_b^p\right)^{\mathrm{T}} \mathbf{p}_b^p. \tag{7.9}$$

For completeness, we present the proof here. The time derivative of V is given by

$$\begin{aligned} \dot{V} &= (\mathbf{p}_b^p)^T \left(\mathbf{R}_p^T(\mathbf{v}_{LOS,d} - \dot{\mathbf{p}}_p) - \mathbf{S}(\omega_p \dot{\xi})\mathbf{p}_b^p\right), \\ &= (\mathbf{p}_b^p)^T \mathbf{R}_p^T(\mathbf{v}_{LOS,d} - \dot{\mathbf{p}}_p). \end{aligned} \tag{7.10}$$

We note that $\mathbf{R}_p^T \dot{\mathbf{p}}_p$ is the derivative of the origin of the path-tangential coordinate frame expressed in path-tangential coordinates. By the definition of the frame, the direction of the derivative is the x-direction. Thus, the following holds

$$\mathbf{R}_p^T \dot{\mathbf{p}}_p = \left\| \frac{\partial \mathbf{p}_p}{\partial \xi} \right\| \dot{\xi} \, [1, 0, 0]^{\mathrm{T}}. \tag{7.11}$$

Furthermore, inserting for $\dot{\xi}$ from (6.27) we get

$$\mathbf{R}_p^T \dot{\mathbf{p}}_p = U_{LOS} \left(\frac{\Delta(\mathbf{p}_b^p)}{D} + k_\xi \frac{x_b^p}{\sqrt{1 + (x_b^p)^2}} \right) [1, 0, 0]^{\mathrm{T}}. \tag{7.12}$$

We recall the LOS velocity

$$\mathbf{v}_{LOS,d} = \mathbf{R}_p \left[\Delta(\mathbf{p}_b^p), -y_b^p, -z_b^p\right]^\mathrm{T} \frac{U_{LOS}}{D}. \tag{7.13}$$

After cancellations in the x-coordinate, the derivative of the Lyapunov function becomes

$$\dot{V} = -U_{LOS}\left(k_\xi \frac{(x_b^p)^2}{\sqrt{1+(x_b^p)^2}} + \frac{(y_b^p)^2}{D} + \frac{(z_b^p)^2}{D}\right). \tag{7.14}$$

For any $\mathbf{p}_b^p \in \{\mathbf{p}_b^p \in \mathbb{R}^3 : \|\mathbf{p}_b^p\| \leq r\}$ we have

$$\dot{V} \leq -U_{LOS} k_r \|\mathbf{p}_b^p\|^2, \tag{7.15}$$

where $k_r = \min\left\{k_\xi \frac{1}{\sqrt{1+r^2}}, \frac{1}{\sqrt{\Delta_0+2r^2}}\right\}$. All assumptions of (Pettersen; 2017, Theorem 5) are thus satisfied, and the origin of the nominal system is USGES.

Therefore, according to (Pettersen; 2017, Proposition 9) the cascaded system is USGES and UGAS if the following two assumptions hold

1. There exist constants $c_1,\ c_2,\ \eta > 0$ such that

$$\left\|\frac{\partial V}{\partial \mathbf{p}_b^p}\right\| \left\|\mathbf{p}_b^p\right\| \leq c_1 V(\mathbf{p}_b^p), \quad \forall \|\mathbf{p}_b^p\| \geq \eta, \tag{7.16}$$

$$\left\|\frac{\partial V}{\partial \mathbf{p}_b^p}\right\| \leq c_2, \quad \forall \|\mathbf{p}_b^p\| \leq \eta. \tag{7.17}$$

2. There exist two continuous functions $\alpha_1,\ \alpha_2 : \mathbb{R}_{\geq 0} \longrightarrow \mathbb{R}_{\geq 0}$, such that $\mathbf{g}(\cdot)$ satisfies

$$\|g(\cdot)\| \leq \alpha_1(\|\tilde{\mathbf{v}}\|) + \alpha_2(\|\tilde{\mathbf{v}}\|)\|\mathbf{p}_b^p\|. \tag{7.18}$$

Because $\|\partial V/\partial \mathbf{p}_b^p\| = \|\mathbf{p}_b^p\|$, 1) holds with $c_1 = 2,\ c_2 = \eta$ for any $\eta \in \mathbb{R}_{\geq 0}$.
Equation (7.18) is satisfied with $\alpha_1(\|\tilde{\mathbf{v}}\|) = 1, \alpha_2(\|\tilde{\mathbf{v}}\|) = 0$, because $\|g(\cdot)\| = \|\mathbf{R}_p^\mathrm{T}\| =$

1. As a result, all assumptions of (Pettersen; 2017, Proposition 9) are satisfied, and the origin of the closed-loop path-following system (7.8) is USGES and UGAS. □

7.3 Boundedness of the internal states

This section will investigate the boundedness of the internal states of the hand-position feedback linearization controller (3.8). The internal states are $\mathbf{R}$ and $\boldsymbol{\omega}$, however only $\boldsymbol{\omega}$ can grow unbounded because $\mathbf{R}$ is defined on the closed space $\mathbf{SO}(3)$. The proof will closely follow (Matouš, Paliotta, Pettersen and Varagnolo; 2023, Proposition 2 and 3), but we include all steps for completeness. This entire section considers a single vehicle so subscripts will be omitted for simplicity.

First, Proposition 2 from Matouš, Paliotta, Pettersen and Varagnolo (2023) holds for our NSB controller without modification, so we simply restate it here. By the choice of the control law (3.6), the dynamics of the roll rate no longer depend on the other angular velocities. From (3.8d), we get

$$\begin{aligned} \dot{p} &= -\mathbf{e}_1^{\mathrm{T}} \left(\mathcal{D}_{\omega}(\zeta) + \mathbf{M}'_{22} \left(W z_{gb} \mathbf{e}_3 \times \mathbf{R}^{\mathrm{T}} \mathbf{e}_3 \right) \right) \\ &= -\frac{d_{44}}{m_{44}} p - \frac{1}{m_{44}} \mathbf{e}_1^{\mathrm{T}} \left(W z_{gb} \mathbf{e}_3 \times \mathbf{R}^{\mathrm{T}} \mathbf{e}_3 \right). \end{aligned} \tag{7.19}$$

We define

$$a_x = \frac{d_{44}}{m_{44}}, \quad b_x = \frac{W z_{gb}}{m_{44}}, \tag{7.20}$$

and restate the following proposition:

Proposition 7.3 (Proposition 2, Matouš, Paliotta, Pettersen and Varagnolo (2023))**.** *The roll rate dynamics are bounded if $a_x > 0$. Specifically, the trajectory $p(t)$ satisfies*

$$|p(t)| \leq |p(0)| \mathrm{e}^{-a_x t} + \frac{b_x}{a_x} \left(1 - \mathrm{e}^{-a_x t} \right). \tag{7.21}$$

Proof. Consider the following two functions

$$V_p = \frac{1}{2}p^2, \qquad W_p = \sqrt{2V_p}. \tag{7.22}$$

The following inequality holds for the derivative of W_p along the trajectories of p

$$\dot{W}_p \leq -a_x W_p + b_x. \tag{7.23}$$

By applying the comparison lemma, we get

$$W_p(t) = |p(t)| \leq |p(0)|\, \mathrm{e}^{-a_x t} + \frac{b_x}{a_x}\left(1 - \mathrm{e}^{-a_x t}\right), \tag{7.24}$$

which concludes the proof. □

Now, we investigate the boundedness of q and r. The proof closely follows Proposition 3 from Matouš, Paliotta, Pettersen and Varagnolo (2023), but we include some of the omitted steps and modify the proof to work with our NSB controller (6.3).

The dynamics for q and r are obtained from (3.8d):

$$\begin{bmatrix} \dot{q} \\ \dot{r} \end{bmatrix} = \begin{bmatrix} 0 & 0 & -\frac{1}{h} \\ 0 & \frac{1}{h} & 0 \end{bmatrix} \left(\mathbf{R}^{\mathrm{T}}\boldsymbol{\mu} + \mathcal{D}_{\boldsymbol{\nu}}(\boldsymbol{\zeta}_r) + C_{\boldsymbol{\nu}}(\boldsymbol{\zeta}_r) - \boldsymbol{\omega} \times \mathbf{R}^{\mathrm{T}}\mathbf{v} \right). \tag{7.25}$$

The linear velocities can be expressed in terms of the external states

$$\boldsymbol{\nu}_r = \boldsymbol{\nu}_e - \boldsymbol{\omega} \times \mathbf{L}, \tag{7.26}$$

with the external part of the linear velocities given by

$$\boldsymbol{\nu}_e = \mathbf{R}^{\mathrm{T}}\mathbf{v}. \tag{7.27}$$

The norm of $\boldsymbol{\nu}_e$ can be bounded by

$$\|\boldsymbol{\nu}_e\| \leq \|\tilde{\boldsymbol{\nu}}_e\| + \|\dot{\mathbf{p}}_d - \mathbf{v}_c\|, \tag{7.28}$$

where $\dot{\mathbf{p}}_d$ is the derivative of the desired position $\mathbf{p}_d = \mathbf{p}_p(\xi) + \mathbf{R}_p \mathbf{p}_f^f$ and $\tilde{\boldsymbol{\nu}}_e$ is a velocity error term due to transients in the path-following and formation-keeping tasks. Under the controller (6.3) with the formation-keeping acceleration (6.17) and path-following acceleration (6.24) the external dynamics are UGAS following Theorems 7.1 and 7.2. Consequently, $\|\tilde{\boldsymbol{\nu}}_e\|$ will asymptotically converge to zero.

Note that because the path function is continuous and infinitely differentiable and thanks to the choice of the path parameter update law (6.27), the time-derivatives of $\mathbf{p}_d$ are bounded

$$\|\dot{\mathbf{p}}_d(t)\| \leq \bar{\dot{\mathbf{p}}}_d, \quad \|\ddot{\mathbf{p}}_d(t)\| \leq \bar{\ddot{\mathbf{p}}}_d. \tag{7.29}$$

Consider the Lyapunov function candidate

$$V_\omega = \frac{1}{2}(q^2 + r^2). \tag{7.30}$$

We let $\hat{\boldsymbol{\omega}} = [q,\ r]^T$. The derivative is given by

$$\begin{aligned}
\dot{V}_\omega = &- a_y q^2 - a_z r^2 + a_{xyz} pqr \\
&+ a_{ye} \boldsymbol{\nu}_{e_1} q^2 + a_{xy} \boldsymbol{\nu}_{e_2} pq + a_{xz} \boldsymbol{\nu}_{e_3} pr + a_{ze} \boldsymbol{\nu}_{e_1} r^2 \\
&+ a_{ey} \boldsymbol{\nu}_{e_1} \boldsymbol{\nu}_{e_3} q + a_{ley} \boldsymbol{\nu}_{e_3} q + a_{ez} \boldsymbol{\nu}_{e_1} \boldsymbol{\nu}_{e_2} r + a_{lez} \boldsymbol{\nu}_{e_2} r \\
&+ \begin{bmatrix} 0 & -\frac{r}{h} & +\frac{q}{h} \end{bmatrix} (\boldsymbol{\omega} \times \boldsymbol{\nu}_e) + \begin{bmatrix} 0 & \frac{r}{h} & -\frac{q}{h} \end{bmatrix} \mathbf{R}^T \boldsymbol{\mu}.
\end{aligned} \tag{7.31}$$

The coefficient definitions are found in Appendix A. We bound the derivative by the following inequality

$$\begin{aligned}
\dot{V}_\omega \leq &- a_y q^2 - a_z r^2 + a_{xyz} pqr \\
&+ a_{ye} \boldsymbol{\nu}_{e_1} q^2 + a_{xy} \boldsymbol{\nu}_{e_2} pq + a_{xz} \boldsymbol{\nu}_{e_3} pr + a_{ze} \boldsymbol{\nu}_{e_1} r^2 \\
&+ a_{ey} \boldsymbol{\nu}_{e_1} \boldsymbol{\nu}_{e_3} q + a_{ez} \boldsymbol{\nu}_{e_1} ve_2 r \\
&+ \|\boldsymbol{\nu}_e\| \|\hat{\boldsymbol{\omega}}\| \left(\frac{\|\boldsymbol{\omega}\|}{h} + a_e \right) + \|\hat{\boldsymbol{\omega}}\| \frac{\|\mu\|}{h},
\end{aligned} \tag{7.32}$$

with $a_e = \max\{a_{ley}, a_{lez}\}$.

Theorem 7.4. *Let us define*

$$\bar{p} = b_x/a_x, \qquad \bar{\mathbf{v}} = \max_{t\in\mathbb{R}_{\geq 0}} \left\|\dot{\mathbf{p}}_{\mathrm{d},i}(t) - \mathbf{v}_c\right\|, \tag{7.33a}$$

$$\bar{\alpha}_y = a_y - \left(\frac{1}{h}\,\bar{\mathbf{v}} + \frac{1}{2}\left|a_{xyz}\bar{p}\right| + \left|a_{ye}\bar{\mathbf{v}}\right|\right), \tag{7.33b}$$

$$\bar{\alpha}_z = a_z - \left(\frac{1}{h}\,\bar{\mathbf{v}} + \frac{1}{2}\left|a_{xyz}\bar{p}\right| + |a_{ze}\bar{\mathbf{v}}|\right). \tag{7.33c}$$

The angular rate dynamics are ultimately bounded if $a_x, \bar{\alpha}_y, \bar{\alpha}_z > 0$.

Proof. Consider the Lyapunov function V_ω and the bound on its derivative in (7.32). We apply the following identities

$$\|\boldsymbol{\omega}\|\|\hat{\boldsymbol{\omega}}\| \leq (|p| + \|\hat{\boldsymbol{\omega}}\|)\|\hat{\boldsymbol{\omega}}\|, \tag{7.34a}$$

$$|pqr| \leq \frac{1}{2}|p|(q^2 + r^2), \tag{7.34b}$$

to derive the following (looser) upper bound on $\dot{V}_\omega$

$$\dot{V}_\omega \leq -\alpha_y q^2 - \alpha_z r^2 + G\left(\boldsymbol{\nu}_e, \boldsymbol{\omega}, \boldsymbol{\mu}\right). \tag{7.35}$$

The coefficients α_y and α_z are given by

$$\alpha_y = a_y - \left(\frac{1}{h}\|\boldsymbol{\nu}_e\| + \frac{1}{2}|a_{xyz}||p| + |a_{ye}|\|\boldsymbol{\nu}_e\|\right), \tag{7.36a}$$

$$\alpha_z = a_z - \left(\frac{1}{h}\|\boldsymbol{\nu}_e\| + \frac{1}{2}|a_{xyz}||p| + |a_{ze}|\|\boldsymbol{\nu}_e\|\right), \tag{7.36b}$$

and $G(\cdot)$ represents the terms that grow at most linearly with q and r

$$\begin{aligned} G(\boldsymbol{\nu}_e, \boldsymbol{\omega}, \mu) = &\left(\left(\frac{|p|}{h} + a_e\right)\|\boldsymbol{\nu}_e\| + \frac{\|\mu\|}{h}\right)\|\hat{\boldsymbol{\omega}}\| \\ &+ \left(a_{ey}\boldsymbol{\nu}_{e_1}\boldsymbol{\nu}_{e_3} + a_{xy}\boldsymbol{\nu}_{e_2}p\right)q + \left(a_{ez}\boldsymbol{\nu}_{e_1}\boldsymbol{\nu}_{e_2} + a_{xz}\boldsymbol{\nu}_{e_3}p\right)r. \end{aligned} \tag{7.37}$$

From Proposition 7.3, we can conclude that if $a_x > 0$, then

$$\lim_{t\to\infty} |p(t)| \leq \bar{p}. \tag{7.38}$$

The limit converges exponentially. As a result, in the limit, $\bar{\alpha}_y$ and $\bar{\alpha}_z$ from (7.33) form lower bounds on α_y and α_z from (7.36)

$$\lim_{t\to\infty} \alpha_y \geq \bar{\alpha}_y, \quad \lim_{t\to\infty} \alpha_z \geq \bar{\alpha}_z. \tag{7.39}$$

Therefore, if $\bar{\alpha}_y, \bar{\alpha}_z > 0$, then there exists a finite time T after which $\alpha_y, \alpha_z > 0$.

We examine the linear term $G(\cdot)$. We note that the control action $\boldsymbol{\mu}$ is bounded by

$$\|\boldsymbol{\mu}(t)\| \leq \beta(\mathbf{p}_b(0), \tilde{\boldsymbol{\sigma}}_2(0), t) + \|\ddot{\mathbf{p}}_d\|, \tag{7.40}$$

where $\beta(\cdot, t)$ is a class $\mathcal{KL}$ function (Khalil; 2002, definition 4.3) such that

$$\lim_{t\to\infty} \beta(\mathbf{p}_b(0), \tilde{\boldsymbol{\sigma}}_2(0), t) = 0. \tag{7.41}$$

Inserting for this bound as well as (7.29), $G(\cdot)$ is bounded as follows

$$\begin{aligned} G(\boldsymbol{\nu}_e, \boldsymbol{\omega}, \mu) \leq \bar{G}(\boldsymbol{\omega}) &:= \left(\left(\frac{\hat{p}}{h} + a_e\right)\hat{\boldsymbol{\nu}}_e + \frac{\beta(\cdot,0) + \ddot{\bar{\mathbf{p}}}_d}{h}\right)\|\hat{\boldsymbol{\omega}}\| \\ &\quad + \left(a_{ey}\hat{\boldsymbol{\nu}}_e^2 + a_{xy}\hat{\boldsymbol{\nu}}_e\hat{p}\right)q + \left(a_{ez}\hat{\boldsymbol{\nu}}_e^2 + a_{xz}\hat{\boldsymbol{\nu}}_e\hat{p}\right)r \\ &\leq a_G\|\hat{\boldsymbol{\omega}}\|, \end{aligned} \tag{7.42}$$

where $\hat{\boldsymbol{\nu}}_e = \bar{\boldsymbol{\nu}}_e + \|\boldsymbol{\nu}_e(0)\|$ is an upper bound on $\|\boldsymbol{\nu}_e\|$ and $\hat{p} = \bar{p} + |p(0)|$ is an upper bound on $|p|$ and

$$a_G = \left|\left(\frac{\hat{p}}{h} + a_e\right)\hat{\boldsymbol{\nu}}_e + \frac{\beta(\cdot,0) + \ddot{\bar{\mathbf{p}}}_d}{h}\right| + \max\left\{\left|a_{ey}\hat{\boldsymbol{\nu}}_e^2 + a_{xy}\hat{\boldsymbol{\nu}}_e\hat{p}\right|, \left|a_{ez}\hat{\boldsymbol{\nu}}_e^2 + a_{xz}\hat{\boldsymbol{\nu}}_e\hat{p}\right|\right\}. \tag{7.43}$$

We investigate the candidate Lyapunov function for $t < T$. Since α_y and α_z may be negative, we cannot prove boundedness. However, we note that the derivative of

the Lyapunov function (7.35) has the following form

$$\dot{V}_\omega \leq k_1 \|\hat{\boldsymbol{\omega}}\|^2 + a_G \|\hat{\boldsymbol{\omega}}\|, \tag{7.44}$$

where k_1 is a positive constant. We can therefore conclude that the dynamics of q and r are forward complete (Angeli and Sontag; 1999), which means that there exists a solution globally, for positive time.

For $t \geq T$, $\dot{V}_\omega$ has the following form

$$\dot{V}_\omega \leq -\alpha_y q^2 - \alpha_z r^2 + a_G \|\hat{\boldsymbol{\omega}}\|. \tag{7.45}$$

For sufficiently large angular velocities, the quadratic term will dominate the linear term $a_G \|\hat{\boldsymbol{\omega}}\|$, and q and r will remain bounded. □

Chapter 8

The Distributed NSB Method

The second-order NSB method as presented so far is a centralized method. Consequently, it might be difficult to implement the control law in practice because it would require perfect and continuous communication. In this chapter, we propose a novel distributed version of the controller. Other distributed versions of the algorithm have been developed, and in particular, Matouš, Pettersen, Varagnolo and Paliotta (2023a) formulated a distributed version of the first-order NSB method. For comparison, we also extend this method to work in the second-order setting.

In the novel distributed formulation, the key insight is recognizing that the formation-keeping task can be treated as a consensus algorithm on a fully-connected graph. Consensus methods, discussed in Section 1.2, are widely used in distributed control laws for formation control. Leveraging this concept, the proposed distributed version of the NSB method for AUVs presented herein offers a notable advantage. It only necessitates the communication of the path-progress variable ξ with neighboring vehicles, along with measurements of their relative positions and velocities. This approach significantly reduces the communication requirements while still achieving effective formation control.

The subsequent sections detail each of the tasks collision avoidance, formation keeping, and path following for the novel distributed method. The combined control

law for vehicle i is given by

$$\boldsymbol{\mu}_i = \dot{\mathbf{v}}_{1,i} + \mathbf{N}_{1,i}(\dot{\mathbf{v}}_{2,i} + \mathbf{N}_{2,i}\dot{\mathbf{v}}_{3,\{i,\mathcal{N}_i\}}), \tag{8.1}$$

where each of the task accelerations $\dot{\mathbf{v}}_{k,i}, k \in \{1, 2, 3\}$ will be detailed in the following sections. $\dot{\mathbf{v}}_{3,\{i,\mathcal{N}_i\}}$ are the LOS accelerations from vehicle i and all its neighbors.

In the final section, we demonstrate how the distributed first-order method can be extended to work with the second-order NSB algorithm. This extension provides an alternative approach to transitioning from a centralized to a distributed controller and demonstrates the main ideas of how it has been done in earlier works.

8.1 Collision-avoidance task

For the collision avoidance task, we leverage that the collision avoidance task from Arrichiello et al. (2006), which was rewritten for our second-order NSB method in Section 6.6.2, is inherently distributed. The task can be applied without any modifications and ensures collision safety from other vehicles within the fleet and external obstacles. A drawback of the task formulation that is even more critical in a distributed setting is that vehicles may leave communication range when avoiding external obstacles. This drawback could be amended by modifying the task to also activate when the distance between two neighboring vehicles increases above a communication range threshold d_{COM}.

8.2 Formation-keeping task

In this section, we show that the formation-keeping task is in fact a consensus law. Consensus laws are known to be inherently distributed.

We restate the nominal formation-keeping acceleration (6.16)

$$\dot{\mathbf{v}}_2 = \mathbf{J}_2^{\dagger}\left(\ddot{\boldsymbol{\sigma}}_{d,2} - \boldsymbol{\Lambda}_{p,2}\tilde{\boldsymbol{\sigma}}_2 - \boldsymbol{\Lambda}_{d,2}\dot{\tilde{\boldsymbol{\sigma}}}_2\right). \tag{8.2}$$

The key insight lies in the following relationship: $\mathbf{J}_2^\dagger \mathbf{J}_2 = \frac{1}{n}(\mathbf{L}_F \otimes \mathbf{I}_3)$, where $\mathbf{L}_F$ is the Laplacian matrix of the fully connected graph consisting of all agents. The task variables can be written as

$$\sigma_2 = \mathbf{J}_2 \mathbf{p}, \quad \dot{\sigma}_2 = \mathbf{J}_2 \mathbf{v}, \quad \ddot{\sigma}_2 = \mathbf{J}_2 \dot{\mathbf{v}}. \tag{8.3}$$

Then, if the gain matrices are chosen as multiples of the identity matrix $\mathbf{\Lambda} = \lambda \mathbf{I}$, the SOCLIK equation (6.16) can be rewritten as

$$\dot{\mathbf{v}}_2 = \frac{1}{n}(\mathbf{L}_F \otimes \mathbf{I}_3)\left(\dot{\mathbf{v}}_d - \lambda_{p,2}(\mathbf{p} - \mathbf{p}_d) - \lambda_{d,2}(\mathbf{v} - \mathbf{v}_d)\right), \tag{8.4}$$

where

$$\mathbf{p}_{d,i} = \mathbf{p}_p + \mathbf{R}_p(\hat{\xi})\mathbf{p}_{f,i}^f, \quad \mathbf{v}_{d,i} = \mathbf{v}_p + \dot{\mathbf{R}}_p(\hat{\xi})\mathbf{p}_{f,i}^f, \quad \dot{\mathbf{v}}_{d,i} = \dot{\mathbf{v}}_p + \ddot{\mathbf{R}}_p(\hat{\xi})\mathbf{p}_{f,i}^f. \tag{8.5}$$

For complete graphs, the following holds for the terms representing the desired formation acceleration:

$$\frac{1}{n}(\mathbf{L}_{F,i} \otimes \mathbf{I}_3)\dot{\mathbf{v}}_d = \ddot{\mathbf{R}}_p \left(\frac{n-1}{n}\mathbf{p}_{f,i}^f - \frac{1}{n}\sum_{j \in \mathcal{N}_i} \mathbf{p}_{f,j}^f \right) = \ddot{\mathbf{R}}_p \mathbf{p}_{f,i}^f \coloneqq \dot{\tilde{\mathbf{v}}}_{d,i}, \tag{8.6}$$

where $\mathbf{L}_{F,i}$ denotes the i-th row of $\mathbf{L}_F$. Thus, we can simplify (8.4) to the following form:

$$\dot{\mathbf{v}}_2 = \dot{\tilde{\mathbf{v}}}_d - \frac{1}{n}(\mathbf{L}_F \otimes \mathbf{I}_3)\left(\lambda_{p,2}(\mathbf{p} - \mathbf{p}_d) + \lambda_{d,2}(\mathbf{v} - \mathbf{v}_d)\right). \tag{8.7}$$

For non-complete graphs, we let the normalized Laplacian be given by

$$\hat{\mathbf{L}} \coloneqq \operatorname{diag}\left(\frac{1}{|\mathcal{N}_1| + 1}, \ldots, \frac{1}{|\mathcal{N}_n| + 1} \right) \mathbf{L}, \tag{8.8}$$

and rewrite (8.7):

$$\dot{\mathbf{v}}_2 = \dot{\tilde{\mathbf{v}}}_d - (\hat{\mathbf{L}} \otimes \mathbf{I}_3)\left(\lambda_{p,2}(\mathbf{p} - \mathbf{p}_d) + \lambda_{d,2}(\mathbf{v} - \mathbf{v}_d)\right), \tag{8.9}$$

The rewritten SOCLIK equation (8.9) can be recognized as a consensus algorithm similar to the general form (1.2), and is equivalently written

$$\begin{aligned}\dot{\mathbf{v}}_{2,i} =& \dot{\tilde{\mathbf{v}}}_d - \lambda_{p,2}\frac{1}{|\mathcal{N}_i|+1}\sum_{j\in\mathcal{N}_i}(\mathbf{p}_i - \mathbf{p}_j - \mathbf{p}_{d,i} + \mathbf{p}_{d,j}) \\ & - \lambda_{d,2}\frac{1}{|\mathcal{N}_i|+1}\sum_{j\in\mathcal{N}_i}(\mathbf{v}_i - \mathbf{v}_j - \mathbf{v}_{d,i} + \mathbf{v}_{d,j}).\end{aligned} \tag{8.10}$$

The null-space projector of the task in terms of the graph Laplacian is given by:

$$\mathbf{N}_2 = \mathbf{I}_{3n} - \hat{\mathbf{L}} \otimes \mathbf{I}_3. \tag{8.11}$$

Multiplying with this matrix is equivalent to taking the mean LOS accelerations of an AUV and its neighbors. It only projects into the null space of the local formation-keeping task consisting of a vehicle and its neighbors, and some formation errors may result from the path-following task in spite of the null-space projection. Due to the nature of the LOS task, this error is bounded. It can therefore be eliminated by introducing a sliding-mode-like switching term to the formation-keeping acceleration (8.9):

$$\begin{aligned}\dot{\mathbf{v}}_2 =& \dot{\tilde{\mathbf{v}}}_d - (\hat{\mathbf{L}} \otimes \mathbf{I}_3)\left(\lambda_{p,2}(\mathbf{p} - \mathbf{p}_d) + \lambda_{d,2}(\mathbf{v} - \mathbf{v}_d)\right) \\ & - \gamma \text{sign}\left((\hat{\mathbf{L}} \otimes \mathbf{I}_3)(\lambda_{p,2}(\mathbf{p} - \mathbf{p}_d) + \lambda_{d,2}(\mathbf{v} - \mathbf{v}_d))\right).\end{aligned} \tag{8.12}$$

Furthermore, we add the saturation term from the centralized version of the controller following the same arguments as in the centralized case:

$$\begin{aligned}\dot{\mathbf{v}}_2 =& \dot{\tilde{\mathbf{v}}}_d - v_{2,\max}\text{sat}(\lambda_{p,2}(\hat{\mathbf{L}} \otimes \mathbf{I}_3)(\mathbf{p} - \mathbf{p}_d)) - \lambda_{d,2}(\hat{\mathbf{L}} \otimes \mathbf{I}_3)(\mathbf{v} - \mathbf{v}_d) \\ & - \gamma \text{sign}\left(v_{2,\max}\text{sat}(\lambda_{p,2}(\hat{\mathbf{L}} \otimes \mathbf{I}_3)(\mathbf{p} - \mathbf{p}_d)) + \lambda_{d,2}(\hat{\mathbf{L}} \otimes \mathbf{I}_3)(\mathbf{v} - \mathbf{v}_d)\right).\end{aligned} \tag{8.13}$$

8.3 Path-following task

In the distributed path-following approach, each vehicle utilizes the LOS law with ocean-current observer (6.34) derived for the centralized algorithm. We apply a constant look ahead distance $\Delta = \Delta_0$ for simplicity. In the LOS-law, we shall replace $\mathbf{p}_b^p$ with

$$\tilde{\mathbf{p}}_i^p = \mathbf{R}_p^{\mathrm{T}}(\xi_i)(\mathbf{p}_i - \mathbf{p}_p(\xi_i)) - \mathbf{p}_{f,i}^f. \tag{8.14}$$

With this choice, $\tilde{\mathbf{p}}_i^p = \mathbf{p}_b^p$ when the fleet has reached the desired formation.

The desired LOS velocity is then given by

$$\mathbf{v}_{LOS,d,i} = \mathbf{R}_p[\Delta,\ -y_{b,i}^p, -z_{b,i}^p]^{\mathrm{T}} \frac{U_{LOS}}{D_i}, \tag{8.15}$$

and the commanded acceleration is given by

$$\dot{\mathbf{v}}_{3,i} = \dot{\mathbf{v}}_{LOS,d,i} + \mathbf{\Lambda}_{LOS}\left(\mathbf{v}_{LOS,d,i} - \tilde{\mathbf{v}}_i^p - \hat{\mathbf{v}}_{c,i}\right). \tag{8.16}$$

The path-progress parameters ξ_i for each vehicle are synchronized using the following consensus law from Matouš, Pettersen, Varagnolo and Paliotta (2023a):

$$\dot{\xi}_i = U_{LOS}\left\|\frac{\partial \mathbf{p}_p(\xi_i)}{\partial \xi}\right\|^{-1}\left(\frac{\Delta}{D_i} + k_\xi \frac{\tilde{x}_i^p}{\sqrt{1+(\tilde{x}_i^p)^2}}\right) + c_\xi \sum_{j\in N_i}(\xi_j - \xi_i). \tag{8.17}$$

The consensus law ensures that the along-path progress remains synchronized for all vehicles.

In simulations, we experienced better results using the following sliding-mode controller to make the path-following velocity converge to $\mathbf{v}_{LOS}$ compared to analytically differentiating $\mathbf{v}_{LOS}$ like in (8.16):

$$\dot{\mathbf{v}}_{3,i} = \mathbf{\Lambda}_{LOS}(\mathbf{v}_{LOS,d,i} - \mathbf{v}_i - \dot{\mathbf{R}}_p \mathbf{p}_{f,i}^f) - \gamma_3 \mathrm{sign}(\mathbf{v}_{LOS,d,i} - \mathbf{v}_i - \dot{\mathbf{R}}_p \mathbf{p}_{f,i}^f). \tag{8.18}$$

The rationale behind this choice is that when the formation task is at steady state, the

total velocity can be decomposed into formation-keeping and path-following velocity:

$$\mathbf{v}_i = \mathbf{v}_{f,i} + \mathbf{v}_{p,i} = \dot{\mathbf{R}}_p \mathbf{p}^f_{f,i} + \mathbf{v}_{p,i}. \tag{8.19}$$

Using this equation we calculate the desired steady-state path-following velocity $\mathbf{v}_{p,i}$ which we insert in (8.18). When the path-following velocity converges to $\mathbf{v}_{LOS,d}$ for all vehicles, the fleet should eventually approach the desired path.

8.4 Alternative distributed NSB

In this section, we present a different approach to making the second-order NSB method distributed. Unlike our previously presented novel approach, this alternative method utilizes consensus laws to update estimates of the barycenter position and velocity, rather than employing a direct consensus control law. The approach follows directly by extending the first-order solution from Matouš, Pettersen, Varagnolo and Paliotta (2023a) to work with our second-order NSB algorithm. While we only consider formation-keeping and path-following tasks, it is worth noting that the collision avoidance task can also be adapted in a similar manner as described in Matouš, Pettersen, Varagnolo and Paliotta (2023a). This section first presents the most important details of the first-order method and then shows how we extend it to work in the second-order context.

In the first-order method, only an estimate for the barycenter position is needed, and its consensus-based update law is given by

$$\dot{\mathbf{p}}_{b,i} = \mathbf{v}_{LOS,i} + k_b(\mathbf{p}_i - \mathbf{R}_p \mathbf{p}^f_{f,i} - \mathbf{p}_{b,i}) + c_b \sum_{j \in \mathcal{N}_i} (\mathbf{p}_{b,j} - \mathbf{p}_{b,i}). \tag{8.20}$$

For the path-following task, this estimate is inserted directly into the line-of-sight velocity equation (6.20) to obtain $\mathbf{v}_{LOS,i}$. The formation-keeping velocity is chosen as

$$\mathbf{v}_{2,i} = \dot{\widehat{\boldsymbol{\sigma}}}_{2,i,d} - \boldsymbol{\Lambda}_2(\widehat{\boldsymbol{\sigma}}_{2,i} - \widehat{\boldsymbol{\sigma}}_{2,i,d}), \tag{8.21}$$

where

$$\widehat{\boldsymbol{\sigma}}_{2,i} = \mathbf{p}_i - \mathbf{p}_{b,i}, \quad \widehat{\boldsymbol{\sigma}}_{2,i,d} = \mathbf{R}_p \mathbf{p}^f_{f,i}. \tag{8.22}$$

The output of the controller is the total desired velocity of the vehicle, which is forwarded to the low-level control

$$\mathbf{v}_i = \mathbf{v}_{LOS,i} + \mathbf{v}_{2,i}. \tag{8.23}$$

We modify this approach to work with the second-order method by extending the estimator for the barycenter position to also estimate the barycenter velocity. The update law is given by

$$\begin{aligned}\dot{\mathbf{p}}_{b,i} = \mathbf{v}_{b,i} &+ k_{b,11}(\mathbf{p}_i - \mathbf{R}_p \mathbf{p}^f_{f,i} - \mathbf{p}_{b,i}) + k_{b,12}(\mathbf{v}_i - \dot{\mathbf{R}}_p \mathbf{p}^f_{f,i} - \mathbf{v}_{b,i}) \\ &c_{b,11} \sum_{j \in \mathcal{N}_i} (\mathbf{p}_{b,j} - \mathbf{p}_{b,i}) + c_{b,12} \sum_{j \in \mathcal{N}_i} (\mathbf{v}_{b,j} - \mathbf{v}_{b,i}),\end{aligned} \tag{8.24}$$

$$\begin{aligned}\dot{\mathbf{v}}_{b,i} = \dot{\mathbf{v}}_{LOS,i} &+ k_{b,21}(\mathbf{p}_i - \mathbf{R}_p \mathbf{p}^f_{f,i} - \mathbf{p}_{b,i}) + k_{b,22}(\mathbf{v}_i - \dot{\mathbf{R}}_p \mathbf{p}^f_{f,i} - \mathbf{v}_{b,i}) \\ &c_{b,21} \sum_{j \in \mathcal{N}_i} (\mathbf{p}_{b,j} - \mathbf{p}_{b,i}) + c_{b,22} \sum_{j \in \mathcal{N}_i} (\mathbf{v}_{b,j} - \mathbf{v}_{b,i}),\end{aligned} \tag{8.25}$$

where $k_{b,ij}$ and $c_{b,ij}$ are positive gains. The intuition for the update law is that $\mathbf{p}_i - \mathbf{R}_p \mathbf{p}^f_{f,i}$ and $\mathbf{v}_i - \dot{\mathbf{R}}_p \mathbf{p}^f_{f,i}$ serve as estimates of the barycenter position and velocity for each individual vehicle. This concept aligns with the idea presented in the barycenter estimate from our novel approach (8.14). Thus, the terms associated with controller gain $k_{b,ij}$ serve as feedback from the vehicle's position and velocity. On the other hand, the terms with gain cb, ij act as consensus terms, ensuring that all vehicles eventually converge to the same estimate of the barycenter.

Given the barycenter estimates, the formation-keeping acceleration is given by

$$\dot{\mathbf{v}}_{2,i} = \ddot{\widehat{\boldsymbol{\sigma}}}_{2,i,d} - \boldsymbol{\Lambda}_{d,2}(\dot{\widehat{\boldsymbol{\sigma}}}_{2,i} - \dot{\widehat{\boldsymbol{\sigma}}}_{2,i,d}) - v_{2,\max} \mathrm{sat}(\boldsymbol{\Lambda}_{p,2}(\widehat{\boldsymbol{\sigma}}_{2,i} - \widehat{\boldsymbol{\sigma}}_{2,i,d})). \tag{8.26}$$

The path-following acceleration is given by directly inserting the barycenter position

and velocity estimates $\mathbf{p}_{b,i}$ and $\mathbf{v}_{b,i}$ into the equations of the centralized method (6.20), (6.22), and (6.23). The path-parameter update law is given by (8.17).

Similarly to the centralized method, the final commanded acceleration is the sum of the path-following and formation-keeping accelerations

$$\boldsymbol{\mu}_i = \dot{\mathbf{v}}_{2,i} + \dot{\mathbf{v}}_{LOS,i}, \tag{8.27}$$

which concludes the definition of the controller.

Chapter 9

Closed-Loop Analysis of the Distributed NSB Method

This chapter studies the stability properties of the novel distributed NSB control law. We show that the formation-keeping task and path-following tasks are asymptotically stable. We do not consider the alternative distributed formulation from Section 8.4, as it is very similar to the method presented in Matouš, Pettersen, Varagnolo and Paliotta (2023a), and the stability analysis should follow directly from combining their results with our results from the centralized method in Chapter 7.

We consider nominal operation in which no collision avoidance task is active. The control input is given by

$$\boldsymbol{\mu}_i = \boldsymbol{\mu}_{f,i} + \boldsymbol{\mu}_{p,i}, \tag{9.1}$$

where $\boldsymbol{\mu}_{f,i}$ and $\boldsymbol{\mu}_{p,i}$ are defined by:

$$\boldsymbol{\mu}_{f,i} \coloneqq \dot{\mathbf{v}}_{2,i}, \quad \boldsymbol{\mu}_{p,i} \coloneqq \frac{1}{|\mathcal{N}_i| + 1} \left(\dot{\mathbf{v}}_{3,i} + \sum_{j \in \mathcal{N}_i} \dot{\mathbf{v}}_{3,j} \right). \tag{9.2}$$

We note that by the definition of the LOS path-following task, $\|\boldsymbol{\mu}_{p,i}\|$ is bounded and we denote the upper bound by $\bar{\mu}_p$.

9.1 Formation-keeping task

In this section, we analyze the stability of the formation-keeping task. Following ideas from Restrepo et al. (2022) we analyze the stability of the edges in the communication graph. The fleet has achieved the desired formation if and only if the edge errors are zero. We simplify the analysis by considering a piecewise linear saturation function instead of the tanh-based function (6.18):

$$\text{sat}(\mathbf{x}) = \begin{cases} \mathbf{x}, & \|\mathbf{x}\| < 1, \\ \frac{\mathbf{x}}{\|\mathbf{x}\|}, & \|\mathbf{x}\| \geq 1. \end{cases} \tag{9.3}$$

We also replace the discontinuous $\text{sign}(x)$ function in (8.13) by element-wise applying $\text{sat}(\frac{x}{\varepsilon})$ as is a common practice to reduce chattering (Khalil; 2002).

The formation-keeping acceleration is then given by

$$\begin{aligned} \dot{\mathbf{v}}_2 =& \dot{\tilde{\mathbf{v}}}_d - v_{2,\max}\text{sat}(\lambda_{p,2}(\hat{\mathbf{L}} \otimes \mathbf{I}_3)(\mathbf{p} - \mathbf{p}_d)) - \lambda_{d,2}(\hat{\mathbf{L}} \otimes \mathbf{I}_3)(\mathbf{v} - \mathbf{v}_d) \\ & - \gamma \text{sat}\left(\frac{1}{\varepsilon}(v_{2,\max}\text{sat}(\lambda_{p,2}(\hat{\mathbf{L}} \otimes \mathbf{I}_3)(\mathbf{p} - \mathbf{p}_d)) + \lambda_{d,2}(\hat{\mathbf{L}} \otimes \mathbf{I}_3)(\mathbf{v} - \mathbf{v}_d))\right). \end{aligned} \tag{9.4}$$

Although the same saturation function is used to approximate two different functions, we note that $\frac{1}{\varepsilon} \gg \lambda_{p,2}$. In the first use case, the function is used to saturate the control effort at high errors, whereas, in the second use case, the saturation function approximates the $\text{sign}(x)$ function and approaches it in the limit $\varepsilon \to 0$.

9.1.1 Closed-loop dynamics

For this analysis, we introduce the incidence matrix $\mathbf{E} \in \mathbb{R}^{n \times m}$ of the communication graph $\mathcal{G}$, where n and m represent the number of nodes and edges in the graph, respectively. The elements of $\mathbf{E}$ are defined as follows:

$$\mathbf{E}_{ij} = \begin{cases} -1, & \text{if node } i \text{ is the terminal node of edge } e_j, \\ 1, & \text{if node } i \text{ is the initial node of edge } e_j, \\ 0, & \text{otherwise.} \end{cases} \tag{9.5}$$

The edge states of the communication graph are then given by

$$\mathbf{z}_1 = (\mathbf{E}^\mathrm{T} \otimes \mathbf{I}_3)\mathbf{p}, \tag{9.6a}$$

$$\mathbf{z}_2 = (\mathbf{E}^\mathrm{T} \otimes \mathbf{I}_3)\mathbf{v}, \tag{9.6b}$$

furthermore, the graph Laplacian is given by

$$\mathbf{L} = \mathbf{E}\mathbf{E}^\mathrm{T}. \tag{9.7}$$

In line with the insights from Restrepo et al. (2022), our goal is to derive a reduced system that is easier to analyze with Lyapunov theory. Building upon the findings of Zelazo et al. (2007), it is possible to reorganize the edge labels, resulting in an expression of the incidence matrix as

$$\mathbf{E} = [\mathbf{E}_t \ \mathbf{E}_c], \tag{9.8}$$

where $\mathbf{E}_t \in \mathbb{R}^{n\times n-1}$ denotes the full-column-rank incidence matrix corresponding to a spanning tree $\mathcal{G}_t \subseteq \mathcal{G}$ and $\mathbf{E}_c \in \mathbb{R}^{n\times(m-n+1)}$ represent the incidence matrix of the remaining edges. Furthermore, an alternative representation of the full incidence matrix is given by

$$\mathbf{E} = \mathbf{E}_t\mathbf{R}, \tag{9.9}$$

$$\mathbf{R} \coloneqq [\mathbf{I}_{n-1} \ \mathbf{T}], \quad \mathbf{T} \coloneqq (\mathbf{E_t}^\mathrm{T}\mathbf{E}_t)^{-1}\mathbf{E}_t^\mathrm{T}\mathbf{E}_c. \tag{9.10}$$

Consequently, the Laplacian of the full communication graph can be written as

$$\mathbf{L} = \mathbf{E}_t\mathbf{R}\mathbf{R}^\mathrm{T}\mathbf{E}_t^\mathrm{T}. \tag{9.11}$$

We let the reduced system error states be given by the edges of an arbitrary

spanning tree of $\mathcal{G}$:

$$\tilde{\mathbf{z}}_{t,1} = (\mathbf{E}_t^{\mathrm{T}} \otimes \mathbf{I}_3)(\mathbf{p} - \mathbf{p}_d), \tag{9.12a}$$

$$\tilde{\mathbf{z}}_{t,2} = (\mathbf{E}_t^{\mathrm{T}} \otimes \mathbf{I}_3)(\mathbf{v} - \mathbf{v}_d), \tag{9.12b}$$

where $\mathbf{p}_d$ and $\mathbf{v}_d$ are given by (8.5). We rewrite the formation acceleration (8.13) in terms of the error states:

$$\begin{aligned}\boldsymbol{\mu}_f =& \dot{\tilde{\mathbf{v}}}_d - v_{2,\max}\mathrm{sat}\left(\lambda_{p,2}(\mathbf{D}\mathbf{E}_t\mathbf{R}\mathbf{R}^{\mathrm{T}} \otimes \mathbf{I}_3)\tilde{\mathbf{z}}_1\right) - \lambda_{d,2}(\mathbf{D}\mathbf{E}_t\mathbf{R}\mathbf{R}^{\mathrm{T}} \otimes \mathbf{I}_3)\tilde{\mathbf{z}}_2 \\ &- \gamma\mathrm{sat}\left(\frac{1}{\varepsilon}(v_{2,\max}\mathrm{sat}\left(\lambda_{p,2}(\mathbf{D}\mathbf{E}_t\mathbf{R}\mathbf{R}^{\mathrm{T}} \otimes \mathbf{I}_3)\tilde{\mathbf{z}}_1\right) + \lambda_{d,2}(\mathbf{D}\mathbf{E}_t\mathbf{R}\mathbf{R}^{\mathrm{T}} \otimes \mathbf{I}_3)\tilde{\mathbf{z}}_2)\right),\end{aligned} \tag{9.13}$$

where $\mathbf{D}$ is the scaling matrix

$$\mathbf{D} \coloneqq \mathrm{diag}\left(\frac{1}{|\mathcal{N}_1|+1}, \ldots, \frac{1}{|\mathcal{N}_n|+1}\right). \tag{9.14}$$

The error-system dynamics are given by

$$\dot{\tilde{\mathbf{z}}}_{t,1} = \tilde{\mathbf{z}}_{t,2}, \tag{9.15a}$$

$$\dot{\tilde{\mathbf{z}}}_{t,2} = (\mathbf{E}_t \otimes \mathbf{I}_3)^{\mathrm{T}}(\boldsymbol{\mu}_f + \boldsymbol{\mu}_p - \dot{\tilde{\mathbf{v}}}_d). \tag{9.15b}$$

9.1.2 Closed-loop stability

We analyze the system using techniques from sliding-mode control. Parts of the proof closely follow insights from the proof of (Khalil; 2002, Theorem 14.1).

Let the sliding surface $\mathbf{s}$ be given by

$$\mathbf{s} = \lambda_{d,2}\tilde{\mathbf{z}}_{t,2} + v_{2,\max}\begin{cases}\lambda_{p,2}\tilde{\mathbf{z}}_{t,1}, & \|\lambda_{p,2}(\mathbf{D}\mathbf{E}_t\mathbf{R}\mathbf{R}^{\mathrm{T}} \otimes \mathbf{I}_3)\mathbf{z}_{t,1}\| < 1, \\ \frac{\tilde{\mathbf{z}}_{t,1}}{\|(\mathbf{D}\mathbf{E}_t\mathbf{R}\mathbf{R}^{\mathrm{T}} \otimes \mathbf{I}_3)\tilde{\mathbf{z}}_{t,1}\|}, & \text{otherwise.}\end{cases} \tag{9.16}$$

On the sliding surface, the dynamics of the error subsystem (9.15a) are given by

$$\dot{\tilde{\mathbf{z}}}_{t,1} = -\frac{v_{2,\max}}{\lambda_{d,2}} \begin{cases} \lambda_{p,2}\tilde{\mathbf{z}}_{t,1}, & \|\lambda_{p,2}(\mathbf{DE_tRR}^{\mathrm{T}} \otimes \mathbf{I}_3)\mathbf{z}_{t,1}\| < 1, \\ \frac{\tilde{\mathbf{z}}_{t,1}}{\|(\mathbf{DE_tRR}^{\mathrm{T}} \otimes \mathbf{I}_3)\tilde{\mathbf{z}}_{t,1}\|}, & \text{otherwise}, \end{cases} \tag{9.17}$$

which is USGES. When $\tilde{\mathbf{z}}_{t,1}$ is inside the ball $\mathcal{B}_1 := \{\tilde{\mathbf{z}}_{t,1} : \|\tilde{\mathbf{z}}_{t,1}\| < \frac{1}{\lambda_{p,2}\sigma_{\max}^2}\}$, where $\sigma_{\max}$ is the largest singular value of $(\mathbf{DE_tRR}^{\mathrm{T}} \otimes \mathbf{I}_3)$, the system is exponentially stable due to the negative linear feedback. Outside the ball $\mathcal{B}_1$, the system is asymptotically stable which we show with the Lyapunov candidate function

$$V_z(\tilde{\mathbf{z}}_{t,1}) = \frac{1}{2}\tilde{\mathbf{z}}_{t,1}^{\mathrm{T}}\tilde{\mathbf{z}}_{t,1}. \tag{9.18}$$

The time derivative of V_z along the trajectories of (9.17) when the system is outside the linear region is bounded by

$$\dot{V}_z \leq -\frac{v_{2,max}}{\lambda_{d,2}\sigma_{max}^2}\|\tilde{\mathbf{z}}_{t,1}\|, \tag{9.19}$$

which results in asymptotic stability. Furthermore, it holds for any $\tilde{\mathbf{z}}_{t,1} \in \{\tilde{\mathbf{z}}_{t,1} \in \mathbb{R}^{3n-3} : \|\tilde{\mathbf{z}}_{t,1}\| \leq r\}$ that

$$\dot{V}_z \leq -\frac{v_{2,max}}{\lambda_{d,2}\sigma_{max}^2 r}\|\tilde{\mathbf{z}}_{t,1}\|^2. \tag{9.20}$$

Thus, all requirements for (Pettersen; 2017, Theorem 5) are satisfied, and the system is USGES. Moreover, as a result, when $\mathbf{s}$ is non-zero it can be shown that

$$\dot{V}_z \leq -\alpha_3(\|\tilde{\mathbf{z}}_{t,1}\|), \quad \forall\|\tilde{\mathbf{z}}_{t,1}\| \geq \frac{\lambda_{d,2}}{v_{2,\max}\lambda_{p,2}}\|\mathbf{s}\|, \ \|\mathbf{s}\| \leq \frac{v_{2,\max}}{\sigma_{\max}^2}, \tag{9.21}$$

for some $\mathcal{K}_\infty$ class function α_3 which implies local input-to-state stability of the system when $\mathbf{s}$ is viewed as the input.

The control input $\boldsymbol{\mu}_f$ can be written in terms of the sliding variable as follows

$$\boldsymbol{\mu}_f = \dot{\tilde{v}}_d - (\mathbf{DE_tRR}^{\mathrm{T}} \otimes \mathbf{I}_3)\mathbf{s} - \gamma \mathrm{sat}\left(\frac{1}{\varepsilon}(\mathbf{DE_tRR}^{\mathrm{T}} \otimes \mathbf{I}_3)\mathbf{s}\right). \tag{9.22}$$

The time derivative of the sliding variable along the trajectories of (9.15) is given by

$$\begin{aligned}\dot{\mathbf{s}} = &-\lambda_{d,2}\Bigg((\mathbf{E}_\mathbf{t}^\mathrm{T}\mathbf{D}\mathbf{E}_\mathbf{t}\mathbf{R}\mathbf{R}^\mathrm{T}\otimes\mathbf{I}_3)\mathbf{s} + \mathbf{E}_t^\mathrm{T}\gamma\mathrm{sat}\left(\frac{1}{\varepsilon}(\mathbf{D}\mathbf{E}_\mathbf{t}\mathbf{R}\mathbf{R}^\mathrm{T}\otimes\mathbf{I}_3)\mathbf{s}\right)\\ &-(\mathbf{E}_t^\mathrm{T}\otimes\mathbf{I}_3)\boldsymbol{\mu}_p\Bigg) + v_{2,\max}\begin{cases}\lambda_{p,2}\tilde{\mathbf{z}}_2, & \|\lambda_{p,2}(\mathbf{D}\mathbf{E}_\mathbf{t}\mathbf{R}\mathbf{R}^\mathrm{T}\otimes\mathbf{I}_3)\tilde{\mathbf{z}}_{t,1}\| < 1,\\ 0, & \text{otherwise.}\end{cases}\end{aligned} \tag{9.23}$$

Consider the following Lyapunov function

$$V_s(\mathbf{s}) = \frac{1}{2}\mathbf{s}^\mathrm{T}(\mathbf{R}\mathbf{R}^\mathrm{T}\otimes\mathbf{I}_3)\mathbf{s}. \tag{9.24}$$

The matrix $\mathbf{R}\mathbf{R}^\mathrm{T}$ evaluates to the following:

$$\mathbf{R}\mathbf{R}^\mathrm{T} = \mathbf{I}_{n-1} + \left((\mathbf{E}_\mathbf{t}{}^\mathrm{T}\mathbf{E}_t)^{-1}\mathbf{E}_t^\mathrm{T}\mathbf{E}_c\right)\left((\mathbf{E}_\mathbf{t}{}^\mathrm{T}\mathbf{E}_t)^{-1}\mathbf{E}_t^\mathrm{T}\mathbf{E}_c\right)^\mathrm{T}. \tag{9.25}$$

The product of a matrix with its transpose is always at least positive semi-definite, and the sum of a positive definite matrix and a positive semi-definite matrix is positive definite. Therefore $\mathbf{R}\mathbf{R}^\mathrm{T}$ is positive definite and V is a valid Lyapunov function.

The time derivative of V is given by

$$\begin{aligned}\dot{V}_s = &-\lambda_{d,2}\mathbf{s}^\mathrm{T}(\mathbf{R}\mathbf{R}^\mathrm{T}\mathbf{E}_\mathbf{t}^\mathrm{T}\mathbf{D}\mathbf{E}_\mathbf{t}\mathbf{R}\mathbf{R}^\mathrm{T}\otimes\mathbf{I}_3)\mathbf{s}\\ &-\lambda_{d,2}\mathbf{s}^\mathrm{T}(\mathbf{R}\mathbf{R}^\mathrm{T}\mathbf{E}_t^\mathrm{T}\otimes\mathbf{I}_3)\gamma\mathrm{sat}\left(\frac{1}{\varepsilon}(\mathbf{D}\mathbf{E}_\mathbf{t}\mathbf{R}\mathbf{R}^\mathrm{T}\otimes\mathbf{I}_3)\mathbf{s}\right)\\ &+\mathbf{s}^\mathrm{T}(\mathbf{R}\mathbf{R}^\mathrm{T}\mathbf{E}_t^\mathrm{T}\otimes\mathbf{I}_3)\Bigg(\lambda_{d,2}\boldsymbol{\mu}_p\\ &+v_{2,\max}\begin{cases}\lambda_{p,2}(\mathbf{v}-\mathbf{v}_d), & \|\lambda_{p,2}(\mathbf{D}\mathbf{E}_\mathbf{t}\mathbf{R}\mathbf{R}^\mathrm{T}\otimes\mathbf{I}_3)\tilde{\mathbf{z}}_{t,1}\| < 1,\\ 0, & \text{otherwise}\end{cases}\Bigg).\end{aligned} \tag{9.26}$$

From (Zelazo et al.; 2007, Theorem 3.3), the null-space of $\mathbf{E}_t$ is empty, and the null-space of $\mathbf{R}\mathbf{R}^\mathrm{T}$ is empty because it is a positive definite matrix. Then, $\mathbf{R}\mathbf{R}^\mathrm{T}\mathbf{E}_t^\mathrm{T}\mathbf{D}\mathbf{E}_t\mathbf{R}\mathbf{R}^\mathrm{T}$ is positive

definite:

$$\mathbf{x}^{\mathrm{T}}\mathbf{R}\mathbf{R}^{\mathrm{T}}\mathbf{E}_t^{\mathrm{T}}\mathbf{D}\mathbf{E}_t\mathbf{R}\mathbf{R}^{\mathrm{T}}\mathbf{x} = \|\mathbf{D}^{1/2}\mathbf{E}_t\mathbf{R}\mathbf{R}^{\mathrm{T}}\mathbf{x}\|_2^2 > 0, \quad \forall \mathbf{x} \neq \mathbf{0}. \tag{9.27}$$

We now introduce the following change of variables

$$\hat{\mathbf{s}} \coloneqq (\mathbf{E}_t\mathbf{R}\mathbf{R}^{\mathrm{T}} \otimes \mathbf{I}_3)\mathbf{s}, \tag{9.28}$$

and note the following bound

$$\boldsymbol{\mu}_{p,i} + \frac{v_{2,\max}\lambda_{p,2}}{\lambda_{d,2}}(\mathbf{v}_i - \mathbf{v}_{d,i}) \leq \bar{\mu}_p + \frac{v_{2,\max}\lambda_{p,2}}{\lambda_{d,2}}|\mathbf{v}_i - \mathbf{v}_{d,i}| \coloneqq \rho(\mathbf{v}_i). \tag{9.29}$$

We let γ be a function of the velocity so that $\gamma_i = \rho(\mathbf{v}_i) + \beta_0$ for some constant $\beta_0 > 0$. Now, (9.26) can be bounded by

$$\dot{V}_s \leq \lambda_{d,2} \sum_{i=1}^{3n} -\gamma_i \hat{\mathbf{s}}_i \mathrm{sat}(\frac{\sqrt{\mathbf{D}_{ii}}}{\varepsilon}\hat{\mathbf{s}}_i) + |\hat{\mathbf{s}}_i|\rho(\mathbf{v}_i). \tag{9.30}$$

Consider every element of the sum separately. In the region $|\hat{\mathbf{s}}_i| \geq \frac{\varepsilon}{\sqrt{\mathbf{D}_{ii}}}$, we have

$$\dot{V}_{s,i} \leq \lambda_{d,2}(-\gamma_i + \rho(\mathbf{v}_i))|\hat{\mathbf{s}}_i| \leq -\lambda_{d,2}\beta_0|\hat{\mathbf{s}}_i|. \tag{9.31}$$

This bound shows that whenever $|\hat{\mathbf{s}}_i(0)| > \frac{\varepsilon}{\sqrt{\mathbf{D}_{ii}}}$, $|\hat{\mathbf{s}}_i(t)|$ will decrease until it reaches the set $\{\hat{\mathbf{s}}_i \colon |\hat{\mathbf{s}}_i| \leq \frac{\varepsilon}{\sqrt{\mathbf{D}_{ii}}}\}$ in finite time and remains inside thereafter. We note that in practice, the velocity is upper bounded by the vehicle's maximum operating speed and γ_i can therefore be chosen as a constant.

We will now show that the system is bounded and, in the limit $\varepsilon \to 0$, asymptotically stable. This part of the analysis closely follows (Khalil; 2002, Theorem 14.1). Consider a positive constant c and the following chain of implications

$$|\hat{\mathbf{s}}_i| \leq c \;\forall\; i \in \{1, \ldots, n\} \implies \|\hat{\mathbf{s}}\| \leq k_1 c \implies \|\mathbf{s}\| \leq \frac{k_1 c}{\sigma_{\min}^2}, \tag{9.32}$$

where k_1 is some positive constant and $\sigma_{\min}$ is the smallest singular value of $\mathbf{E_t R R}^{\mathrm{T}}$. Following (9.21), if we choose $c \leq \frac{v_{2,\max}\sigma_{\min}^2}{k_1\sigma_{\max}^2}$, then,

$$\begin{aligned} V_z(\tilde{\mathbf{z}}_{t,1}) \geq \frac{1}{2}\left(\frac{\lambda_{d,2}k_1 c}{v_{2,\max}\lambda_{p,2}\sigma_{\min}^2}\right)^2 &\implies \|\tilde{\mathbf{z}}_{t,1}\| \geq \frac{\lambda_{d,2}k_1 c}{v_{2,\max}\lambda_{p,2}\sigma_{\min}^2} \geq \frac{\lambda_{d,2}\|\mathbf{s}\|}{v_{2,\max}\lambda_{p,2}} \\ &\implies \dot{V}_z \leq -\alpha_3(\|\tilde{\mathbf{z}}_{t,1}\|) \leq -\alpha_3\left(\frac{\lambda_{d,2}k_1 c}{v_{2,\max}\lambda_{p,2}}\right), \end{aligned} \tag{9.33}$$

which shows that the set $\{\tilde{\mathbf{z}}_{t,1} \colon V_z(\tilde{\mathbf{z}}_{t,1}) \leq c_0\}$ with $c_0 \geq \frac{1}{2}\left(\frac{\lambda_{d,2}k_1 c}{v_{2,\max}\lambda_{p,2}\sigma_{\min}^2}\right)^2$ is positively invariant because $\dot{V}$ is negative on the boundary $V_z(\tilde{\mathbf{z}}_{t,1}) = c_0$. Consequently, it follows that the set

$$\Omega = \left\{\tilde{\mathbf{z}}_{t,1} \colon V_z(\tilde{\mathbf{z}}_{t,1}) \leq c_0\right\} \times \{\mathbf{s} \colon |\hat{\mathbf{s}}_i| \leq c \;\forall\; 1 \leq i \leq n\}, \tag{9.34}$$

is positively invariant when $c \geq \frac{\varepsilon}{\sqrt{\mathbf{D}_{ii}}}$. It serves as an estimate of the control law's region of attraction. After some finite time, we have $|\hat{\mathbf{s}}_i| \leq \frac{\varepsilon}{\sqrt{\mathbf{D}_{ii}}}$. It follows from (9.18) and (9.21) that $\dot{V}_z \leq -\alpha_3\left(\frac{\lambda_{d,2}k_1\varepsilon}{v_{2,\max}\lambda_{p,2}\sigma_{\min}^2}\right)$ for all $V_z(\tilde{\mathbf{z}}_{t,1}) \geq \frac{1}{2}\left(\frac{\lambda_{d,2}k_1\varepsilon}{v_{2,\max}\lambda_{p,2}\sigma_{\min}^2}\right)^2$. Therefore, the trajectories will eventually reach the positive invariant set

$$\Omega_\varepsilon = \left\{\tilde{\mathbf{z}}_{t,1} \colon V_z(\tilde{\mathbf{z}}_{t,1}) \leq \frac{1}{2}\left(\frac{\lambda_{d,2}k_1\varepsilon}{v_{2,\max}\lambda_{p,2}\sigma_{\min}^2}\right)^2\right\} \times \left\{\mathbf{s} \colon |\hat{\mathbf{s}}_i| \leq \frac{\epsilon}{\sqrt{\mathbf{D}_{ii}}} \;\forall\; 1 \leq i \leq n\right\}. \tag{9.35}$$

The set Ω_ε can be made arbitrarily small by choosing ε small enough. In the limit, Ω_ε shrinks to the origin and the system is asymptotically stable.

Lemma 9.1. *Let the fleet communication graph $\mathcal{G}$ be connected, and let $\lambda_{p,2}$, $\lambda_{d,2}$, $v_{2,\max}$, β_0, and ε be positive constants and choose γ_i so that*

$$\gamma_i \geq \beta_0 + \bar{\mu}_p + \frac{v_{2,\max}\lambda_{p,2}}{\lambda_{d,2}}|\mathbf{v}_i - \mathbf{v}_{d,i}|. \tag{9.36}$$

Then, for all $\tilde{\mathbf{z}}_t(0) \in \Omega$, defined by (9.34)*, the system* (9.15) *subject to controller* (9.13) *reaches the positively invariant set Ω_ε, defined by* (9.35)*, in finite time. In the limit $\varepsilon \to 0$ the set Ω_ε reduces to the origin and the system is asymptotically stable.*

We further note that the sliding-variable subsystem is globally asymptotically stable because $\dot{V}_{s,i}$ for all i, given by (9.31), is globally negative. Therefore, when the system starts outside of Ω the states $\tilde{\mathbf{z}}_{t,1}$ may initially grow as $\dot{V}_z \geq 0$, but there exists a time $T > 0$ after which $\|\mathbf{s}\| \leq \frac{v_{2,\max}}{\sigma^2_{\max}}$ and thus $\dot{V}_z \leq -\alpha_3(\|\tilde{\mathbf{z}}_{t,1}\|)$. We can therefore conclude that the system is globally ultimately bounded. Furthermore, because the sliding variables are saturated in position, any initial configuration with zero initial velocity will be within the set Ω.

9.2 Path-following task

In this section, we will analyze the stability of the path-following task. Similarly to the analysis of the centralized control law we will use cascaded system theory to analyze the perturbed LOS dynamics. The following analysis largely follows insights from Matouš, Pettersen, Varagnolo and Paliotta (2023a). To simplify analysis we assume that the desired path is a straight line. Consequently, the rotation matrix $\mathbf{R}_p$ is constant and independent of ξ, and the path function is given by

$$\mathbf{p}_p(\xi) = \mathbf{p}_0 + \mathbf{R}_p[\xi,\ 0,\ 0]^{\mathrm{T}}. \tag{9.37}$$

We also assume that there is no ocean current.

9.2.1 Closed-loop dynamics

In this section, we derive the closed-loop equations for the error variables.

In the case of straight-line paths, the path-following task acceleration can be simplified to

$$\dot{\mathbf{v}}_{3,i} = \dot{\mathbf{v}}_{LOS,d,i} + \Lambda_{LOS}(\mathbf{v}_{LOS,d,i} - \mathbf{v}_i), \tag{9.38}$$

where the desired LOS acceleration is given by

$$\begin{aligned}\dot{\mathbf{v}}_{LOS,d} = \mathbf{R}_p \left[0, -\dot{y}_b^p, -\dot{z}_b^p\right]^{\mathrm{T}} \frac{U_{LOS}}{D} \\ - \mathbf{R}_p \left[\Delta, -y_b^p, -z_b^p\right]^{\mathrm{T}} \frac{U_{LOS}}{D^2} \dot{D}.\end{aligned} \tag{9.39}$$

The actually applied acceleration is given by $\boldsymbol{\mu}_{p,i}$ from (9.2), however, because the communication graph is undirected, the following holds

$$\sum_{i=1}^{n} \boldsymbol{\mu}_{p,i} = \sum_{i=1}^{n} \frac{1}{|\mathcal{N}_i| + 1} \left(\dot{\mathbf{v}}_{3,i} + \sum_{j \in \mathcal{N}_i} \dot{\mathbf{v}}_{3,j} \right) = \sum_{i=1}^{n} \dot{\mathbf{v}}_{3,i}. \tag{9.40}$$

The local averaging can therefore be disregarded in the following analysis.

Also following the straight-line simplification, the barycenter kinematics are given by

$$\begin{aligned}\dot{\mathbf{p}}_b^p &= \mathbf{R}_p^{\mathrm{T}} \left(\frac{1}{n} \sum_{i=1}^{n} \mathbf{v}_i - \dot{\mathbf{p}}_p(s) \right), \\ &= \frac{1}{n} \sum_{i=1}^{N} \mathbf{R}_p^{\mathrm{T}} \left(\mathbf{v}_{LOS,d,i} + \widetilde{\mathbf{v}}_i \right) - [\dot{\xi},\ 0,\ 0]^{\mathrm{T}}.\end{aligned} \tag{9.41}$$

The velocity error $\widetilde{\mathbf{v}}_i$ is defined as

$$\widetilde{\mathbf{v}}_i = \mathbf{v}_i - \mathbf{v}_{LOS,d,i}, \tag{9.42}$$

and we analyze the dynamics of the sum $\sum_{i=1}^{n} \widetilde{\mathbf{v}}_i$:

$$\begin{aligned}\sum_{i=1}^{n} \dot{\widetilde{\mathbf{v}}}_i &= \sum_{i=1}^{n} \dot{\mathbf{v}}_{3,i} + \boldsymbol{\mu}_{f,i} - \dot{\mathbf{v}}_{LOS,d,i}, \\ &= - \sum_{i=1}^{n} \Lambda_{LOS} \widetilde{\mathbf{v}}_i.\end{aligned} \tag{9.43}$$

This system is linear and exponentially stable. The consensus-based formation-keeping

accelerations cancel out in the sum due to the undirected communication graph.

Each individual vehicle's estimate of the barycenter is given by

$$\tilde{\mathbf{p}}_i^p = \mathbf{R}_p^{\mathrm{T}}(\mathbf{p}_i - \mathbf{p}_p(\xi_i) - \mathbf{R}_p \mathbf{p}_{f,i}^f). \tag{9.44}$$

The barycenter error is then defined as

$$\widetilde{\mathbf{p}}_{b,i}^p = \tilde{\mathbf{p}}_i^p - \mathbf{p}_b^p. \tag{9.45}$$

The barycenter error is directly dependent on the formation-keeping error $\widetilde{\mathbf{z}}_{t,1}$, which is bounded or asymptotically stable according to Lemma 9.1. To show this, we first define the "true" path-progress parameter ξ as the mean of the individual estimates:

$$\xi := \frac{1}{n}\sum_{i=1}^{n} \xi_i. \tag{9.46}$$

Then, we rewrite the barycenter equation:

$$\begin{aligned}
\mathbf{p}_b^p &= \mathbf{R}_p^{\mathrm{T}}(\frac{1}{n}\sum_{i=0}^{n} \mathbf{p}_i - \mathbf{p}_p), \\
&= \mathbf{R}_p^{T}(\frac{1}{n}\sum_{i=0}^{n} \mathbf{p}_i - \frac{1}{n}\sum_{i=1}^{n}(\mathbf{p}_{p,0} + \mathbf{R}_p[\xi_i, 0, 0]^{\mathrm{T}} + \mathbf{R}_p \mathbf{p}_{f,i}^f)), \\
&= \mathbf{R}_p^{\mathrm{T}}(\frac{1}{n}\mathbf{1}_{n,1}^{\mathrm{T}} \otimes \mathbf{I}_3)(\mathbf{p} - \mathbf{p}_d).
\end{aligned} \tag{9.47}$$

Here, we used the straight-line assumption and the fact that the formation vectors $\mathbf{p}_{f,i}^f$ sum to zero. We furthermore rewrite (9.44) in the simplified form

$$\tilde{\mathbf{p}}_i^p = \mathbf{R}_p^{\mathrm{T}}(\mathbf{p}_i - \mathbf{p}_{d,i}). \tag{9.48}$$

Now, the barycenter error $\widetilde{\mathbf{P}}_b^p := [\widetilde{\mathbf{p}}_{b,1}^p, \ldots, \widetilde{\mathbf{p}}_{b,n}^p]^{\mathrm{T}}$ can be written in the following form

$$\widetilde{\mathbf{P}}_b^p = (\mathbf{I}_n \otimes \mathbf{R}_p^{\mathrm{T}})(\mathbf{I}_n - \frac{1}{n}\mathbf{1}_{n,n} \otimes \mathbf{I}_3)(\mathbf{p} - \mathbf{p}_d), \tag{9.49}$$

where $\mathbf{I}_n - \frac{1}{n}\mathbf{1}_{n,n}$ can be recognized as the scaled Laplacian matrix of a fully connected graph with n nodes. Consequently, following (9.11) and (9.12a), (9.49) can be rewritten in the following way:

$$\begin{aligned}\widetilde{\mathbf{P}}_b^p &= (\mathbf{I}_n \otimes \mathbf{R}_p^{\mathrm{T}})(\frac{1}{n}\mathbf{L}_F \otimes \mathbf{I}_3)(\mathbf{p} - \mathbf{p}_d), \\ &= (\mathbf{I}_n \otimes \mathbf{R}_p^{\mathrm{T}})(\frac{1}{n}\mathbf{E}_t\mathbf{R}\mathbf{R}^{\mathrm{T}}\mathbf{E}_t^{\mathrm{T}} \otimes \mathbf{I}_3)(\mathbf{p} - \mathbf{p}_d), \\ &= (\mathbf{I}_n \otimes \mathbf{R}_p^{\mathrm{T}})(\frac{1}{n}\mathbf{E}_t\mathbf{R}\mathbf{R}^{\mathrm{T}} \otimes \mathbf{I}_3)\tilde{\mathbf{z}}_{t,1}.\end{aligned} \tag{9.50}$$

Thus, the barycenter norm of the barycenter error can be bounded by the following inequality

$$\left\|\widetilde{\mathbf{P}}_b^p\right\| \leq \frac{1}{n}\left\|\mathbf{E}_t\mathbf{R}\mathbf{R}^{\mathrm{T}}\right\| \|\tilde{\mathbf{z}}_{t,1}\|. \tag{9.51}$$

The desired LOS velocity calculated by vehicle i can be expressed as

$$\mathbf{v}_{LOS,d,i} = \mathbf{v}_{LOS,d} + \widetilde{\mathbf{v}}_{LOS,d,i}, \tag{9.52}$$

where

$$\widetilde{\mathbf{v}}_{LOS,d,i} = \mathbf{R}_p[\Delta,\ -\tilde{y}_i^p, -\tilde{z}_i^p]^{\mathrm{T}}\frac{U_{LOS}}{D_i} - \mathbf{R}_p[\Delta,\ -y_b^p, -z_b^p]^{\mathrm{T}}\frac{U_{LOS}}{D}. \tag{9.53}$$

It follows that $\widetilde{\mathbf{v}}_{LOS,d,i} = \mathbf{0}$ if $\widetilde{\mathbf{p}}_{b,i} = \mathbf{0}$. Furthermore, it can be shown that the norm of the LOS velocity error satisfies the following inequality

$$\|\widetilde{\mathbf{v}}_{LOS,d,i}\| \leq \frac{U_{LOS}}{\Delta}\|\widetilde{\mathbf{p}}_{b,i}\|. \tag{9.54}$$

We will now derive the closed-loop expression for the path-parameter error $\tilde{\xi}_i = \xi_i - \xi$. First, a closed-loop expression for $\dot{\xi}$ is given by

$$\dot{\xi} = \frac{1}{n}\sum_{i=1}^{n}\dot{\xi}_i = \frac{1}{n}\sum_{i=1}^{n}U_{LOS}\left(\frac{\Delta}{D_i} + k_\xi\frac{\tilde{x}_i^p}{\sqrt{1+(\tilde{x}_i^p)^2}}\right). \tag{9.55}$$

The consensus terms cancel out because the vehicles communicate over an undirected

graph, and from the definition of a straight-line path in (9.37), it follows that $\|\frac{\partial \mathbf{p}_P(\xi)}{\partial \xi}\| = 1$.

We define the path parameter update errors, $g_1, \ldots, g_N$, as

$$g_i = U_{LOS}\left(\frac{\Delta}{D_i} - \frac{\Delta}{D} + k_\xi\left(\frac{\tilde{x}_i^p}{\sqrt{1+(\tilde{x}_i^p)^2}} - \frac{x_b^p}{\sqrt{1+(x_b^p)^2}}\right)\right). \tag{9.56}$$

It can be shown that g_i satisfies the following inequality

$$|g_i| \leq U_{LOS}\left(\frac{1}{\Delta} + k_\xi\right)\|\widetilde{\mathbf{p}}_{b,i}\| + U_{LOS}k_\xi|\tilde{\xi}_i|. \tag{9.57}$$

Inserting for (9.56) in (9.55) results in

$$\dot{\xi} = U_{LOS}\left(\frac{\Delta}{D} + k_\xi\frac{x_b^p}{\sqrt{1+(x_b^p)^2}}\right) + \frac{1}{n}\sum_{i=1}^{N} g_i. \tag{9.58}$$

The time derivative of $\tilde{\xi}_i$ is given by

$$\dot{\tilde{\xi}}_i = c_\xi \sum_{i\in\mathcal{N}_i}(\tilde{\xi}_j - \tilde{\xi}_i) + g_i - \frac{1}{n}\sum_{j=1}^{n} g_j, \tag{9.59}$$

which can be written in matrix form

$$\dot{\widetilde{\Xi}} = -c_\xi \mathbf{L}\widetilde{\Xi} + \frac{1}{n}\mathbf{L}_F\mathbf{G}, \tag{9.60}$$

where $\widetilde{\Xi} = [\tilde{\xi}_1, \ldots, \tilde{\xi}_n]^{\mathrm{T}}$, $\mathbf{G} = [g_1, \ldots, g_n]^{\mathrm{T}}$.

Finally, substituting (9.52), (9.58), the barycenter dynamics (9.41) can be written as

$$\begin{aligned}\dot{\mathbf{p}}_b^p = &- U_{LOS}\left[k_\xi \frac{x_b^p}{\sqrt{1+(x_b^p)^2}},\ \frac{y_b^p}{D},\ \frac{z_b^p}{D}\right]^{\mathrm{T}} \\ &+ \frac{1}{n}\sum_{i=1}^{n}\left(\mathbf{R}_p^T(\widetilde{\mathbf{v}}_{LOS,d,i}+\widetilde{\mathbf{v}}_i)+g_i\right).\end{aligned} \tag{9.61}$$

9.2.2 Closed-loop stability

In this section, we will analyze the stability of the error variables $\tilde{\xi}_i$, $\widetilde{\mathbf{v}}_i$, and finally $\mathbf{p}_b^p$. Our aim is to show uniform global asymptotic stability. We will therefore use (Loría and Panteley; 2005, Theorem 2.1) to analyze the cascaded systems, which is similar to (Pettersen; 2017, Proposition 9), but provides weaker stability properties under weaker assumptions on the perturbing and perturbed systems. For convenience, we summarize the theorem here.

Consider a cascaded system

$$\dot{\mathbf{x}}_1 = f_1(t,\mathbf{x}_1) + g(t,\mathbf{x})\mathbf{x}_2, \tag{9.62a}$$

$$\dot{\mathbf{x}}_2 = f_2(t,\mathbf{x}_2). \tag{9.62b}$$

The theorem (Loría and Panteley; 2005, Theorem 2.1) states that if the nominal system

$$\dot{\mathbf{x}}_1 = f_1(t,\mathbf{x}_1) \tag{9.63}$$

is UGAS, the trajectories of (9.62b) are uniformly globally bounded, and the following three assumptions below are satisfied, then the solutions of system (9.62) are uniformly globally bounded. Moreover, if the origin of system (9.62b) is UGAS, then so is the origin of the cascade (9.62).

1. There exist constants $c_1, c_2, \eta > 0$ and a Lyapunov function $V(t,\mathbf{x}_1)$ for (9.63) such that $V : \mathbb{R}_{\geq 0} \times \mathbb{R}^n \to \mathbb{R}_{\geq} 0$ is positive definite, radially unbounded, $\dot{V}(t,\mathbf{x}_1) \leq 0$

and

$$\left\| \frac{\partial V}{\partial \mathbf{x}_1} \right\| \|\mathbf{x}_1\| \leq c_1 V, \qquad \forall \|\mathbf{x}_1\| \geq \eta, \tag{9.64a}$$

$$\left\| \frac{\partial V}{\partial \mathbf{x}_1} \right\| \leq c_2, \qquad \forall \|\mathbf{x}_1\| \leq \eta. \tag{9.64b}$$

2. There exist two continuous functions $\theta_1, \theta_2 : \mathbb{R}_{\geq 0} \to \mathbb{R}_{\geq 0}$ such that

$$\|g(t, \mathbf{x})\| \leq \theta_1 (\|\mathbf{x}_2\|) + \theta_2 (\|\mathbf{x}_2\|) \|\mathbf{x}_1\| . \tag{9.65}$$

3. There exists a class $\mathcal{K}$ function $\alpha(\cdot)$ such that, for all $t_0 \geq 0$, the trajectories of the system (9.62b) satisfy

$$\int_{t_0}^{\infty} \|\mathbf{x}_2(t; t_0, \mathbf{x}_2(t_0))\| dt \leq \alpha(\|\mathbf{x}_2(t_0)\|). \tag{9.66}$$

Lemma 9.2. *If the formation-keeping subsystem* (9.15) *satisfies the initial condition and all parameter conditions of Lemma 9.1, and the consensus gain c_ξ is chosen such that $c_\xi \lambda_2 > 2U_{LOS} k_\xi$, where λ_2 is the Fiedler eigenvalue of $\mathbf{L}$, then the solutions of system* (9.60) *are uniformly globally bounded. Furthermore, if $\varepsilon \to 0$ so that the origin of the formation-keeping subsystem* (9.15) *is asymptotically stable, then $\widetilde{\Xi} = 0$ is a UGAS equilibrium of* (9.60).

Proof. We analyze system (9.60) as a cascade where $\widetilde{\mathbf{P}}_b^p$ perturbs the dynamics of $\widetilde{\Xi}$ through $\mathbf{G}$.

Substituting $\widetilde{\mathbf{P}}_b = \mathbf{0}$ into $\mathbf{G}$ we get the following *nominal* dynamics of $\widetilde{\Xi}$

$$\dot{\widetilde{\Xi}} = -c_\xi \mathbf{L} \widetilde{\Xi} + \frac{1}{n} \mathbf{L}_F \mathbf{G}_\xi. \tag{9.67}$$

From (9.57) the following inequality holds true for $\mathbf{G}_\xi$

$$\|\mathbf{G}_\xi\| \leq U_{LOS} k_\xi \|\widetilde{\Xi}\|. \tag{9.68}$$

Consider the following Lyapunov function candidate

$$V_{\tilde{\xi}}(\widetilde{\boldsymbol{\xi}}) = \frac{1}{2}\widetilde{\Xi}^{\mathrm{T}}\widetilde{\Xi}. \tag{9.69}$$

The derivative of $V_{\tilde{\xi}}$ along the trajectories of (9.67) is

$$\dot{V}_{\tilde{\xi}} = -c_{\tilde{\xi}}\tilde{\Xi}^{\mathrm{T}}\mathbf{L}\tilde{\Xi} + \frac{1}{n}\tilde{\Xi}^{\mathrm{T}}\mathbf{L}_F\mathbf{G}_{\tilde{\xi}} \leq \left(-c_{\tilde{\xi}}\lambda_2 + 2U_{LOS}k_{\tilde{\xi}}\right)\|\tilde{\Xi}\|^2. \tag{9.70}$$

We conclude that $\dot{V}_{\tilde{\xi}}$ is negative definite, and the nominal system is GES, if $c_{\tilde{\xi}}\lambda_2 > 2U_{LOS}k_{\tilde{\xi}}$. The barycenter error $\widetilde{\mathbf{P}}_b^p$ is bounded by the formation-keeping error $\tilde{\mathbf{z}}_{t,1}$ which is asymptotically stable following Lemma 9.1 when $\varepsilon \to \infty$.

We now analyze the stability of the cascaded system under the assumption that the formation-keeping system is asymptotically stable. Consider the Lyapunov function candidate $V_{\tilde{\xi}}$. The first assumption in (Loría and Panteley; 2005, Theorem 2.1) is satisfied with $c_1 = \frac{1}{2}$, $\eta > 0$, and $c_2 = \eta$. The second assumption is satisfied with $\theta_1(\widetilde{\mathbf{P}}_b^p) = U_{LOS}(\frac{1}{\Delta} + k_{\tilde{\xi}})\|\widetilde{\mathbf{P}}_b^p\|$ and $\theta_2(\widetilde{\mathbf{P}}_b^p) = 0$.

The third assumption is shown in (Pettersen; 2017, Remark 11) to be satisfied for systems with the properties UGAS + uniformly locally exponentially stable (ULES). Our formation-keeping system is locally and not globally asymptotically stable, but the results hold locally.

Since the system is ULES there exist positive constants c, k, λ independent on t_0, such that $\forall\widetilde{\mathbf{P}}_b^p \in \{\widetilde{\mathbf{P}}_b^p : \tilde{\mathbf{z}}_{t,1} \in \mathcal{B}_1\}$

$$\|\widetilde{\mathbf{P}}_b^p(t; t_0, \widetilde{\mathbf{P}}_b^p(t_0))\| \leq k\|\widetilde{\mathbf{P}}_b^p(t_0)\|\mathrm{e}^{-\lambda(t-t_0)}\ \forall t \geq t_0 \geq 0. \tag{9.71}$$

Since the system is asymptotically stable there exists a class $\mathcal{KL}$ function β such that $\forall\widetilde{\mathbf{P}}_b^p \in \Omega_p$, where Ω_p is the set of barycenter errors such that $\tilde{\mathbf{z}}_{t,1} \in \Omega$, the following holds:

$$\|\widetilde{\mathbf{P}}_b^p(t; t_0, \widetilde{\mathbf{P}}_b^p(t_0))\| \leq \beta(\|\widetilde{\mathbf{P}}_b^p(t_0)\|, t - t_0)\ \forall t \geq t_0 \geq 0. \tag{9.72}$$

By the asymptotic stability property, we know that $\exists T > 0$ such that at that $t = t_0 + T$ the solution enters the neighborhood of the origin where the convergence is

exponential. Consequently,

$$\begin{aligned}\int_{t_0}^{\infty} \|\widetilde{\mathbf{P}}_b^p(t; t_0, \widetilde{\mathbf{P}}_b^p(t_0))\| dt \leq & \int_{t_0}^{t_0+T} \beta(\|\widetilde{\mathbf{P}}_b^p(t_0)\|, t - t_0) dt \\ & + \int_{t_0+T}^{\infty} k\|\widetilde{\mathbf{P}}_b^p(t_0)\| \mathrm{e}^{-\lambda(t-t_0)} dt \\ & \leq T\beta(\|\widetilde{\mathbf{P}}_b^p(t_0)\|, 0) + \frac{k}{\lambda}\beta(\|\widetilde{\mathbf{P}}_b^p(t_0)\|, T).\end{aligned} \tag{9.73}$$

The right hand side is a class $\mathcal{K}$ function $\alpha(\|\widetilde{\mathbf{P}}_b^p(t_0)\|)$, and the third assumption is satisfied.

All assumptions of (Loría and Panteley; 2005, Theorem 2.1) are satisfied, thus the origin of the cascaded system is UGAS.

If the formation-keeping subsystem is only uniformly globally bounded, we can instead show uniformly globally boundedness of the path-parameter error system (9.60). The derivative of V_ξ along the trajectories of (9.60) are bounded by

$$\dot{V}_\xi \leq \left(-c_\xi \lambda_2 + 2U_{LOS} k_\xi\right) \|\tilde{\Xi}\|^2 + 2U_{LOS}\left(\frac{1}{\Delta} + k_\xi\right) \left(\sup_t \|\widetilde{\mathbf{P}}_b^p(t)\|\right) \|\tilde{\Xi}\|. \tag{9.74}$$

Which is negative outside the ball

$$\mathcal{B}_2 \coloneqq \left\{ \|\tilde{\Xi}\| \colon \|\tilde{\Xi}\| \geq \frac{2U_{LOS}(\frac{1}{\Delta} + k_\xi)}{\left(2U_{LOS} k_\xi - c_\xi \lambda_2\right)} \left(\sup_t \|\widetilde{\mathbf{P}}_b^p(t)\|\right) \right\}. \tag{9.75}$$

Therefore, the solutions to the system (9.60) will remain bounded if the formation-keeping errors remain bounded.

□

Now, we analyze the path-following subsystem (9.61)

Lemma 9.3. *The origin $\mathbf{p}_b^p$ is a UGAS equilibrium of the subsystem* (9.61) *if the formation-keeping task satisfies the asymptotic stability conditions of Lemma 9.1 and the positive parameters c_ξ, k_ξ, U_{LOS} are chosen such that $c_\xi \lambda_2 > 2U_{LOS} k_\xi$. Moreover, if the formation-keeping task is not asymptotically stable but ultimately bounded, then the trajectories of*

subsystem (9.61) *are ultimately bounded as well.*

Proof. Similarly to the previous lemma and the proof of Theorem 7.2 we analyze the system as a cascade where $\widetilde{\Xi}$, $\widetilde{\mathbf{P}}_b^p$ and $\widetilde{\mathbf{V}} = [\tilde{\mathbf{v}}_1, \ldots, \tilde{\mathbf{v}}_n]^\mathrm{T}$ perturbs the dynamics of $\mathbf{p}_b^p$ through $\widetilde{\mathbf{V}}_{LOS,d}$, $\widetilde{\mathbf{V}}$ and $\mathbf{G}$. The nominal system

$$\dot{\mathbf{p}}_b^p = -U_{LOS} \left[k_\xi \frac{x_b^p}{\sqrt{1 + (x_b^p)^2}}, \frac{y_b^p}{D}, \frac{z_b^p}{D} \right]^\mathrm{T}, \tag{9.76}$$

was proved USGES in Matouš, Pettersen, Varagnolo and Paliotta (2023b) and we restated the proof in our proof of Theorem 7.2.

Consider the Lyapunov function candidate

$$V_b(\mathbf{p}_b^p) = \frac{1}{2}(\mathbf{p}_b^p)^\mathrm{T}\mathbf{p}_b^p. \tag{9.77}$$

Similarly to the previous lemma, Assumption 3 in (Loría and Panteley; 2005, Theorem 2.1) is satisfied with $c_1 = \frac{1}{2}$, an arbitrary $\eta > 0$, and $c_2 = \eta$.

Let $\mathbf{h}$ denote the perturbing term in (9.61):

$$\mathbf{h} = \frac{1}{n} \sum_{i=1}^{n} \left(\mathbf{R}_p^T (\widetilde{\mathbf{v}}_{LOS,d,i} + \widetilde{\mathbf{v}}_i) + g_i \right). \tag{9.78}$$

From (9.54) and (9.57), we arrive at the following upper bound on the norm of $\mathbf{h}$

$$\begin{aligned} \|\mathbf{h}\| &\leq \left(2\frac{U_{LOS}}{\Delta} + U_{LOS} k_\xi \right) \|\widetilde{\mathbf{P}}_b\| + U_{LOS} k_\xi \|\widetilde{\Xi}\| + \|\widetilde{\mathbf{V}}\|, \\ &\leq \left(2\frac{U_{LOS}}{\Delta} + U_{LOS} k_\xi + 1 \right) \left\| \left[\widetilde{\mathbf{P}}_b, \widetilde{\Xi}, \widetilde{\mathbf{V}} \right] \right\|. \end{aligned} \tag{9.79}$$

Consequently, Assumption 4 in (Loría and Panteley; 2005, Theorem 2.1) is satisfied with $\theta_1 = (2\frac{U_{LOS}}{\Delta} + U_{LOS} k_\xi + 1)$ and $\theta_2 = 0$.

Assumption 5 in (Loría and Panteley; 2005, Theorem 2.1) is trivially satisfied for $\widetilde{\mathbf{V}}$ because of exponential stability. It was shown to be satisfied for $\widetilde{\mathbf{P}}_b$ in the previous

lemma, and it is satisfied for $\widetilde{\Xi}$ because the dynamics of $\widetilde{\Xi}$ are UGAS and there exists a time T after which it is USGES when the formation-keeping subsystem has entered the locally-exponentially-stable neighborhood.

All necessary assumptions of (Loría and Panteley; 2005, Theorem 2.1) are satisfied, and the path-following subsystem (9.61) is UGAS.

In the case when the formation-keeping subsystem is not asymptotically stable, but ultimately bounded, it can be shown similarly to the previous lemma that the solution to (9.61) remains bounded. The boundedness comes as a result of the perturbations entering the cascade linearly, i.e. $\theta_2 = 0$, and the nominal system being USGES. □

9.3 Stability of the full system

By combining the three previous lemmas we present the following theorem on the stability of the full system.

Theorem 9.4. *Let the fleet communication graph $\mathcal{G}$ be connected, and let $\lambda_{p,2}$, $\lambda_{d,2}$, $v_{2,\max}$, β_0, and ε be positive constants and choose γ_i so that*

$$\gamma_i \geq \beta_0 + \bar{\mu}_p + \frac{v_{2,\max}\lambda_{p,2}}{\lambda_{d,2}}|\mathbf{v}_i - \mathbf{v}_{d,i}|. \tag{9.80}$$

Furthermore, let the consensus gain $c_{\tilde{\xi}}$ be chosen so that $c_{\tilde{\xi}}\lambda_2 > 2U_{LOS}k_{\tilde{\xi}}$, where λ_2 is the Fiedler eigenvalue of $\mathbf{L}$, and let $k_{\tilde{\xi}}$, Δ, and U_{LOS} be positive constants. Then, for all initial conditions $[\mathbf{p}(0)^{\mathrm{T}}, \mathbf{v}(0)^{\mathrm{T}}]^{\mathrm{T}} \in \mathbb{R}^{6n}$ such that $\tilde{\mathbf{z}}_t(0) \in \Omega$, defined by (9.34)*, the trajectories of* (9.15) *and* (9.61) *remain ultimately bounded. Furthermore, when $\varepsilon \longrightarrow 0$ the origin of the system is asymptotically stable.*

Chapter 10

Simulations in MATLAB

Simulations are a powerful tool for evaluating the performance of multi-agent systems in various scenarios. In this chapter, we present the simulation of the system in MATLAB (The MathWorks Inc.; 2022), a widely-used platform for scientific computing and engineering applications. We develop a simulation framework that integrates the various components of the system, including path following, formation control, and obstacle avoidance, and demonstrate its effectiveness in a range of scenarios. The simulations provide insights into the system's behavior under different conditions and enable us to test and refine our control algorithms.

The chapter is organized as follows. Section 10.1 details the numerical model used in the simulations. Section 10.2 demonstrates the effectiveness of the centralized NSB algorithm through three different simulation scenarios. Section 10.3 demonstrates the effectiveness of the distributed NSB algorithm, first through a general experiment with collision avoidance, formation keeping, and path following, and then through three comparison studies with the first-order distributed method from Matouš, Pettersen, Varagnolo and Paliotta (2023a), the hand-position-based consensus method from Restrepo et al. (2022), and the alternative distributed formulation from Section 8.4.

10.1 Numerical AUV model

We chose the light autonomous underwater vehicle (LAUV), shown in Figure 10.1, as the vehicle model for simulation (Sousa et al.; 2012). The plant model in our simulation environment is set up to exactly match our ideal model (2.1). That means there are no modeling errors, and the fleet should behave as expected from theory. This section details the derivation of the numerical model used in the simulation.

Figure 10.1: The LAUV modeled in this simulation study. Image is taken from OceanScan website (OceanScan - MST; 2023).

A model for the LAUV with the origin of the coordinate frame at the center of buoyancy is developed in Estrela da Silva et al. (2007). The modeling closely follows that of (Fossen; 2021, Section 8.4). Following Assumption 2.3 from Chapter 2 we will develop the model around the pivot point (PP). We will first present a model with the origin at the center of buoyancy (CB) and then transform the model to the pivot point using the pivot point transformation (2.4). Following Estrela da Silva et al. (2007) we consider a LAUV with a length $L = 104\,\text{cm}$, a diameter $D = 15\,\text{cm}$, a mass of $18\,\text{kg}$ and distance between CB and center of gravity (CG) $z_g = 1\,\text{cm}$.

The mass matrix $\mathbf{M} = \mathbf{M}_{RB} + \mathbf{M}_A$ consists of the rigid body mass matrix and the added mass matrix. The rigid body mass matrix is derived as a diagonal matrix in CG and transformed to CB

$$\mathbf{M}_{RB}^{CB} = \mathbf{H}^{\mathrm{T}}([0\,0\,z_g]^{\mathrm{T}})\mathrm{diag}([m\,m\,m\,I_x\,I_y\,I_z])\mathbf{H}([0\,0\,z_g]^{\mathrm{T}}), \tag{10.1}$$

where $\mathbf{H}$ is a coordinate transformation matrix given in (Fossen; 2021, Appendix C), $I_x = \frac{1}{10}mD^2$ and $I_y = I_z = \frac{1}{20}m(L^2 + D^2)$. The added mass matrix is diagonal in CB

because of symmetry, and the numerical calculation can be found in (Fossen; 2021, Section 8.4). The resulting mass matrix with numerical values is given by

$$\mathbf{M}^{CB} = \begin{bmatrix} 19 & 0 & 0 & 0 & 0.18 & 0 \\ 0 & 34 & 0 & -0.18 & 0 & 0 \\ 0 & 0 & 34 & 0 & 0 & 0 \\ 0 & -0.18 & 0 & 0.04 & 0 & 0 \\ 0.18 & 0 & 0 & 0 & 1.8 & 0 \\ 0 & 0 & 0 & 0 & 0 & 1.8 \end{bmatrix}. \tag{10.2}$$

The corresponding damping matrix is taken from Estrela da Silva et al. (2007), and the non-linear part is neglected according to Assumption 2.5:

$$\mathbf{D}^{CB}(\zeta_r) = \begin{bmatrix} 2.4 & 0 & 0 & 0 & 0 & 0 \\ 0 & 23 & 0 & 0 & 0 & -11.5 \\ 0 & 0 & 23 & 0 & 11.5 & 0 \\ 0 & 0 & 0 & 0.3 & 0 & 0 \\ 0 & 0 & -3.1 & 0 & 9.7 & 0 \\ 0 & 3.1 & 0 & 0 & 0 & 9.7 \end{bmatrix}. \tag{10.3}$$

To derive the control-input matrix we consider fins with an x-position of $-0.455\,\mathrm{m}$ relative to the vehicle's mass center. Then, each newton meter of torque produced corresponds to $2.2\,\mathrm{N}$ produced force, which results in the following control-input matrix:

$$\mathbf{B}^{CB} = \begin{bmatrix} 1.0 & 0 & 0 & 0 \\ 0 & 0 & 0 & -2.2 \\ 0 & 0 & 2.2 & 0 \\ 0 & 1.0 & 0 & 0 \\ 0 & 0 & 1.0 & 0 \\ 0 & 0 & 0 & 1.0 \end{bmatrix}. \tag{10.4}$$

At this point, we note that, as a result of non-zero z_g implicitly violating the top-bottom symmetry assumption (Assumption 2.1), $\mathbf{M}^{CB}$ from (10.2) violates the structure from (Borhaug et al.; 2007, Equation 4). Therefore, it will not be possible to find a transformation that exactly satisfies Assumption 2.3. A common modeling approach is to neglect the off-diagonal elements of $\mathbf{M}^{CB}$ as they are dominated by the other modes of the system. The resulting model matrices are then given by

$$\mathbf{M} = \mathbf{H}_{PP}^{\mathrm{T}} \mathrm{diag}(\mathbf{M}^{CB}) \mathbf{H}_{PP}, \tag{10.5a}$$

$$\mathbf{D}(\boldsymbol{\zeta}_r) = \mathbf{H}_{PP}^{\mathrm{T}} \mathbf{D}^{CB}(\boldsymbol{\zeta}_r) \mathbf{H}_{PP}, \tag{10.5b}$$

$$\mathbf{B} = \mathbf{H}_{PP}^{\mathrm{T}} \mathbf{B}^{CB}, \tag{10.5c}$$

where $\mathbf{H}_{PP}$ is the pivot-point transformation matrix given by (2.4).

The Coriolis and centripetal matrix $\mathbf{C}(\boldsymbol{\zeta}_r) = \mathbf{C}_{RB}(\boldsymbol{\zeta}_r) + \mathbf{C}_A(\boldsymbol{\zeta}_r)$ consists of a rigid body term and an added mass term. Following (Fossen; 2021, Section 10.3), we carefully model the rigid-body Coriolis matrix independently of linear velocities so that the model correctly handles irrotational constant ocean currents. The resulting Coriolis matrices are given by

$$\mathbf{C}_{RB}(\boldsymbol{\zeta}_r) = \mathbf{H}_{PP}^{\mathrm{T}} \begin{bmatrix} \mathbf{S}(m\boldsymbol{\omega}) & \mathbf{0}_{3\times 3} \\ \mathbf{0}_{3\times 3} & \mathbf{S}([I_x p \; I_y q \; I_z r]^{\mathrm{T}}) \end{bmatrix} \mathbf{H}_{PP}, \tag{10.6}$$

$$\mathbf{C}_A(\boldsymbol{\zeta}_r) = \begin{bmatrix} \mathbf{0}_{3\times 3} & -\mathbf{S}(\mathbf{A}_{11}\boldsymbol{\nu}_r + \mathbf{A}_{12}\boldsymbol{\omega}) \\ -\mathbf{S}(\mathbf{A}_{11}\boldsymbol{\nu}_r + \mathbf{A}_{12}\boldsymbol{\omega}) & -\mathbf{S}(\mathbf{A}_{21}\boldsymbol{\nu}_r + \mathbf{A}_{22}\boldsymbol{\omega}) \end{bmatrix}, \tag{10.7}$$

where

$$\mathbf{H}_{PP}^{\mathrm{T}} \mathbf{M}_A \mathbf{H}_{PP} \coloneqq \begin{bmatrix} \mathbf{A}_{11} & \mathbf{A}_{12} \\ \mathbf{A}_{21} & \mathbf{A}_{22} \end{bmatrix}. \tag{10.8}$$

10.2 Centralized NSB algorithm simulation results

This section presents three different simulation experiments with the centralized second-order NSB method from Chapter 6. Section 10.2.1 details a simulation experi-

ment with three AUVs equipped with the centralized NSB controller with the collision cones obstacle avoidance method detailed in Section 6.6.1. Section 10.2.2 details a similar experiment but with obstacle avoidance implemented as an individual high-priority task for each vehicle as detailed in Section 6.6.2. Section 10.2.3 demonstrates through simulation how the second-order NSB algorithm enables us to specify the formation-keeping task as an interpretable spring-damper system.

10.2.1 General three-agent mission

This section presents a general simulation scenario that demonstrates the effectiveness of the complete system. The fleet consists of three vehicles equipped with the NSB controller (6.3), with the choice of integral action (Section 6.5.1) to compensate for the unknown ocean current and the collision cones method (Section 6.6.1) to avoid obstacles. The fleet should follow a continuous spiral-shaped path while avoiding collision with a cylindrical-shaped obstacle with radius 10 m and base circle in the $xy-$plane and origin $[x,\ y] = [100,\ -10]$. In the rest of this section, all distances will be given in meters, and units are omitted for simplicity.

The prescribed path is given by the following spiral-equation

$$\mathbf{p}_p(\xi) = \mathbf{p}_{p,0} + \left[\xi, -40\cos(\tfrac{\pi}{100}\xi), 20\sin(\tfrac{\pi}{100}\xi)\right]^{\mathrm{T}}, \tag{10.9}$$

where

$$\mathbf{p}_{p,0} = \left[0, -40, 35\right]^{\mathrm{T}}. \tag{10.10}$$

The barycenter relative formation is given by

$$\mathbf{p}^{f}_{f,1:3} = \begin{bmatrix} 0 & 0 & 0 \\ 10 & -10 & 0 \\ 5 & 5 & -10 \end{bmatrix}, \tag{10.11}$$

and the collision avoidance task is configured to ensure a safe distance of 10 m both between vehicles in the fleet and external obstacles. Because the cylinder radius is

10 m, its avoidance radius, r_o, is 20 m. The activation angle $\alpha_{\min}$ is chosen as 15°. The vehicles are subject to an unknown ocean current

$$\mathbf{v}_c = \begin{bmatrix} 0 & 0.25 & 0.05 \end{bmatrix}^{\mathrm{T}} \text{ m/s}. \tag{10.12}$$

The controller gain matrices $\mathbf{\Lambda}_{p,1}$, $\mathbf{\Lambda}_{d,1}$, $\mathbf{\Lambda}_{p,2}$, $\mathbf{\Lambda}_{d,2}$, $\mathbf{\Lambda}_{p,3}$, and $\mathbf{\Lambda}_{i,3}$ from (6.10), (6.17), and (6.29) are chosen as scaled identity matrices $k_i\mathbb{I}$. The gains, as well as controller parameters $v_{2_{\max}}$, Δ_0, U_{LOS}, and $k_{\tilde{\xi}}$ from (6.17) , (6.19), (6.20), and (6.27), and the hand length h are given by Table 10.1. The hand length is chosen as 5 m following Matouš, Paliotta, Pettersen and Varagnolo (2023) where the same AUV was simulated.

Table 10.1: Controller parameters used in simulation

Parameter	Value
$k_{p,1}$	1
$k_{d,1}$	0.2
$k_{p,2}$	0.5
$k_{d,2}$	1
$k_{p,3}$	1
$k_{i,3}$	1
U_{LOS}	1.5 m/s
Δ_0	5 m
$k_{\tilde{\xi}}$	0.2
$v_{2_{\max}}$	0.75 m/s
h	5 m

We initialize the fleet with barycenter $\mathbf{p}_b = [-5,\ -100,\ 18]^{\mathrm{T}}$ and relative positions

$$\boldsymbol{\sigma}_{2,1:3} = \begin{bmatrix} 0 & 0 & 0 \\ -15 & 15 & 0 \\ -7 & -7 & 14 \end{bmatrix}. \tag{10.13}$$

The resulting North-East trajectory of the mission is shown in Figure 10.2. The

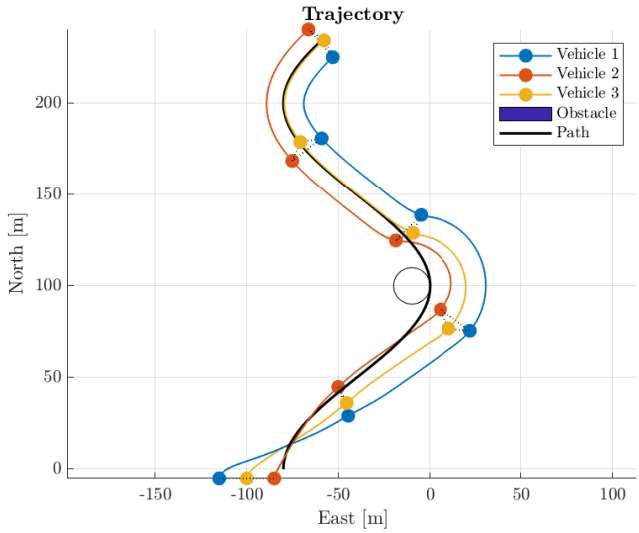

Figure 10.2: The trajectory of the vehicles. The markers represent the vehicle positions every 50 seconds.

vehicles avoid the obstacle with a margin and return to the desired path. The fleet deviates from the desired path right away, because the path is inside the obstacle's collision cone as illustrated in Figure 6.1b. The avoidance maneuver is further detailed in Figure 10.3a. The collision cones avoidance task is active from the beginning of the mission until the obstacle is passed. In other words, the fleet proactively changes its path early in order to avoid the obstacle. The minimum distance between the fleet and the obstacle is 10 m as expected when the obstacle avoidance radius r_o is chosen 10 m larger than the obstacle radius. The distance is at its minimum at the 100-second mark. Then, it can be seen from the third set of markers in Figure 10.2 that the fleet path is tangent to the obstacle, which is the expected behavior of the collision cones avoidance method. Figure 10.3a further shows that the inter-vehicle COLAV task activates when the distance between vehicles is below $d_{COLAV} = 10$ m. The distance slightly oscillates below the threshold. The oscillation can be expected because $k_{p,1}$ and $k_{d,1}$ are chosen so that the system is underdamped. The distance can reduce slightly below the threshold because the task does not activate before the threshold is violated.

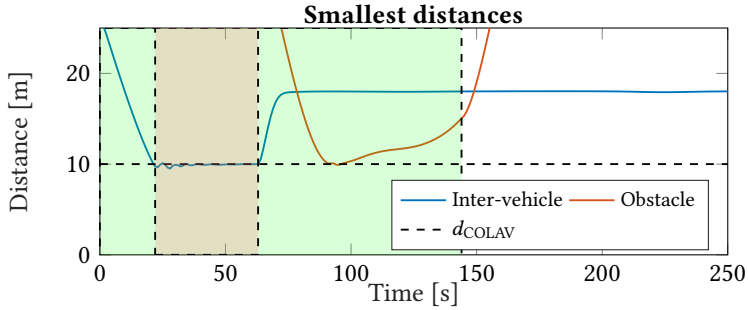

(a) The minimum inter-vehicle and obstacle distance.

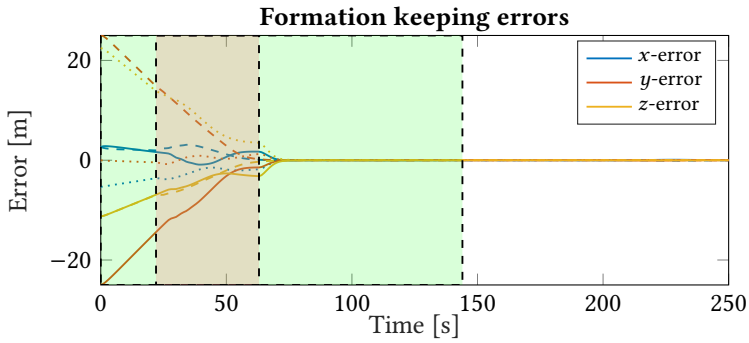

(b) The formation keeping errors.

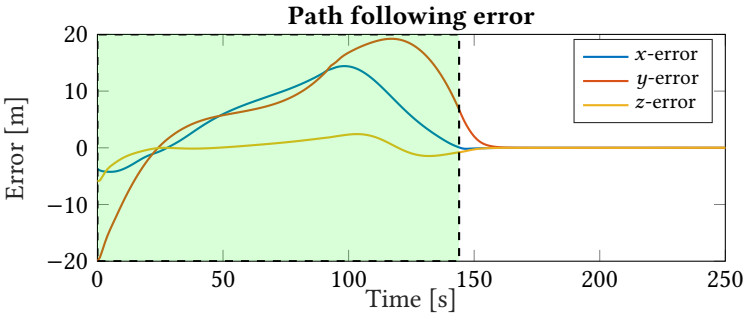

(c) The path-following error of the barycenter.

Figure 10.3: Error variables from the simulated mission. The full, dashed, and dotted lines correspond to the three different vehicles. The green and red rectangles represent when obstacle avoidance or inter-vehicle COLAV is active.

Figure 10.3b shows that the fleet converges to the desired formation during the obstacle avoidance maneuver. The obstacle avoidance task specifies common accelerations to all vehicles and does therefore not interfere with the formation-keeping task. Except for during the inter-vehicle collision avoidance, the convergence seems linear, which can be expected because the task velocity is saturated by $v_{2,\max}$. The formation-keeping errors asymptotically converge to zero in accordance with Theorem 7.1.

Figure 10.3c shows that the path-following error initially increases as the fleet avoids the obstacle because the x- and y-components of $\mathbf{v}_{LOS,d}$ and $\dot{\mathbf{v}}_{LOS,d}$ are replaced with $\mathbf{v}_{OA,d}$ and $\dot{\mathbf{v}}_{OA,d}$ given by (6.39), (6.40). As expected from Theorem 7.2, the error converges to zero after the obstacle is passed when the LOS task is activated again. The constant ocean current is accurately compensated for by the integral action, and the path-following error remains at zero for the rest of the mission.

Figure 10.4a shows that the angular velocities remain bounded, in accordance with Theorem 7.4. Figure 10.4b shows that the surge velocities of all vehicles remain between 1 m/s and 2 m/s, which is expected, as the velocity should remain in the interval $U_{LOS} \pm v_{2_{\max}} = [0.75,\ 2.25]$, except for during inter-vehicle collision avoidance maneuvers. Furthermore, this range includes the expected operating surge velocity of the vehicle the simulation is modeled after.

10.2.2 Individual obstacle avoidance

In this section, we examine a simulation study of the NSB formation path-following problem with the obstacle avoidance method from Section 6.6.2 adapted from Arrichiello et al. (2006). A key difference from the collision cones method simulated in the previous section is that this method enables the fleet to break formation in order to avoid collisions. Furthermore, this method enables the vehicles to conduct avoidance maneuvers in all three dimensions and not only in the xy plane.

The simulation setup is similar to the previous section, with the same desired path, external obstacle, constant ocean current, and initial states. Furthermore, all controller gains and parameters are also the same, given by Table 10.1.

The resulting trajectory in the NED coordinate frame is shown in Figure 10.5. The fleet splits up the formation to pass the obstacle and converges back to the formation

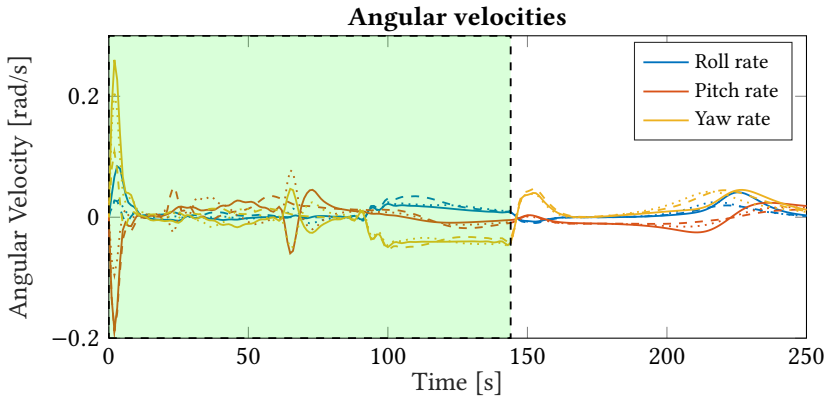

(a) The angular velocities of the vehicles. Dashed and dotted lines represent different vehicles.

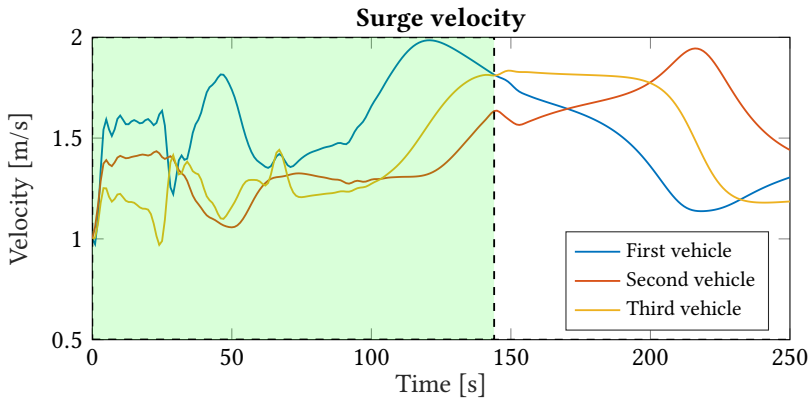

(b) The surge velocities of the vehicles.

Figure 10.4: Angular and surge velocities for the vehicles in the first simulated mission. The green rectangle represents the time when the collision avoidance task was active.

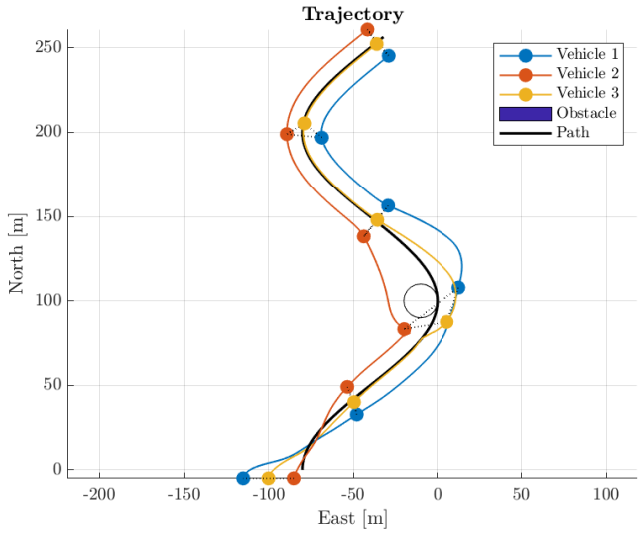

Figure 10.5: The trajectory of the vehicles. The markers represent the vehicle positions every 50 seconds.

after the obstacle is passed. Compared to the collision cones avoidance method, the fleet deviates late from the path in order to avoid the obstacle, which is further shown in Figure 10.6a, where the green rectangle represents when the external collision avoidance task is active. As also seen in Figure 10.6a, the inter-vehicle collision avoidance still works well, despite now being defined as individual tasks for each vehicle, which is expected because the formulation with individual tasks should be equivalent to the joint formulation, as long as only two vehicles are within the collision threshold of each other.

Figure 10.6c shows that the fleet converges earlier to the correct path and deviates minimally from it during the avoidance maneuver. The limited deviation is possible because the path error is defined in terms of the barycenter, and as long as some vehicles of the fleet are on each side of the obstacle, it is possible for the barycenter to remain on the path. Instead, the formation-keeping error increases during the avoidance maneuver, as seen in Figure 10.6b. With the collision cones avoidance method from the previous section, the formation was kept during obstacle avoidance.

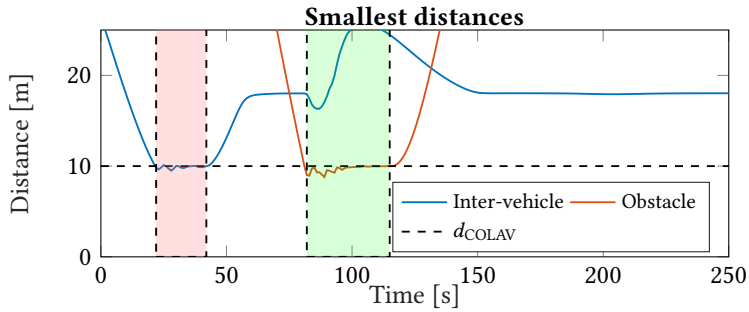

(a) The minimum inter-vehicle and obstacle distance.

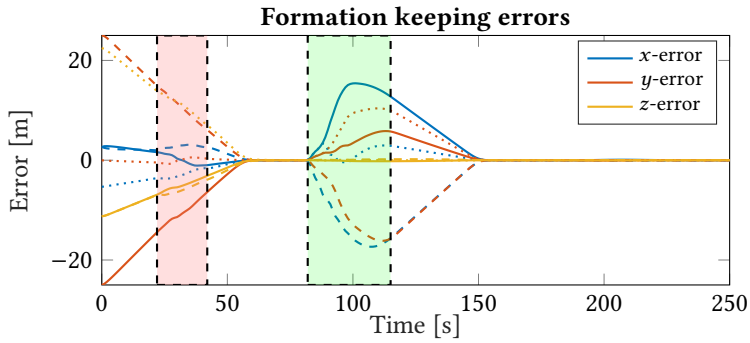

(b) The formation keeping errors.

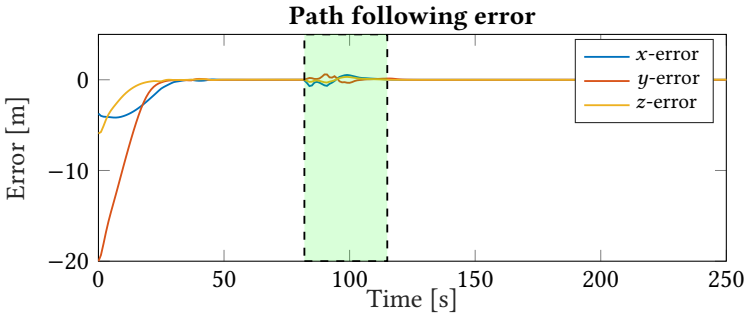

(c) The path-following error of the barycenter.

Figure 10.6: Error variables from the second simulated mission. The full, dashed, and dotted lines correspond to the three different vehicles. The green and red rectangles represent when obstacle avoidance or inter-vehicle COLAV is active.

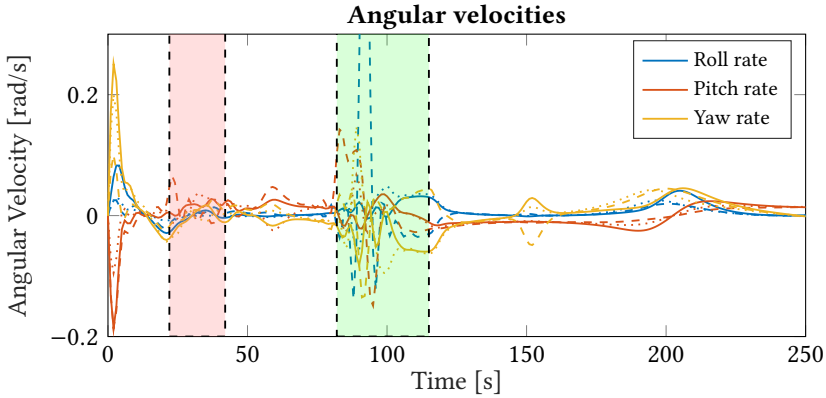

(a) The angular velocities of the vehicles. Dashed and dotted lines represent different vehicles.

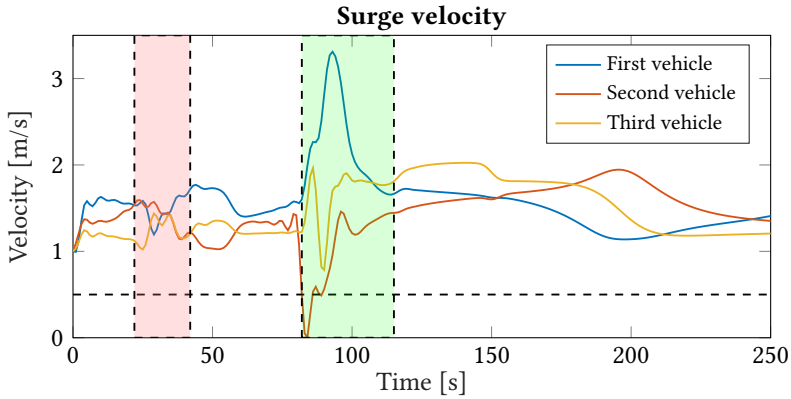

(b) The surge velocities of the vehicles.

Figure 10.7: Angular and surge velocities for the vehicles in the second simulated mission. The green rectangle represents the time when the collision avoidance task was active.

Figure 10.7b shows that the surge velocities of the vehicles rise above 3 m/s and sink below 0.5 m/s. Velocities above 3 m/s are unexpected, as it is above the maximum operating velocity of the physical vehicles that the simulation models. There are two possible explanations for such a high velocity. First, the controller might command generalized forces that are larger than the limits of the physical systems actuators. Actuator saturation was not modeled, and such forces would be applied directly to the plant in our simulator. In a real system with actuation limits, the control action going into saturation might impose a stability problem. A second explanation for the large surge velocities is that the simulation does not model non-linear damping. In a more realistic simulator, the non-linear damping would become significant when the velocities increase above the nominal operating range. It is also problematic that the velocity of a vehicle sinks below 0.5 m/s. Then, a real, physical vehicle would lose controllability because water does not flow sufficiently fast past the fins.

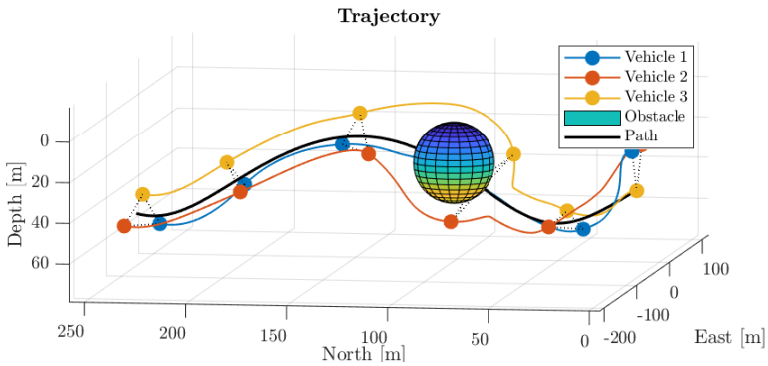

Figure 10.8: Illustration of obstacle avoidance in all three dimensions. The obstacle is chosen as a sphere.

Another feature that distinguishes this obstacle avoidance method from the collision cones method is that it enables obstacle avoidance in all three dimensions. In the collision cones method, the avoidance maneuver was limited to the xy-plane. As demonstrated in Figure 10.8, the obstacle avoidance method as described in Section 6.6.2 enables each individual vehicle to independently avoid the obstacle in all dimensions. The spherical obstacle in this experiment was chosen larger than the cylindrical obstacle in the previous experiments for illustrative purposes.

10.2.3 Formation error as damped harmonic motion

Part of the motivation for developing the second-order NSB controller is that there are no hidden dynamics abstracted away in the low-level control layer. Consequently, the collision-avoidance and formation-keeping error systems are expected to behave exactly as second-order systems defined by the gain matrices. In turn, the gain matrices can be chosen by specifying natural frequencies and damping ratios as described in Section 5.4. In this section, we will observe the transient of the formation-keeping error under different controller gains. Although we demonstrate the concept with the formation-keeping error, the same behavior is expected for the collision-avoidance task as well.

We design a simple simulation experiment in which everything except for the formation-keeping task is simplified as much as possible. The fleet is made to follow a straight line in the north direction. It is initialized with the barycenter on the path, and there is no external obstacle or ocean current. The desired formation is given by (10.11) as in the previous simulation experiments, and the initial relative positions are given by $\boldsymbol{\sigma}_{2,i} = 2\mathbf{p}^f_{f,i}$. All controller gains and parameters except for $k_{p,2}$ and $k_{d,2}$ are given by Table 10.1. We simulate three different choices of formation-keeping controller gains given by Table 10.2. The natural frequency is kept fixed at $\omega_{n,2} = 0.5$ which is low enough so that the effects of the saturation in the controller are minimal, and the damping ratio is chosen so that the system is underdamped, critically damped, and overdamped for the respective three experiments. The total simulation time is 50 s.

Table 10.2: Controller parameters for the three experiments.

Parameter	Experiment 1	Experiment 2	Experiment 3
$\omega_{n,2}$	0.5	0.5	0.5
ξ_2	0.3	1	2
$k_{p,2}$	0.25	0.25	0.25
$k_{d,2}$	0.3	1	2

Figure 10.9 shows the north-east trajectory for the vehicles with different damping ratios. The corresponding formation-keeping errors are shown in Figure 10.10. As

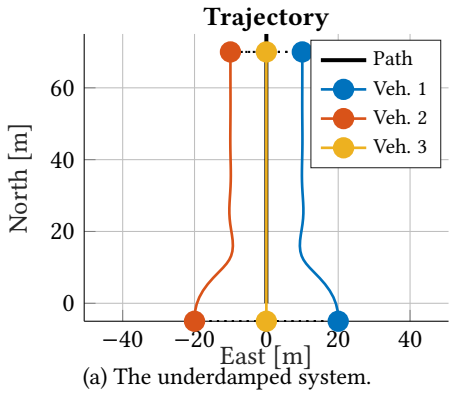

(a) The underdamped system.

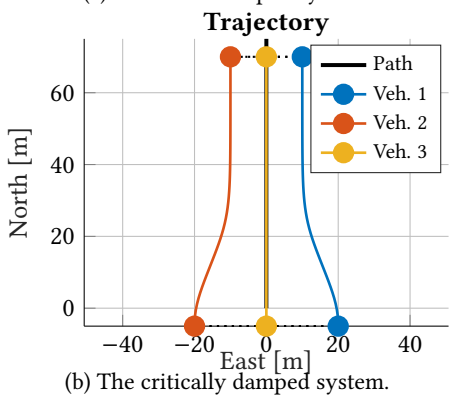

(b) The critically damped system.

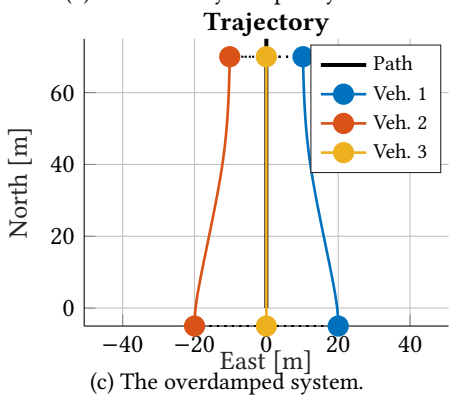

(c) The overdamped system.

Figure 10.9: The north-east trajectories of the vehicles with different formation-keeping controller gains.

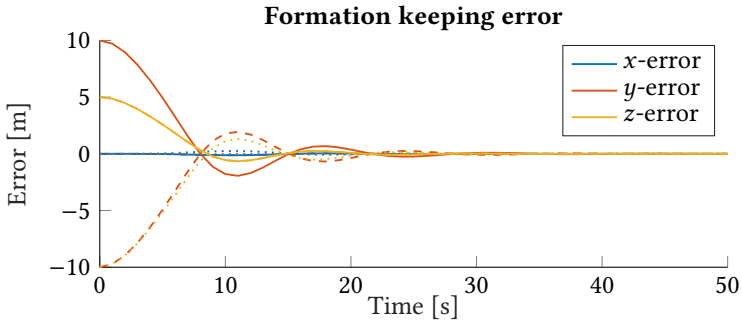

(a) The underdamped system.

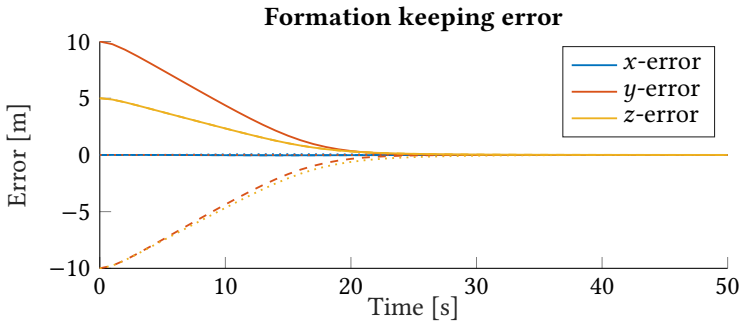

(b) The critically damped system.

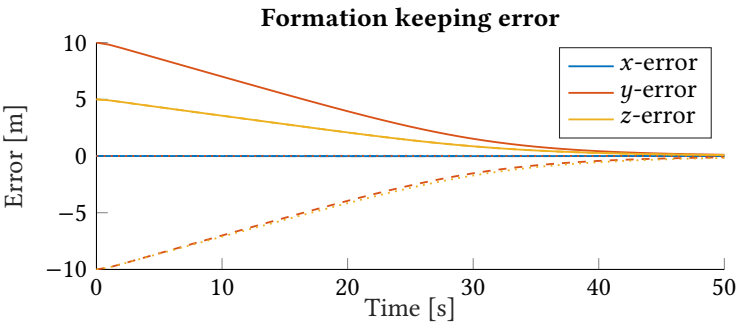

(c) The overdamped system.

Figure 10.10: The formation-keeping errors for the vehicles with different formation-keeping controller gains. The full, dashed, and dotted lines illustrate the different vehicles.

expected, the formation-keeping error in the underdamped system exhibits an oscillatory motion. The error in the critically damped system converges quickly to the origin without oscillations, and the overdamped system converges more slowly. Despite the saturation term in the formation-keeping acceleration (6.17), the task errors converge as can be expected from the theory of damped harmonic motion.

10.3 Distributed NSB algorithm simulation results

This section presents three simulation experiments with the distributed NSB method from Chapter 8. The method is first demonstrated on a general mission featuring collision avoidance, formation keeping, and path following in Section 10.3.1. Then, the method is compared to two existing methods from the literature in Sections 10.3.2 and 10.3.3, and the alternative distributed implementation in Section 10.3.4. The method is configured with the sliding-mode path-following acceleration given by (8.18).

10.3.1 General five-agent mission

This section presents a simulation experiment of the distributed NSB control law presented in Chapter 8. The experiment involves a fleet of five agents with a communication graph given by Figure 10.11. All controller gains and parameters are unchanged from previous experiments and given by Table 10.1.

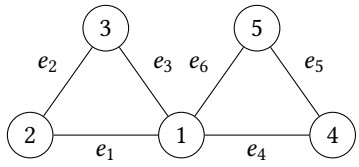

Figure 10.11: The communication graph of the fleet.

The barycenter relative vectors give the desired formation:

$$\mathbf{p}^f_{f,1:5} = \begin{bmatrix} 0 & 8 & 8 & -8 & -8 \\ 0 & -8 & 8 & 8 & -8 \\ 8 & -2 & -2 & -2 & -2 \end{bmatrix}. \tag{10.14}$$

The desired formation-relative positions of the agents 2-5 make up a square in the xy-plane. The fleet is initialized so that each of the four agents starts at opposite corners of the square. The initial positions are chosen slightly closer than the desired formation so that the inter-vehicle collision avoidance task activates:

$$\mathbf{p}_{1:5}(0) = \begin{bmatrix} 0 & -5 & -5 & 5 & 5 \\ 0 & 5 & -5 & -5 & 5 \\ 5 & -1.25 & -1.25 & -1.25 & -1.25 \end{bmatrix}. \tag{10.15}$$

The fleet avoids the obstacle and converges to the desired path as seen by Figure 10.12. Figure 10.13 shows more clearly that the formation-keeping and path-following errors converge to and remain at zero. Figure 10.13a shows that the collision avoidance task works similarly to the centralized algorithm, with only small violations of the collision-avoidance threshold.

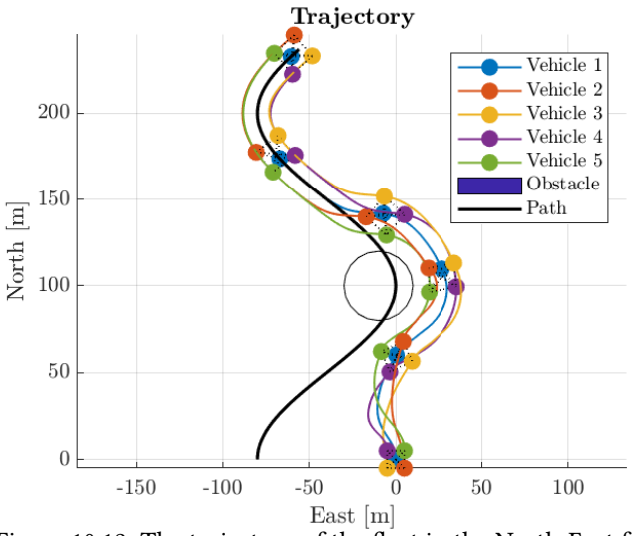

Figure 10.12: The trajectory of the fleet in the North-East frame.

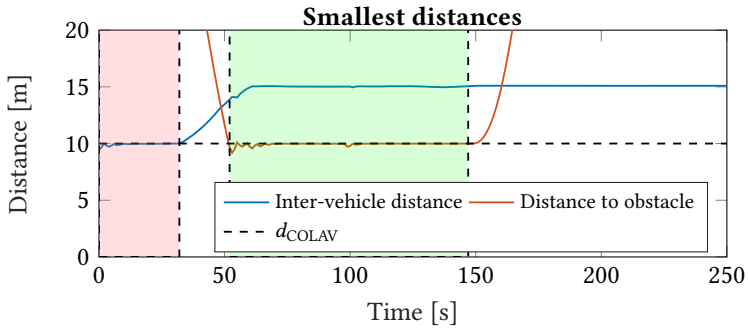

(a) The minimum inter-vehicle and obstacle distance.

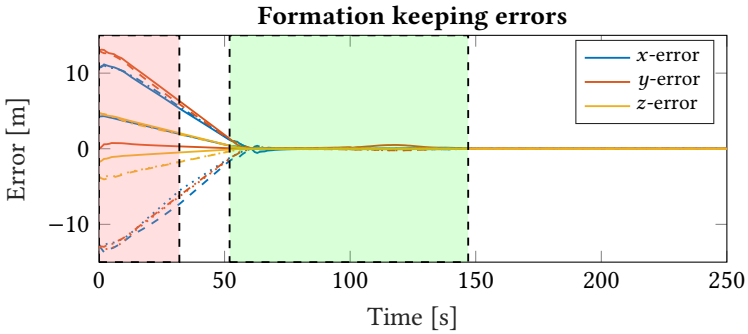

(b) The formation keeping errors.

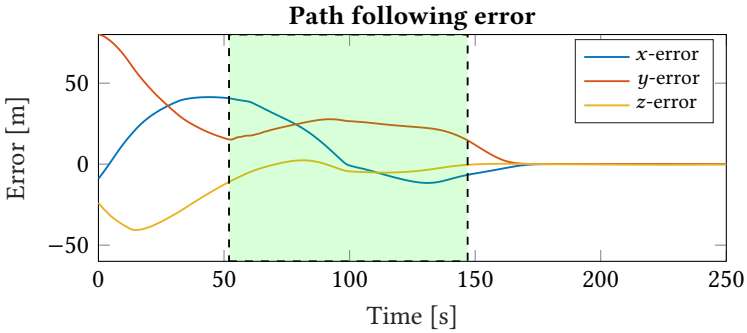

(c) The path-following error of the barycenter.

Figure 10.13: Error variables from the simulated distributed mission. The different line styles correspond to the five different vehicles. The green and red rectangles represent when obstacle avoidance or inter-vehicle COLAV is active.

10.3.2 Comparison study with the first-order NSB method

In this section, we compare our distributed NSB method with the first-order NSB method from Matouš, Pettersen, Varagnolo and Paliotta (2023a). The Simulink model for the first-order method was provided by Josef Matouš. The first-order method is implemented in a distributed manner as described in Section 8.4.

We simulate the two methods on the four-vehicle simulation experiment detailed in Matouš, Pettersen, Varagnolo and Paliotta (2023a). We choose the experiment without obstacles because the two methods implement obstacle avoidance differently. Furthermore, the inter-vehicle collision avoidance threshold is chosen small enough for the task to not activate because the provided implementation of the first-order NSB does not include that task. The barycenter should follow an elliptic path given by

$$\mathbf{p}_p(\xi) = [a\cos\xi,\ b\sin\xi,\ c\sin\xi^2]^{\mathrm{T}}, \tag{10.16}$$

where $a = 60\,\mathrm{m}$, $b = 40\,\mathrm{m}$, $c = 10\,\mathrm{m}$. The shape of the desired formation is given by

$$\mathbf{p}^f_{f,1:4} = \begin{bmatrix} 10 & -10 & 0 & 0 \\ 0 & 0 & 10 & -10 \\ 0 & -4 & 4 & 0 \end{bmatrix}, \tag{10.17}$$

and the communication graph is given by Figure 10.14.

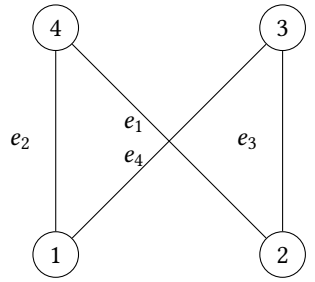

Figure 10.14: Communication graph for the comparison experiment.

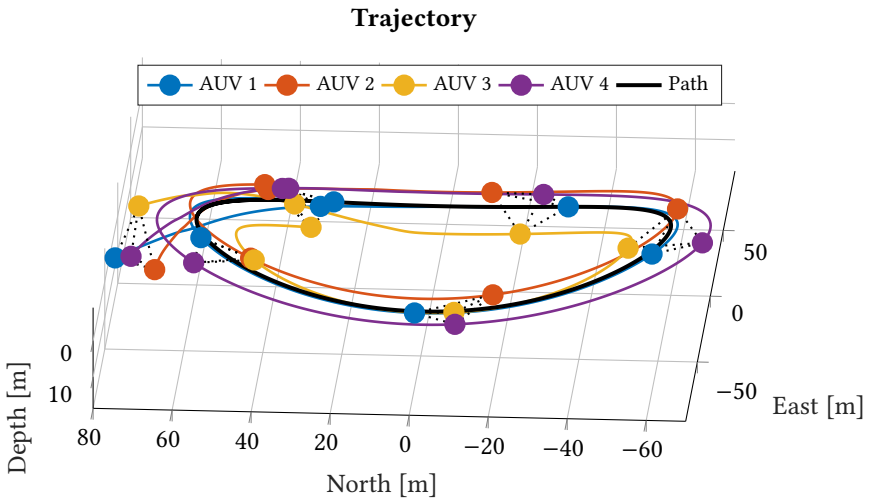

Figure 10.15: The 3D trajectory from the second-order NSB method in the comparison experiment.

The 3D trajectory of our method is shown in Figure 10.15. The norm of the path-following error for both methods is shown in Figure 10.16a and the norm of the formation-keeping error is shown in Figure 10.16b. The error norm is plotted on a semi-logarithmic plot to emphasize the ultimate error of both methods.

The plots show that with the first-order method, the error converges quicker, but to a higher final error. The difference in convergence speed comes from the fact that our method implements a saturated formation-keeping task whereas the first-order method does not. As a result, the first-order method is UGES, while our method is ULES in the formation-keeping task. In the semi-logarithmic plot in Figure 10.16b, exponential decay will show as a linear graph. Clearly, the first-order method decays exponentially from the start, whereas our second-order method starts decaying exponentially at around 50 s, which can be interpreted as the point when the formation-keeping subsystem enters the locally exponentially stable neighborhood.

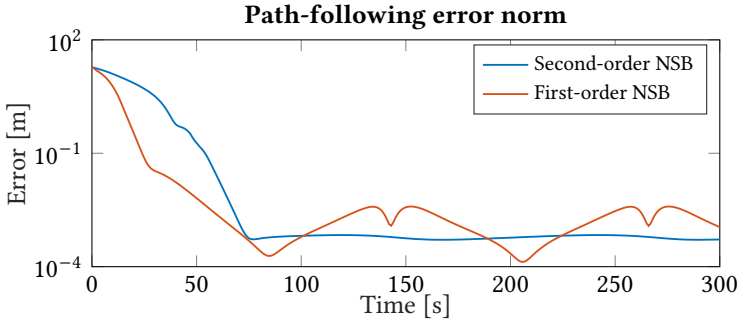

(a) Comparison of the path-following error.

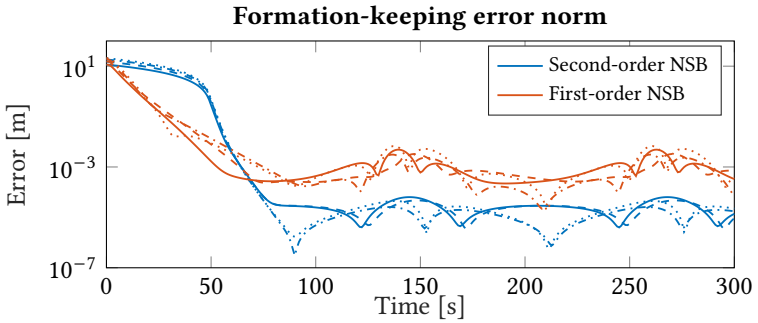

(b) Comparison of the formation-keeping error. Different line styles represent different vehicles.

Figure 10.16: Comparison between the first-order NSB method from Matouš, Pettersen, Varagnolo and Paliotta (2023a) and our second-order NSB method. Our method converges slower but to a lower absolute error.

In this ideal simulation setup, our method, benefiting from the model-based hand-position controller's ability to accurately compensate for system non-linearities, achieves a smaller steady-state error. Because our second-order method has no dynamics abstracted away in a lower-level control layer, the error should approach machine precision following Lemmas 9.1 and 9.3 if a discontinuous switching sliding-mode controller was used. However, in practice, several factors prevent this ideal behavior.

Firstly, the switching sliding-mode term in (8.13) is replaced by a continuous saturation function in our implementation. As a result, we can only expect a bounded formation-keeping error since the disturbance $\boldsymbol{\mu}_p$ in (9.15) is nonvanishing at $\tilde{\mathbf{z}}_{t,2} = \mathbf{0}$.

Furthermore, the asymptotic stability of the formation-keeping subsystem is a prerequisite for the stability of the path-following subsystem in Lemma 9.3. Therefore, the path-following subsystem will not be asymptotically stable as well. Nevertheless, a bounded formation-keeping subsystem will result in a bounded path-following subsystem. Moreover, Lemma 9.3 was only proven for straight-line paths and this experiment had an elliptic path.

Lastly, we may observe some discrepancies because of numerical inaccuracies when applying the hand-position controller on a simulated system compared to applying the NSB method directly on a second-order integrator system.

The errors of the first-order method are not expected to vanish to zero because of the extra dynamics from the low-level control. Despite our second-order method resulting in lower errors in this simulation experiment, it is crucial to acknowledge that the low-level PID controllers in the first-order method may offer greater robustness when dealing with real systems affected by modeling errors. To the best of our knowledge, there have not yet been developed robustness guarantees for the hand-position controller. Nonetheless, these promising simulation results highlight the effectiveness of our method compared to the state-of-the-art alternative.

10.3.3 Comparison study with a consensus method

This section provides a simulated experiment that compares our method with the consensus method developed by Restrepo et al. (2022). The most important properties

of the consensus method were presented in the literature study in Section 1.2. We developed the Simulink model for the consensus law ourselves and trivially extended it to 6-DOF by combining the method with the 6-DOF hand-position controller. Because the consensus method is initially designed as a target tracking method, we choose the following update law inspired by Paliotta et al. (2019) for the virtual target's path parameter to facilitate path following

$$\dot{\xi} = \mathbf{U}_d \left\| \frac{\partial \mathbf{p}_p(\xi)}{\partial \xi} \right\|^{-1} \left(1 - k_{\xi} \tanh \|\mathbf{p}_1 - \mathbf{p}_p - \mathbf{z}_{p,d}\|\right), \tag{10.18}$$

where $U_d = 1.3\,\mathrm{m/s}$ is the desired path-following velocity, $k_{\xi} = 0.5$ is a control parameter, and $\mathbf{z}_{p,d}$ is the desired displacement between the leader vehicle and the path.

The two methods are tested on the same simulation scenario as described in the previous section. Unlike in the previous section, the inter-vehicle collision avoidance threshold is now chosen as 7 m because both methods implement some form of collision avoidance.

There are some clear differences and similarities between the two methods. The main similarity is that both control laws leverage the same hand-position input-output linearizing controller to simplify the nonlinear vehicle dynamics. Furthermore, both methods rely on a consensus law with a switching sliding-mode term for formation keeping. An important difference that may affect the performance of the methods is that in the consensus algorithm from Restrepo et al. (2022) only the first vehicle is assumed to have access to the target. Because the rest of the fleet does not have access to the target, and thus the orientation of the path-tangential coordinate frame, the desired formation for the consensus method is with respect to the NED coordinate frame, whereas the desired formation in our method is with respect to the path-tangential coordinate frame.

The simulation results are presented in Figure 10.17. Note that unlike previous plots of formation-keeping error in this thesis, Figure 10.17b shows the formation-keeping error as the edge-consensus errors $\|\tilde{\mathbf{z}}_1\|$. It can be seen from the initially linear graphs in the semilogarithmic plots in Figures 10.17a and 10.17b that the consensus method has exponential convergence. As discussed in the previous section, our method

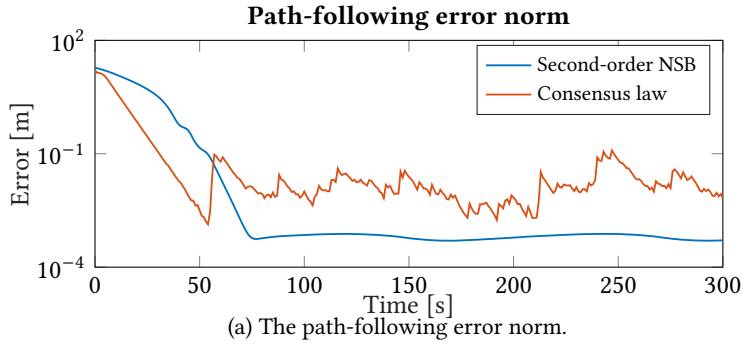

(a) The path-following error norm.

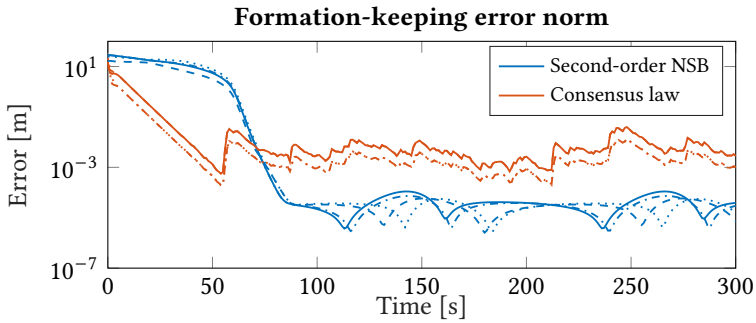

(b) The formation keeping errors. The errors are given as the edge-agreement errors for the four edges in the communication graph.

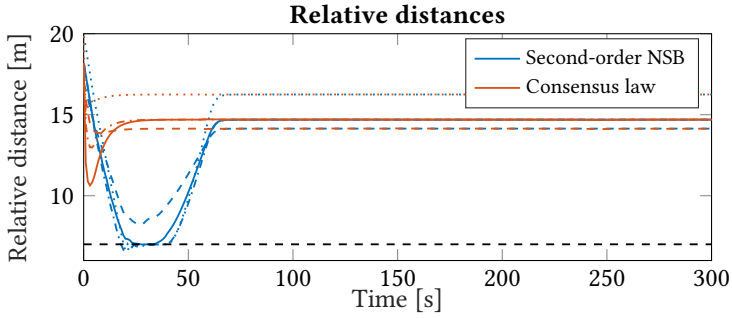

(c) The relative inter-vehicle distance for the four edges in the communication graph.

Figure 10.17: Error variables comparing the consensus method from Restrepo et al. (2022) with our method. The different line styles correspond to the four edges of the communication graph.

converges slower because of the saturated formation-keeping acceleration and the constant velocity line-of-sight path-following law. Further inspection of the simulation data shows that for the consensus method, the commanded surge force peaks at $\sim 800\,\mathrm{N}$ whereas our method peaks at $\sim 40\,\mathrm{N}$. The force is larger than a physical system can produce for both methods, but the consensus method violates the limits of a physical system more severely than ours. One of the reasons why we implemented a saturated formation-keeping acceleration and a constant velocity line-of-sight law in the first place was to limit the control action at large errors.

Our method converges to a significantly lower error than the consensus law, which is surprising, as both methods leverage the same hand-position controller and none of them have hidden dynamics from low-level control. One would therefore expect both methods to have low path-following and edge-consensus errors, only limited by the continuous approximation of the switching control. We were not able to further improve the results from the consensus method by modifying the approximation of the switching function.

Figure 10.17c shows that the two methods handle collision avoidance differently. In the consensus control law, collision avoidance is managed through a BLF. Collision avoidance through the BLF is always active, and the control action goes to infinity as the vehicles approach the distance threshold. As a result, no pair of vehicles ever come close to the threshold. In our method, on the other hand, the collision avoidance task only activates when the threshold is violated. It is therefore expected that the vehicles will transiently violate the threshold, but quickly recover to safe distances.

In conclusion, our method performs at least as well if not better than the consensus method from Restrepo et al. (2022). The trajectories converge slower by design, but the ultimate error is lower, and furthermore, the error plots seem smoother. Both methods rely on the same hand-position controller for handling the nonlinear equations of motion. When implementing the methods on a real system, the robustness of the hand-position controller is one of the main concerns, and since it is the same for both methods we cannot say that one method is expected to have an advantage over the other when going from simulation to real experiments.

10.3.4 Comparison with the alternative distributed NSB method

In this section, we compare the two different distributed formulations of the second-order NSB method. We refer to the firstly presented method from Chapter 8 as the *novel* method and the secondly presented method as the *alternative* method. The simulation setup is the same as the previous two sections. All common controller gains are chosen to be equal and given by Table 10.2. The gains c_b and k_b for the barycenter estimate updates of the alternative formulation are chosen as the LQR gain of an integrator system with an identity input matrix and weighting matrices $\mathbf{Q} = 100\mathbf{I}_2$ and $\mathbf{R} = \mathbf{I}_2$.

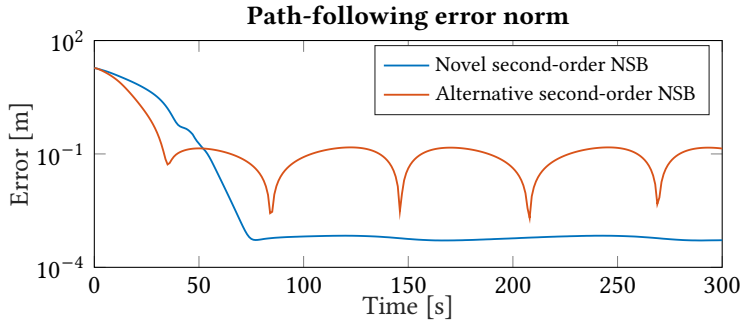

(a) Comparison of the path-following error.

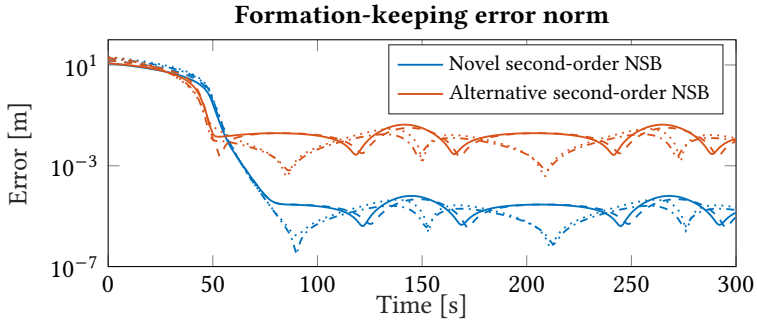

(b) Comparison of the formation-keeping error. The line styles represent different vehicles.

Figure 10.18: Comparison between the two different distributed formulations of the second-order NSB method.

Figure 10.18 shows the simulation results. Our novel distributed method has a lower error compared to the alternative distributed method. The sliding-mode terms are a possible explanation. They help increase the robustness to modeling errors such as imperfect cancellations of nonlinear dynamics in the hand-position controller. Interestingly, the formation-error plots look very similar for the two methods, only differing by scale. This can be attributed to both methods being fundamentally the same control law, only with different approaches to making them distributed. Both methods leverage the same hand-position controller and split motion control into a path-following and a formation-keeping task.

To verify our hypothesis that the difference in error comes from the sliding-mode terms, we conduct another simulation experiment. In this experiment, we remove the sliding-mode term from the path-following acceleration by replacing (8.18) with (8.16). Additionally, we eliminate the switching term from (8.13). The resulting simulation errors are shown in Figure 10.19. Clearly, the two methods have almost identical performance, with the only noticeable difference being that our novel method converges slightly slower to the desired path. This outcome confirms our hypothesis that the primary difference between the methods lies in the introduction of the sliding-mode switching terms.

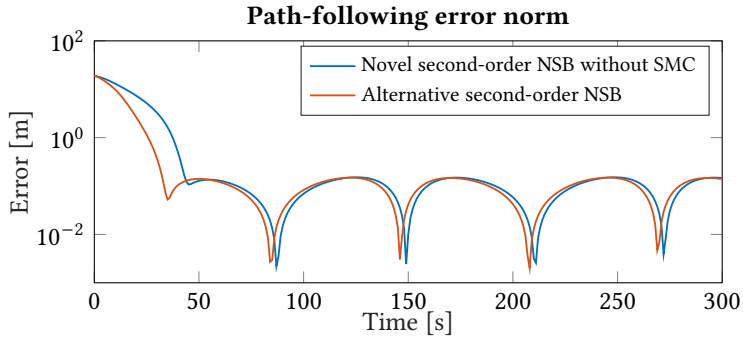

(a) Comparison of the path-following error.

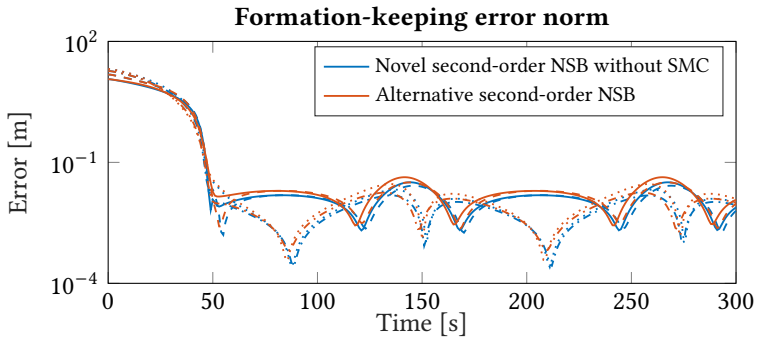

(b) Comparison of the formation-keeping error. The line styles represent different vehicles.

Figure 10.19: Comparison between the two different distributed formulations of the second-order NSB method where our novel formulation is stripped of all sliding-mode controller (SMC) terms.

Chapter 11

Conclusions and Future Work

In this thesis, we have addressed the formation path-following problem with AUVs and proposed a novel control method based on the extended second-order NSB algorithm. Our work makes several contributions to the field of autonomous fleet coordination and control. In particular, we have submitted a conference paper to the 62nd IEEE Conference on Decision and Control (Lie et al.; 2023).

Building upon the existing NSB algorithm, we developed an extended second-order NSB method that directly handles the double-integrator dynamics of AUVs. By leveraging the hand-position input-output linearizing controller, we express the entire fleet dynamics in task space resulting in a method without hidden low-level dynamics. The method enables us to express the task dynamics as interpretable spring-damper systems and eliminates the intermediate step of transforming desired velocities or accelerations into surge and orientation references, as has been done in previous works.

To validate the performance and stability of our control method, we conducted a thorough closed-loop stability analysis of the joint formation-control and path-following system. The formation-keeping subsystem was shown to be UGAS and the path-following subsystem was shown to be USGES.

One significant contribution of our research is the development of a novel approach to reformulating the centralized NSB algorithm into a decentralized method. By treat-

ing formation keeping as a consensus problem we devised a distributed NSB method that leverages inter-vehicle communication of path progress, relative positions, and relative velocities. Alternatively, with the right sensor set, the relative positions and velocities can be directly measured instead of communicated. This approach enables the application of the NSB method in real-world systems subject to communication constraints, as the need for continuous communication with a central node is eliminated.

Finally, extensive MATLAB simulation studies were conducted to evaluate the performance of both the centralized and decentralized NSB methods. Our simulations demonstrated the effectiveness of our approach and showcased that under ideal conditions it might perform better than existing methods. We evaluated the methods under various scenarios, including different choices for the external collision avoidance method. Although our method seemingly performed better than the first-order NSB method, we noted the advantages of the first-order method, in particular, that it leverages robust, well-tested low-level maneuvering controllers. The hand-position controller used in our method is not as well-tested and studied in real-world applications.

Future work includes testing the method on high-fidelity simulators such as Unified Navigation Environment (DUNE) (*DUNE: Unified Navigation Environment*; n.d.) and in real-world experiments. Testing the method's robustness in more realistic and complex underwater scenarios is a critical step before the method can be deployed in the real world. The use of high-fidelity simulators can provide a more accurate representation of the dynamics and environmental conditions that AUVs encounter in real-world operations. In particular, imperfect state measurements and actuation may significantly impact the underlying feedback-linearizing hand-position controller.

Initial attempts were made to implement the method in DUNE, but our efforts were not successful in robustly implementing the low-level hand-position controller. As the hand-position controller is a prerequisite for implementing the second-order NSB method, implementation in DUNE was not pursued further. Future work may therefore also include deeper research into the hand-position controller or alternative approaches to transforming the nonlinear equations of motion into double-integrator systems.

Appendix A

Internal boundedness coefficients

This appendix includes the coefficients from (7.31). The coefficients were calculated using the symbolic toolbox from MATLAB (2022).

$$a_y = \frac{d_{35}m_{55} - d_{55}m_{35} + hd_{33}m_{55} - hd_{53}m_{35}}{h(m_{33}m_{55} - m_{35}^2)}, \tag{A.1a}$$

$$a_z = \frac{d_{66}m_{26} - d_{26}m_{66} + hd_{22}m_{66} - hd_{62}m_{26}}{h(m_{22}m_{66} - m_{26}^2)}, \tag{A.1b}$$

$$\begin{aligned} a_{xyz} = &\frac{m_{35}m_{44} - m_{26}m_{55} - m_{35}m_{66} + hm_{26}m_{35} + hm_{22}m_{55}}{h(m_{33}m_{55} - m_{35}^2)} \\ &- \frac{m_{26}m_{55} - m_{26}m_{44} + m_{35}m_{66} + hm_{26}m_{35} + hm_{33}m_{66}}{h(m_{22}m_{66} - m_{26}^2)}, \end{aligned} \tag{A.1c}$$

$$a_{xy} = -\frac{m_{26}m_{35} + m_{22}m_{55}}{h(m_{33}m_{55} - m_{35}^2)}, \tag{A.1d}$$

$$a_{xz} = -\frac{m_{26}m_{35} + m_{33}m_{66}}{h(m_{22}m_{66} - m_{26}^2)}, \tag{A.1e}$$

$$a_{ye} = \frac{m_{11}m_{55} - m_{35}^2 + hm_{11}m_{35} - hm_{33}m_{35}}{h(m_{33}m_{55} - m_{35}^2)}, \tag{A.1f}$$

$$a_{ze} = \frac{m_{11}m_{66} - m_{26}^2 - hm_{11}m_{26} + hm_{22}m_{26}}{h(m_{22}m_{66} - m_{26}^2)}, \tag{A.1g}$$

$$a_{ey} = \frac{m_{11}m_{35} - m_{33}m_{35}}{h(m_{33}m_{55} - m_{35}^2)}, \tag{A.1h}$$

$$a_{ez} = \frac{m_{11}m_{26} - m_{22}m_{26}}{h(m_{22}m_{66} - m_{26}^2)}, \tag{A.1i}$$

$$a_{ley} = \frac{d_{53}m_{35} - d_{33}m_{55}}{h(m_{33}m_{55} - m_{35}^2)}, \tag{A.1j}$$

$$a_{lez} = \frac{d_{22}m_{66} - d_{62}m_{26}}{h(m_{22}m_{66} - m_{26}^2)}. \tag{A.1k}$$

Appendix B

Conference paper CDC 2023

This master's thesis is accompanied by a conference paper submitted to the Conference on Decision and Control 2023. The paper provides a concise presentation of the preliminary findings presented in this thesis, highlighting the most important results and conclusions for the centralized second-order NSB method. The paper is currently under review.

Formation Control of Underactuated AUVs Using the Hand Position Concept

Erling S. Lie, Josef Matouš, and Kristin Y. Pettersen

***Abstract*— This paper presents an extended null-space-based behavioral algorithm for the formation control of fleets of underactuated autonomous underwater vehicles. The null-space-based controller is developed to work directly with second-order integrator systems, handling the double integrator dynamics in task space. The method is applied to the problem of formation path-following of a fleet of underactuated autonomous underwater vehicles. The nonlinear six-degrees-of-freedom models of the vehicles are transformed into second-order integrator systems using a 3D hand position output linearizing controller. The behavioral controller implements a hierarchy of path-following, formation-keeping, and collision-avoidance tasks. The closed-loop system is proven uniformly globally asymptotically stable, and the proposed method is validated through numerical simulations.**

I. INTRODUCTION

Cooperating autonomous underwater vehicles (AUVs) has become an important area of research due to their potential for performing tasks that are difficult or impossible for a single AUV to accomplish. Cooperation among AUVs can increase mission efficiency, enable the exploration of larger areas, and provide redundancy in case of system failures.

In many applications, it is desirable for a fleet of AUVs to move in formation while following a desired path. Formation path-following can be achieved using a variety of control strategies. These include leader-follower approaches, where one AUV acts as a leader and the others follow its trajectory [1]–[3]. Coordinated path-following approaches use distributed control methods to achieve formation control, often based on consensus algorithms [4]–[6], while behavioral approaches focus on defining the behaviors each AUV should exhibit in order to achieve a desired formation [7], [8]. A comprehensive view of these strategies is provided in [9].

The null-space-based (NSB) behavioral approach is a popular centralized method for formation path-following that has been extensively studied in the literature [10]–[14]. This strategy enables complex missions through a hierarchy that combines several simpler tasks with strict priority. In [10], a comprehensive motivation is given for the decomposition of complex path-planning and coordination in multi-agent systems into two blocks: NSB and maneuvering. The NSB block takes into account the parameters of the mission, the environment, and the state of the fleet to calculate the desired velocities for each vehicle. The desired velocities are then tracked by the maneuvering controls.

The NSB algorithm, as presented in the existing literature, is developed for kinematic single-integrator systems [10]–[12]. In this work, we extend the NSB method to vehicles with double integrator dynamics and propose an algorithm that uses a second-order closed-loop inverse kinematics (SO-CLIK) equation to control the task variables through desired acceleration. The procedure is inspired by robotic manipulators, where second-order methods are more common, due to the inherent second-order dynamics of mechanical systems [15], [16]. Although existing NSB methods are developed for first-order systems, AUV dynamics are inherently second-order. Therefore, any first-order solution is necessarily perturbed by the dynamics of the maneuvering controller. In contrast, our formulation handles the second-order dynamics directly in the task space as interpretable spring-damper systems.

We apply the proposed NSB method to a fleet of AUVs. AUVs are underactuated systems with inherently nonlinear dynamics. What enables us to still use the proposed NSB method, developed for vehicles with linear double integrator dynamics, is the use of the hand position input-output linearization method, [17]–[20], for maneuvering control. Specifically, we apply the 3D hand position method proposed in [20], which transforms the underactuated six-degree-of-freedom AUV model into a double-integrator system. Subsequently, through the design of specific path-following, formation-keeping, and collision-avoidance tasks, the fleet is controlled to follow a preplanned path in formation while avoiding collisions both within the fleet and with external obstacles. The stability of the system is proved, and its effectiveness is verified in simulation. Because our reformulated NSB method works directly with the second-order system given by the hand position controller, there is no need to transform desired velocities or accelerations into surge and orientation references, as has been done in previous works. This reduces one level of complexity in the controller design.

The paper is organized as follows. Section II presents the extended NSB algorithm which is applicable for general double-integrator systems. Section III presents a case study of this NSB algorithm applied to a fleet of AUVs. Section IV presents conclusions and future work.

II. THE NSB ALGORITHM FOR DOUBLE INTEGRATORS

The NSB method enables the creation of multiple tasks in a hierarchical manner, ensuring that low-priority tasks do not interfere with high-priority ones. In this section, we present

This work was partly supported by the Research Council of Norway through project No. 302435 and the Centres of Excellence funding scheme, project No. 223254.

E. S. Lie, J. Matouš, and K. Y. Pettersen are with the Department of Engineering Cybernetics, Norwegian University of Science and Technology (NTNU), Trondheim, Norway. {erling.s.lie, josef.matous, kristin.y.pettersen}@ntnu.no

the method extended to second-order integrator systems. This modified NSB algorithm provides the acceleration input $\boldsymbol{\mu}$ to the following double-integrator system

$$\dot{\mathbf{p}} = \mathbf{v}, \tag{1a}$$
$$\dot{\mathbf{v}} = \boldsymbol{\mu}. \tag{1b}$$

For each task, we design a task variable $\boldsymbol{\sigma}_i \in \mathbb{R}_i^m$ as a function of $\mathbf{p}$

$$\boldsymbol{\sigma}_i = \mathbf{f}_i(\mathbf{p}). \tag{2}$$

The first and second time-derivatives of $\boldsymbol{\sigma}_i$ are

$$\dot{\boldsymbol{\sigma}}_i = \mathbf{J}_i(\mathbf{p})\mathbf{v}, \tag{3a}$$
$$\ddot{\boldsymbol{\sigma}}_i = \mathbf{J}_i(\mathbf{p})\dot{\mathbf{v}} + \dot{\mathbf{J}}_i\mathbf{v}, \tag{3b}$$

where $\mathbf{J}_i = \partial \mathbf{f}_i / \partial \mathbf{p}$ is the task Jacobian. We denote the desired value of the task variable by $\boldsymbol{\sigma}_{d,i}$.

In the standard NSB algorithm, $\mathbf{v}_i$ is obtained through the closed-loop inverse kinematics (CLIK) equation [21]

$$\mathbf{v}_i = \mathbf{J}_i^{\dagger}\big(\dot{\boldsymbol{\sigma}}_{d,i} - \boldsymbol{\Lambda}_i\tilde{\boldsymbol{\sigma}}_i\big), \tag{4}$$

where $\boldsymbol{\Lambda}_i$ is a positive definite gain matrix, $\tilde{\boldsymbol{\sigma}}_i = \boldsymbol{\sigma}_i - \boldsymbol{\sigma}_{d,i}$ is the task error, and $\mathbf{J}_i^{\dagger}$ is the pseudo-inverse of the task Jacobian. To achieve second-order differential control, we instead propose the second-order closed-loop inverse kinematics (SOCLIK) equation from robotic manipulators [22]

$$\dot{\mathbf{v}}_i = \mathbf{J}_i^{\dagger}\big(\ddot{\boldsymbol{\sigma}}_{d,i} - \boldsymbol{\Lambda}_{p,i}\tilde{\boldsymbol{\sigma}}_i - \boldsymbol{\Lambda}_{d,i}\dot{\tilde{\boldsymbol{\sigma}}}_i - \dot{\mathbf{J}}_i\mathbf{v}\big), \tag{5}$$

where $\boldsymbol{\Lambda}_{p,i}$ and $\boldsymbol{\Lambda}_{d,i}$ are positive definite gain matrices.

In the standard NSB algorithm, there exists a subspace of velocities that do not conflict with a given task. Similarly, in second-order systems, there exists a subspace of non-conflicting accelerations. If we denote $\dot{\mathbf{v}}_1$ as the SOCLIK solution to the highest priority task, there exists an acceleration $\dot{\mathbf{v}}_{NSB}$ that also satisfies this task:

$$\dot{\mathbf{v}}_{NSB} = \dot{\mathbf{v}}_1 + \mathbf{N}_1\dot{\mathbf{v}}_2, \tag{6}$$

where $\mathbf{N}_1 = \mathbb{I} - \mathbf{J}_1^{\dagger}\mathbf{J}_1$ is the null space projector of task 1, and $\dot{\mathbf{v}}_2$ is some additional desired acceleration resulting from other tasks. The relation can be generalized to obtain a solution for N tasks:

$$\dot{\mathbf{v}}_{NSB} = \sum_{i=1}^{N} \bar{\mathbf{N}}_i\dot{\mathbf{v}}_i, \tag{7}$$

where $\bar{\mathbf{N}}_i$ is the null space projector of the augmented Jacobian of all higher priority tasks $\bar{\mathbf{J}}_i = [\mathbf{J}_1^{\mathrm{T}} \dots \mathbf{J}_{i-1}^{\mathrm{T}}]^{\mathrm{T}}$. With this choice of acceleration, the highest priority task is always fulfilled, whereas the lower priority tasks are fulfilled as well as possible in the subspace that does not conflict with higher priority tasks. The commanded acceleration $\boldsymbol{\mu}$ is given by the NSB acceleration

$$\boldsymbol{\mu} = \dot{\mathbf{v}}_{NSB}. \tag{8}$$

A. Stability Analysis

In this section, we investigate the stability of an NSB algorithm consisting of two tasks. The proof is based on [23], but extended to a double integrator system. First, let us present the concepts of task independence and orthogonality.

Definition 1: Let $\mathbf{J}_1$ and $\mathbf{J}_2$ denote the Jacobians of tasks 1 and 2. These two tasks are *orthogonal* if

$$\mathbf{J}_1\mathbf{J}_2^{\dagger} = \mathbf{O}, \tag{9}$$

where $\mathbf{O}$ is a matrix of zeros. The tasks are *independent* if

$$\rho\left(\mathbf{J}_1^{\mathrm{T}}\right) + \rho\left(\mathbf{J}_2^{\mathrm{T}}\right) = \rho\left(\left[\mathbf{J}_1^{\mathrm{T}}\,\mathbf{J}_2^{\mathrm{T}}\right]\right), \tag{10}$$

where $\rho(\cdot)$ is the rank of the matrix.

Theorem 1: Consider two independent and orthogonal tasks 1 and 2. Let $\tilde{\mathbf{X}}^{\mathrm{T}} = \left[\tilde{\boldsymbol{\sigma}}_1^{\mathrm{T}}, \tilde{\boldsymbol{\sigma}}_2^{\mathrm{T}}, \dot{\tilde{\boldsymbol{\sigma}}}_1^{\mathrm{T}}, \dot{\tilde{\boldsymbol{\sigma}}}_2^{\mathrm{T}}\right]$ denote the stacked error vector.

The control input defined in (6) ensures that $\tilde{\mathbf{X}} = \mathbf{0}$ is a globally exponentially stable equilibrium point.

Proof: First, let us find the closed-loop expressions for $\ddot{\tilde{\boldsymbol{\sigma}}}_1$ and $\ddot{\tilde{\boldsymbol{\sigma}}}_2$, from (3b), (6), and (8):

$$\ddot{\tilde{\boldsymbol{\sigma}}}_1 = \mathbf{J}_1\dot{\mathbf{v}}_1 + \mathbf{J}_1\mathbf{N}_1\dot{\mathbf{v}}_2 + \dot{\mathbf{J}}_1\mathbf{v} - \ddot{\boldsymbol{\sigma}}_{d,1}, \tag{11a}$$
$$\ddot{\tilde{\boldsymbol{\sigma}}}_2 = \mathbf{J}_2\dot{\mathbf{v}}_1 + \mathbf{J}_2\mathbf{N}_1\dot{\mathbf{v}}_2 + \dot{\mathbf{J}}_2\mathbf{v} - \ddot{\boldsymbol{\sigma}}_{d,2}, \tag{11b}$$

Note that thanks to the independence and orthogonality assumptions, it follows that $\mathbf{J}_2\mathbf{N}_1\mathbf{J}_2^{\dagger} = \mathbb{I}$. Consequently, substituting (5) into (11) and using (3), the time-derivative of $\tilde{\mathbf{X}}$ is given by

$$\dot{\tilde{\mathbf{X}}} = \mathbf{M}\tilde{\mathbf{X}}, \tag{12}$$

where

$$\mathbf{M} = \begin{bmatrix} \mathbf{O} & \mathbf{O} & \mathbb{I} & \mathbf{O} \\ \mathbf{O} & \mathbf{O} & \mathbf{O} & \mathbb{I} \\ -\boldsymbol{\Lambda}_{p,1} & \mathbf{O} & -\boldsymbol{\Lambda}_{d,1} & \mathbf{O} \\ \mathbf{O} & -\boldsymbol{\Lambda}_{p,2} & \mathbf{O} & -\boldsymbol{\Lambda}_{d,2} \end{bmatrix}. \tag{13}$$

Since the gain matrices are positive definite by design, the matrix $\mathbf{M}$ is Hurwitz, and the closed-loop system is globally exponentially stable. ∎

III. Case Study: Formation Path Following of AUVs

The following sections present a case study of the proposed NSB algorithm applied to a fleet of underactuated AUVs equipped with the hand-position-based controller from [20]. The control objective of the fleet is to follow a predefined path while keeping formation and avoiding obstacles.

The vehicle model under the hand position controller is presented in Section III-A and the formation path following problem is formulated in Section III-B. The NSB tasks are detailed in Section III-C, Section III-D details the obstacle avoidance method, Section III-E analyzes the stability properites, and Section III-F presents a simulation study.

A. AUV model

We consider a 6-degree-of-freedom model of an AUV exposed to an unknown constant irrotational ocean current. The AUV's position, attitude, translational and rotational velocities are denoted by $\boldsymbol{\eta} \in \mathbb{R}^3$, $\mathbf{R} \in SO(3)$, $\boldsymbol{\nu} \in \mathbb{R}^3$, and $\boldsymbol{\omega} \in \mathbb{R}^3$, respectively. The relative velocity between the

AUV and current is $\boldsymbol{\nu}_r = \boldsymbol{\nu} - \mathbf{R}^{\mathrm{T}}\mathbf{v}_c$, and the concatenated velocity vector is $\boldsymbol{\zeta}_r^{\mathrm{T}} = [\boldsymbol{\nu}_r^{\mathrm{T}}, \boldsymbol{\omega}^{\mathrm{T}}]$.

We apply the 3D hand position-based controller from [20] for maneuvering control of the AUV and obtain the resulting system model

$$\dot{\mathbf{x}}_1 = \mathbf{x}_2 + \mathbf{v}_c, \tag{14a}$$

$$\dot{\mathbf{x}}_2 = \boldsymbol{\mu}, \tag{14b}$$

$$\dot{\mathbf{R}} = \mathbf{R}\mathbf{S}(\boldsymbol{\omega}), \tag{14c}$$

$$\begin{aligned}\dot{\boldsymbol{\omega}} = \bar{\mathbf{L}} \times \left(\mathbf{R}^{\mathrm{T}}\boldsymbol{\mu} + \mathcal{D}_{\boldsymbol{\nu}}(\boldsymbol{\zeta}_r) + \mathcal{C}_{\boldsymbol{\nu}}(\boldsymbol{\zeta}_r) - \boldsymbol{\omega} \times \mathbf{R}^{\mathrm{T}}\mathbf{x}_2\right) \\ - \left(\bar{\mathbf{L}}\mathbf{L}^{\mathrm{T}}\right)\left(\mathcal{D}_{\boldsymbol{\omega}}(\boldsymbol{\zeta}_r) + \mathbf{M}'_{22}(W\mathbf{z}_{gb}\mathbf{e}_3 \times \mathbf{R}^{\mathrm{T}}\mathbf{e}_3)\right).\end{aligned} \tag{14d}$$

Note that through the 3D hand position concept, the underactuated and highly nonlinear AUV model is now transformed to an input-output feedback linearized form, where the external part of the system $[\mathbf{x}_1, \mathbf{x}_2]^{\mathrm{T}}$ denotes the hand position and velocity given by

$$\mathbf{x}_1 = \boldsymbol{\eta} + \mathbf{R}\mathbf{L}, \tag{15a}$$

$$\mathbf{x}_2 = \mathbf{R}\boldsymbol{\nu}_r + \mathbf{R}(\boldsymbol{\omega} \times \mathbf{L}). \tag{15b}$$

The internal part of the system is given by $[\mathbf{R}, \boldsymbol{\omega}]^{\mathrm{T}}$, and $\boldsymbol{\mu}$ is the new control input. The definitions of the vectors and matrices $\mathbf{L}$, $\bar{\mathbf{L}}$, $\mathbf{M}'_{22}$, $\mathbf{z}_{gb}$, $\mathbf{e}_3$, $\mathcal{D}_{\boldsymbol{\nu}}$, $\mathcal{D}_{\boldsymbol{\omega}}$ and $\mathcal{C}_{\boldsymbol{\nu}}$ are given in [20].

B. Formation Path Following

We consider a fleet of n AUVs following a path in the inertial coordinate frame given by a smooth function $\mathbf{p}_p : \mathbb{R} \mapsto \mathbb{R}^3$, and define the stacked position and velocity vectors $\mathbf{p} = [\mathbf{x}_{1,1}^{\mathrm{T}}, \ldots, \mathbf{x}_{1,n}^{\mathrm{T}}]^{\mathrm{T}}$ and $\mathbf{v} = [\mathbf{x}_{2,1}^{\mathrm{T}}, \ldots, \mathbf{x}_{2,n}^{\mathrm{T}}]^{\mathrm{T}}$, respectively. We also define the stacked ocean current vector $\mathbf{V}_c = \mathbf{1}_{n,1} \otimes \mathbf{v}_c$, where $\mathbf{1}_{n,1}$ is an n-dimensional vector of ones, and $\otimes$ is the Kronecker product. We will in the following denote the position of a single AUV by $\mathbf{p}_i := \mathbf{x}_{1,i}$ and its velocity relative to the ocean current by $\mathbf{v}_i := \mathbf{x}_{2,i}$.

The path function is assumed to be $\mathcal{C}^\infty$ and regular, meaning that the function is continuously differentiable and the partial derivative with respect to ξ satisfies $\left\| \frac{\partial \mathbf{p}_p(\xi)}{\partial \xi} \right\| \neq 0$.

For every point $\mathbf{p}_p(\xi)$, there exists a path-tangential coordinate-frame with a corresponding rotation matrix $\mathbf{R}_p$ (see Fig. 1). The path-following error $\mathbf{p}_b^p$ is defined in terms of the barycenter of the fleet in the path-tangential coordinate frame:

$$\mathbf{p}_b^p = \mathbf{R}_p^{\mathrm{T}}\left(\mathbf{p}_b - \mathbf{p}_p(\xi)\right), \quad \mathbf{p}_b = \frac{1}{n}\sum_{i=1}^{n}\mathbf{p}_i. \tag{16}$$

The formation is defined in the formation-centered coordinate frame, centered at $\mathbf{p}_b$ with the same orientation as the path-tangential frame (see Fig. 2). The position in the formation-centered frame is given by

$$\mathbf{p}_i^f = \mathbf{R}_p^{\mathrm{T}}\left(\mathbf{p}_i - \mathbf{p}_b\right), \tag{17}$$

and the desired positions are given by $\mathbf{p}_{f,1}^f, \ldots, \mathbf{p}_{f,n}^f$.

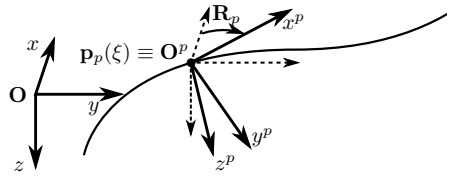

Fig. 1. Definition of the path angles and path-tangential coordinate frame. $\mathbf{O}$ denotes the origin of the inertial coordinate frame, $\mathbf{O}^p$ denotes the origin of the path-tangential frame.

C. NSB Controller

We let the control system consist of three tasks in decreasing order of priority: inter-vehicle collision avoidance, formation keeping, and path following. The following sections will detail the chosen task variables and SOCLIK solution for each task.

1) Inter-vehicle collision avoidance: The highest priority task is inter-vehicle collision avoidance (COLAV). This task is active only when two vehicles are closer than an activation distance d_{COLAV}. The task variable is given by a stacked vector $\boldsymbol{\sigma}_1 = [\sigma_{1,1}^{\mathrm{T}}, \ldots, \sigma_{1,l}^{\mathrm{T}}]^{\mathrm{T}}$ of relative distances between vehicles closer than the activation distance:

$$\begin{aligned}\sigma_{1,k} = \|\mathbf{p}_i - \mathbf{p}_j\|, \quad \forall i, j \in 1, \ldots, n : j > i, \\ \|\mathbf{p}_i - \mathbf{p}_j\| < d_{COLAV}.\end{aligned} \tag{18}$$

The task size varies depending on the number of vehicles that are within the activation distance, and it is empty under normal conditions. The desired values of the task are given by

$$\boldsymbol{\sigma}_{d,1} = d_{COLAV}\mathbf{1}_l. \tag{19}$$

We note that $\ddot{\boldsymbol{\sigma}}_{d,1} = \dot{\boldsymbol{\sigma}}_{d,1} = 0$.

The task Jacobian is given by the stacked partial derivatives for each active collision

$$\mathbf{J}_1 = \left[\left(\frac{\partial \sigma_{1,1}}{\partial \mathbf{p}}\right)^{\mathrm{T}}, \ldots, \left(\frac{\partial \sigma_{1,l}}{\partial \mathbf{p}}\right)^{\mathrm{T}}\right]^{\mathrm{T}}, \tag{20a}$$

$$\frac{\partial \sigma_{1,k}}{\partial \mathbf{p}_i} = \frac{(\mathbf{p}_i - \mathbf{p}_j)^{\mathrm{T}}}{\|\mathbf{p}_i - \mathbf{p}_j\|}, \quad \frac{\partial \sigma_{1,k}}{\partial \mathbf{p}_j} = -\frac{(\mathbf{p}_i - \mathbf{p}_j)^{\mathrm{T}}}{\|\mathbf{p}_i - \mathbf{p}_j\|}. \tag{20b}$$

The derivative of the task Jacobian is similarly given by a

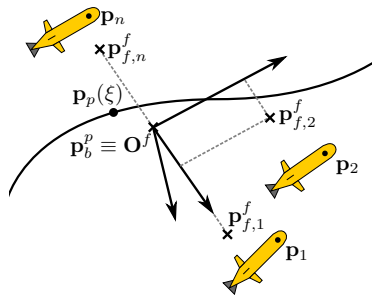

Fig. 2. Definition of the formation. $\mathbf{O}^f$ denotes the origin of the formation-centered coordinate frame.

stack of time-differentiated partial derivatives

$$\dot{\mathbf{J}}_1 = \left[\left(\frac{\mathrm{d}}{\mathrm{d}t}\frac{\partial\sigma_{1,1}}{\partial\mathbf{p}}\right)^{\mathrm{T}},\ldots,\left(\frac{\mathrm{d}}{\mathrm{d}t}\frac{\partial\sigma_{1,l}}{\partial\mathbf{p}}\right)^{\mathrm{T}}\right]^{\mathrm{T}}, \tag{21a}$$

$$\begin{aligned}\frac{\mathrm{d}}{\mathrm{d}t}\frac{\partial\sigma_{1,k}}{\partial\mathbf{p}_i} = \Bigg(&\frac{\mathbb{I}_3}{\|\mathbf{p}_i-\mathbf{p}_j\|}\\ &-\frac{(\mathbf{p}_i-\mathbf{p}_j)(\mathbf{p}_i-\mathbf{p}_j)^{\mathrm{T}}}{\|\mathbf{p}_i-\mathbf{p}_j\|^3}\Bigg)(\mathbf{v}_i-\mathbf{v}_j),\end{aligned} \tag{21b}$$

The resulting SOCLIK equation for the task is

$$\dot{\mathbf{v}}_1 = -\mathbf{J}_1^{\dagger}\big(\mathbf{\Lambda}_{p,1}\tilde{\boldsymbol{\sigma}}_1 + \mathbf{\Lambda}_{d,1}\dot{\boldsymbol{\sigma}}_1 + \dot{\mathbf{J}}_1(\mathbf{v}+\mathbf{V}_c)\big), \tag{22}$$

with $\dot{\boldsymbol{\sigma}}_1 = \mathbf{J}_1(\mathbf{v}+\mathbf{V}_c)$. Note that due to the structure of the task Jacobian, it follows that $\mathbf{J}_1\mathbf{V}_c = \dot{\mathbf{J}}_1\mathbf{V}_c = \mathbf{0}$. Consequently, $\dot{\mathbf{v}}_1$ is independent of the ocean current velocity.

2) Formation-Keeping Task: The formation-keeping task moves the vehicles into a predefined formation in the formation-centered frame. The task variable is given by

$$\boldsymbol{\sigma}_2 = \big[\boldsymbol{\sigma}_{2,1}^{\mathrm{T}},\ldots,\boldsymbol{\sigma}_{2,n-1}^{\mathrm{T}}\big]^{\mathrm{T}}, \quad \boldsymbol{\sigma}_{2,i} = \mathbf{p}_i - \mathbf{p}_b. \tag{23}$$

The desired values are

$$\boldsymbol{\sigma}_{d,2} = [\big(\mathbf{R}_p\mathbf{p}_{f,1}^f\big)^{\mathrm{T}},\ldots,\big(\mathbf{R}_p\mathbf{p}_{f,n-1}^f\big)^{\mathrm{T}}]^{\mathrm{T}}. \tag{24}$$

There is one fewer task than AUVs to avoid singularities, as the last AUV's position is implied by $\sum_{i=1}^{n}\mathbf{p}_{f,1}^f = \mathbf{0}$. The Jacobian is given by

$$\mathbf{J}_2 = \left(\begin{bmatrix}\mathbb{I}_{n-1} & \mathbf{0}_{n-1,1}\end{bmatrix} - \frac{\mathbf{1}_{n-1,n}}{N}\right)\otimes\mathbb{I}_3. \tag{25}$$

Because $\dot{\mathbf{J}}_2 = \mathbf{0}$, the SOCLIK equation reduces to

$$\dot{\mathbf{v}}_2 = \mathbf{J}_2^{\dagger}\big(\ddot{\boldsymbol{\sigma}}_{d,2} - \mathbf{\Lambda}_{p,2}\tilde{\boldsymbol{\sigma}}_2 - \mathbf{\Lambda}_{d,2}\dot{\tilde{\boldsymbol{\sigma}}}_2\big). \tag{26}$$

The nominal task acceleration (26) may saturate the actuators if the formation error is large. The NSB controller may also lead to a loss of controllability if the formation-keeping velocities exactly cancel out the path-following velocities. Therefore, we introduce the saturated task acceleration

$$\dot{\mathbf{v}}_2 = \mathbf{J}_2^{\dagger}\big(\ddot{\boldsymbol{\sigma}}_{d,2} - v_{2_{\max}}\mathrm{sat}\big(\mathbf{\Lambda}_{p,2}\tilde{\boldsymbol{\sigma}}_2\big) - \mathbf{\Lambda}_{d,2}\dot{\tilde{\boldsymbol{\sigma}}}_2\big), \tag{27}$$

where $v_{2_{\max}}$ is a positive constant and sat is a saturation function given by

$$\mathrm{sat}\big(\mathbf{x}\big) = \mathbf{x}\frac{\tanh\|\mathbf{x}\|}{\|\mathbf{x}\|}. \tag{28}$$

With the saturated task acceleration, we further require that the product of the gain matrices $\mathbf{\Lambda}_{p,2}\mathbf{\Lambda}_{d,2}$ is symmetric positive definite.

Like the inter-vehicle collision avoidance task, this task is independent of the ocean current.

3) Path Following Task: The path following task concerns moving the barycenter along the predefined path. Moreover, we want the formation to move at a constant, desired path-following speed U_{LOS}. We apply the same acceleration to all vehicles to ensure that the barycenter moves without changing the relative formation.

We apply the line-of-sight (LOS) algorithm from [12] and modify it to work with double-integrator systems. We denote the components of the path following error $\mathbf{p}_b^p$ as x_b^p, y_b^p, and z_b^p. Like in [12], we let $\Delta(\mathbf{p}_b^p)$ be the error-dependent look-ahead distance of the LOS guidance law given by

$$\Delta(\mathbf{p}_b^p) = \sqrt{\Delta_0^2 + (x_p^b)^2 + (y_p^b)^2 + (z_p^b)^2}, \tag{29}$$

where Δ_0 is a positive constant. The LOS velocity is then

$$\mathbf{v}_{LOS,d} = \mathbf{R}_p\left[\Delta(\mathbf{p}_b^p), -y_b^p, -z_b^p\right]^{\mathrm{T}}\frac{U_{LOS}}{D}, \tag{30}$$

where $U_{LOS} > 0$ is the desired path-following speed, and

$$D = \sqrt{\Delta(\cdot)^2 + (y_p^b)^2 + (z_p^b)^2} \tag{31}$$

is a normalization term.

Unlike [12], our method requires a desired acceleration. We derive the time-derivative of the line-of-sight velocity (30)

$$\begin{aligned}\dot{\mathbf{v}}_{LOS,d} = &\dot{\mathbf{R}}_p\left[\Delta(\mathbf{p}_b^p), -y_b^p, -z_b^p\right]^{\mathrm{T}}\frac{U_{LOS}}{D}\\ &+\mathbf{R}_p\left[\dot{\Delta}(\mathbf{p}_b^p,\dot{\mathbf{p}}_b^p), -\dot{y}_b^p, -\dot{z}_b^p\right]^{\mathrm{T}}\frac{U_{LOS}}{D}\\ &-\mathbf{R}_p\left[\Delta(\mathbf{p}_b^p), -y_b^p, -z_b^p\right]^{\mathrm{T}}\frac{U_{LOS}}{D^2}\dot{D}.\end{aligned} \tag{32}$$

We want to eliminate the error caused by the constant unknown ocean current at this stage of the control hierarchy, as all higher-priority tasks are independent of it. To this end, we introduce the virtual integral state $\mathbf{p}_v$ defined by

$$\dot{\mathbf{p}}_v = \mathbf{v}_{LOS,d}, \tag{33}$$

and define the following task acceleration

$$\dot{\mathbf{v}}_{LOS} = \dot{\mathbf{v}}_{LOS,d} + \mathbf{\Lambda}_{p,3}(\mathbf{v}_{LOS,d} - \mathbf{v}_b) + \mathbf{\Lambda}_{i,3}(\mathbf{p}_v - \mathbf{p}_b), \tag{34}$$

where $\mathbf{v}_b = \frac{1}{N}\sum_{i=1}^{N}\mathbf{v}_i$.

Lemma 1: Let $\mathbf{\Lambda}_{p,3}$ and $\mathbf{\Lambda}_{i,3}$ be two symmetric positive definite matrices. The relative barycenter velocity $\mathbf{v}_b$ converges exponentially to the relative LOS velocity $\mathbf{v}_{LOS,d} - \mathbf{v}_c$ under controller (7), (8) with the path-following task-acceleration given by (34).

Proof: We define error variables

$$\tilde{\mathbf{p}} = \mathbf{p}_b - \mathbf{p}_v - \mathbf{\Lambda}_{i,3}^{-1}\mathbf{\Lambda}_{p,3}\mathbf{v}_c, \tag{35a}$$

$$\tilde{\mathbf{v}} = \mathbf{v}_b + \mathbf{v}_c - \mathbf{v}_{LOS,d}, \tag{35b}$$

which have the following linear dynamics

$$\begin{bmatrix}\dot{\tilde{\mathbf{p}}}\\ \dot{\tilde{\mathbf{v}}}\end{bmatrix} = \begin{bmatrix}\mathbf{0} & \mathbb{I}\\ -\mathbf{\Lambda}_{i,3} & -\mathbf{\Lambda}_{p,3}\end{bmatrix}\begin{bmatrix}\tilde{\mathbf{p}}\\ \tilde{\mathbf{v}}\end{bmatrix}. \tag{36}$$

A linear system with a Hurwitz system matrix is uniformly globally exponentially stable. ∎

Since the desired acceleration is equal for all vehicles, we define it by a simple Kronecker product

$$\dot{\mathbf{v}}_3 = \mathbf{1}_{n,1}\otimes\dot{\mathbf{v}}_{LOS}. \tag{37}$$

Like in [12], the update of the path-parameter ξ is used as

an extra degree of freedom to guarantee along-track stability

$$\dot{\xi} = U_{LOS} \left\| \frac{\partial \mathbf{p}_p(\xi)}{\partial \xi} \right\|^{-1} \left(\frac{\Delta(\mathbf{p}_b^p)}{D} + k_\xi \frac{x_b^p}{\sqrt{1+(x_b^p)^2}} \right). \tag{38}$$

This choice ensures that the desired LOS velocity (30) guarantees USGES of the path-following task, which we will rely on in the stability proof presented in Section III-E.

D. Obstacle avoidance

We implement an obstacle avoidance method that enables the fleet to avoid external obstacles while keeping the formation. This approach mitigates the issue of vehicles straying out of communication range while evading obstacles. We modify the collision cones method from [12] to be compatible with double integrator dynamics and focus on obstacle avoidance in the xy-plane.

We assume a constant velocity model for the obstacle. Its position and velocity vectors are denoted by $\mathbf{p}_o = [x_o, y_o, z_o]^{\mathrm{T}}$ and $\mathbf{v}_o = [\dot{x}_o, \dot{y}_o, \dot{z}_o]^{\mathrm{T}}$. We define an obstacle avoidance radius r_o that is large enough to account for both the size of the obstacle and the AUV. The formation radius r_f is defined as the maximum distance between any vehicle in the fleet and the formation center, and it is assumed to be constant. We further define $\mathbf{p}_{rel} = [x_o - x_b, y_o - y_b]^{\mathrm{T}}$, $\mathbf{v}_{rel} = [\dot{x}_{LOS,d} - \dot{x}_o, \dot{y}_{LOS,d} - \dot{y}_o]^{\mathrm{T}}$, and $\dot{\mathbf{v}}_{rel} = [\ddot{x}_{LOS,d}, \ddot{y}_{LOS,d}]^{\mathrm{T}}$. Note that $\mathbf{v}_{rel}$ is defined in terms of the LOS desired velocity (30), so $\dot{\mathbf{p}}_{rel} \neq \mathbf{v}_{rel}$.

Collision is avoided if we ensure

$$||\mathbf{p}_{rel}|| \geq r_o + r_f \tag{39}$$

throughout the avoidance maneuver (see Fig. 3(a)). The formation is on a collision course (see Fig. 3(b)), if

$$|\angle(\mathbf{p}_{rel}, \mathbf{v}_{rel})| \leq \alpha, \quad \alpha = \sin^{-1}\Big(\frac{r_o + r_f}{||\mathbf{p}_{rel}||}\Big). \tag{40}$$

Then the obstacle avoidance task is activated if the fleet is close enough so that $\alpha > \alpha_{\min}$. When the task is active, the x- and y-components of $\mathbf{v}_{LOS,d}$ and $\dot{\mathbf{v}}_{LOS,d}$ given by (30) and (32) are replaced with $\mathbf{v}_{OA,d}$ and $\dot{\mathbf{v}}_{OA,d}$, given by

$$\mathbf{v}_{OA,d} = ||\mathbf{v}_{rel}|| \left[\cos(\psi_{OA}), \sin(\psi_{OA})\right]^{\mathrm{T}} + [\dot{x}_o, \dot{y}_o]^{\mathrm{T}}, \tag{41}$$

$$\dot{\mathbf{v}}_{OA,d} = ||\dot{\mathbf{v}}_{rel}|| \left[\cos(\psi_{OA}), \sin(\psi_{OA})\right]^{\mathrm{T}} + ||\mathbf{v}_{rel}|| \Big[-\sin(\psi_{OA})\dot{\psi}_{OA}, \cos(\psi_{OA})\dot{\psi}_{OA}\Big]^{\mathrm{T}}, \tag{42}$$

where

$$\psi_{OA} = \operatorname{atan_2}(y_o - y_b, x_o - x_b) \pm \alpha, \tag{43}$$

$$\dot{\psi}_{OA} = \frac{\det\big([\mathbf{p}_{rel}\ \dot{\mathbf{p}}_{rel}]\big)}{||\mathbf{p}_{rel}||^2} \pm \dot{\alpha}, \tag{44}$$

$$\dot{\alpha} = \frac{r_o + r_f}{||\mathbf{p}_{rel}||^2 \sqrt{||\mathbf{p}_{rel}||^2 - (r_o + r_f)^2}} \mathbf{p}_{rel}^{\mathrm{T}} \dot{\mathbf{p}}_{rel}, \tag{45}$$

before entering into (33) and (34).

E. Closed-Loop Analysis

In this section, we analyze the closed-loop stability of the system's external states and the boundedness of the internal states. We assume that the inter-vehicle collision avoidance task is inactive for the analysis. The path-following and formation-keeping tasks are orthogonal, because they produce common accelerations for the whole fleet and relative accelerations within the fleet, respectively. Therefore, the null-space projection $\mathbf{N}_2$ from the formation-keeping task will not affect the path-following acceleration $\mathbf{v}_3$

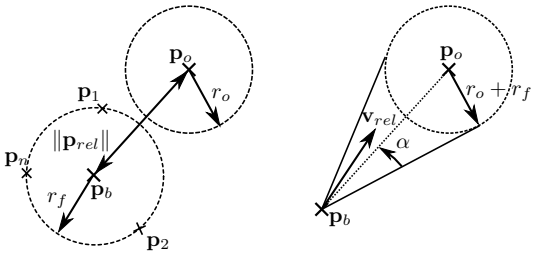

(a) Illustration of the obstacle avoidance constraint (39). (b) Illustration of the conflict condition (40).

Fig. 3. Illustrations of obstacle avoidance.

$$\dot{\mathbf{v}} = \dot{\mathbf{v}}_2 + \dot{\mathbf{v}}_3. \tag{46}$$

Furthermore, because of the following independence relations

$$\ddot{\boldsymbol{\sigma}}_2 = \mathbf{J}_2\dot{\mathbf{v}}_2 + \mathbf{J}_2\dot{\mathbf{v}}_3 = \mathbf{J}_2\dot{\mathbf{v}}_2, \tag{47}$$

$$\dot{\mathbf{v}}_b = \frac{1}{n}\sum_{i=1}^{n}(\dot{\mathbf{v}}_2 + \dot{\mathbf{v}}_3) = \frac{1}{n}\sum_{i=1}^{n}\dot{\mathbf{v}}_3, \tag{48}$$

the closed-loop properties of each task can be analyzed independently.

1) Stability of the Formation-Keeping Task: The closed-loop dynamics of the formation-task error $\tilde{\boldsymbol{\sigma}}_2$ under the saturated formation-keeping acceleration, (27), are given by the system

$$\ddot{\tilde{\boldsymbol{\sigma}}}_2 = -v_{2_{\max}}\mathrm{sat}\big(\boldsymbol{\Lambda}_{p,2}\tilde{\boldsymbol{\sigma}}_2\big) - \boldsymbol{\Lambda}_{d,2}\dot{\tilde{\boldsymbol{\sigma}}}_2. \tag{49}$$

Theorem 2: Let $\boldsymbol{\Lambda}_{p,2}$, $\boldsymbol{\Lambda}_{d,2}$ be two symmetric positive definite matrices so that the product $\boldsymbol{\Lambda}_{p,2}\boldsymbol{\Lambda}_{d,2}$ is symmetric positive definite. Then, $\big[\dot{\tilde{\boldsymbol{\sigma}}}_2^{\mathrm{T}}, \tilde{\boldsymbol{\sigma}}_2^{\mathrm{T}}\big]^{\mathrm{T}} = \mathbf{0}$ is a uniformly globally asymptotically stable (UGAS) equilibrium of the closed-loop system (49).

Proof: Consider the Lyapunov function

$$V(\tilde{\boldsymbol{\sigma}}_2, \dot{\tilde{\boldsymbol{\sigma}}}_2) = v_{2,\max}\log\left(\cosh\|\boldsymbol{\Lambda}_{p,2}\tilde{\boldsymbol{\sigma}}_2\|\right) + \frac{1}{2}\dot{\tilde{\boldsymbol{\sigma}}}_2^{\mathrm{T}}\boldsymbol{\Lambda}_{p,2}\dot{\tilde{\boldsymbol{\sigma}}}_2. \tag{50}$$

Inserting for (49), the time-derivative is given by

$$\begin{aligned}\dot{V} &= v_{2,\max}\mathrm{sat}\left(\boldsymbol{\Lambda}_{p,2}\tilde{\boldsymbol{\sigma}}_2\right)^{\mathrm{T}}\boldsymbol{\Lambda}_{p,2}\dot{\tilde{\boldsymbol{\sigma}}}_2 \\ &\quad - \dot{\tilde{\boldsymbol{\sigma}}}_2^{\mathrm{T}}\boldsymbol{\Lambda}_{p,2}\left(v_{2,\max}\mathrm{sat}\left(\boldsymbol{\Lambda}_{p,2}\tilde{\boldsymbol{\sigma}}_2\right) + \boldsymbol{\Lambda}_{d,2}\dot{\tilde{\boldsymbol{\sigma}}}_2\right), \\ &= -\dot{\tilde{\boldsymbol{\sigma}}}_2^{\mathrm{T}}\boldsymbol{\Lambda}_{p,2}\boldsymbol{\Lambda}_{d,2}\dot{\tilde{\boldsymbol{\sigma}}}_2.\end{aligned} \tag{51}$$

Let $S = \{\big[\dot{\tilde{\boldsymbol{\sigma}}}_2^{\mathrm{T}}, \tilde{\boldsymbol{\sigma}}_2^{\mathrm{T}}\big]^{\mathrm{T}} \in \mathbb{R}^{6(n-1)} | \dot{V} = 0\}$. Because of the dynamics (49), no other solution can stay identically in S,

other than the trivial solution $\left[\dot{\tilde{\boldsymbol{\sigma}}}_2^{\mathrm{T}}, \tilde{\boldsymbol{\sigma}}_2^{\mathrm{T}}\right]^{\mathrm{T}} \equiv \mathbf{0}$. Thus, the origin is globally asymptotically stable according to [24, Corollary 4.2]. Furthermore, because (49) is time-invariant, the equilibrium is UGAS. ■

2) Stability of the Path-Following Task: Let $\tilde{\mathbf{p}}$ and $\tilde{\mathbf{v}}$ be given by (35). Using the definition

$$\mathbf{p}_b^p = \mathbf{R}_p^{\mathrm{T}}(\mathbf{p}_b - \mathbf{p}_p), \tag{52}$$

we get the following error system

$$\begin{aligned}
\dot{\tilde{\mathbf{p}}} &= \tilde{\mathbf{v}}, \\
\dot{\tilde{\mathbf{v}}} &= -\boldsymbol{\Lambda}_{p,3}\tilde{\mathbf{v}} - \boldsymbol{\Lambda}_{i,3}\tilde{\mathbf{p}}, \qquad (53a)\\
\dot{\mathbf{p}}_b^p &= f(\cdot) + g(\cdot)\tilde{\mathbf{v}}, \\
&= \mathbf{R}_p^{\mathrm{T}}(\mathbf{v}_b + \mathbf{v}_c - \dot{\mathbf{p}}_p) + \left(\mathbf{S}(\omega_p\dot{\xi})\right)^{\mathrm{T}}\mathbf{R}_p^{\mathrm{T}}(\mathbf{p}_b - \mathbf{p}_p), \qquad (53b)\\
&= \mathbf{R}_p^{\mathrm{T}}(\mathbf{v}_{LOS,d} - \dot{\mathbf{p}}_p) - \mathbf{S}(\omega_p\dot{\xi})\mathbf{p}_b^p + \mathbf{R}_p^{\mathrm{T}}\tilde{\mathbf{v}}.
\end{aligned}$$

Theorem 3: Let $\boldsymbol{\Lambda}_{p,3}$, $\boldsymbol{\Lambda}_{i,3}$ be positive definite matrices. Then, $[\tilde{\mathbf{p}}^{\mathrm{T}}, \tilde{\mathbf{v}}^{\mathrm{T}}, (\mathbf{p}_b^p)^{\mathrm{T}}]^{\mathrm{T}} = \mathbf{0}$ is a uniformly semiglobally exponentially stable equilibrium (USGES) of the system (53a)-(53b).

Proof: Note that the error system is in a cascaded form where the velocity error $\tilde{\mathbf{v}}$ from (53a) perturbs the system (53b). The dynamics of the perturbing system (53a) are UGES according to Lemma 1. The nominal system (53b) with $\tilde{\mathbf{v}} = \mathbf{0}$ was proved to be USGES in [12] using the Lyapunov function

$$V(\mathbf{p}_b^p) = \frac{1}{2}\left(\mathbf{p}_b^p\right)^{\mathrm{T}}\mathbf{p}_b^p. \tag{54}$$

Therefore, according to [25, Proposition 9] the cascaded system is USGES if the following two assumptions hold

1) There exist constants c_1, c_2, $\eta > 0$ such that

$$\left\|\frac{\partial V}{\partial \mathbf{p}_b^p}\right\| \|\mathbf{p}_b^p\| \le c_1 V(\mathbf{p}_b^p), \quad \forall \|\mathbf{p}_b^p\| \ge \eta, \tag{55}$$

$$\left\|\frac{\partial V}{\partial \mathbf{p}_b^p}\right\| \le c_2, \quad \forall \|\mathbf{p}_b^p\| \le \eta. \tag{56}$$

2) There exist two continuous functions α_1, $\alpha_2 : \mathbb{R}_{\ge 0} \to \mathbb{R}_{\ge 0}$, such that $\mathbf{g}(\cdot)$ satisfies

$$\|g(\cdot)\| \le \alpha_1(\|\tilde{\mathbf{v}}\|) + \alpha_2(\|\tilde{\mathbf{v}}\|)\|\mathbf{p}_b^p\|. \tag{57}$$

Because $\|\partial V/\partial \mathbf{p}_b^p\| = \|\mathbf{p}_b^p\|$, 1) holds with $c_1 = 2$, $c_2 = \eta$ for any $\eta \in \mathbb{R}_{\ge 0}$.

Equation (57) is satisfied with $\alpha_1(\|\tilde{\mathbf{v}}\|) = 1, \alpha_2(\|\tilde{\mathbf{v}}\|) = 0$, because $\|g(\cdot)\| = \|\mathbf{R}_p^{\mathrm{T}}\| = 1$. As a result, all assumptions of [25, Proposition 9] are satisfied, and the origin of the closed-loop path-following system (53a)-(53b) is USGES. ■

3) Boundedness of Internal States: The proofs in this section are based on [20]. For brevity, we will omit those derivations that can be directly found in [20].

We note that the only states that can grow unboundedly are the angular velocities of the vehicles. Let p_i, q_i, and r_i denote the roll, pitch, and yaw rate of vehicle i (note that $\boldsymbol{\omega}_i^{\mathrm{T}} = [p_i, q_i, r_i]$). Furthermore, let $\mathbf{p}_{\mathrm{d},i} = \mathbf{p}_p(\xi) + \mathbf{R}_p\mathbf{p}_{f,i}^f$ denote the desired position of vehicle i. Note that because the path function is $\mathcal{C}_\infty$ and thanks to the choice of the path parameter update law (38), the time-derivative of $\mathbf{p}_{\mathrm{d},i}$ is bounded.

First, we investigate the roll rate dynamics. In [20], it is shown that the roll rate dynamics are always bounded. Specifically, there exist $a_x, b_x > 0$ such that

$$|p_i(t)| \le |p_i(0)|\,\mathrm{e}^{-a_x t} + \frac{b_x}{a_x}\left(1 - \mathrm{e}^{-a_x t}\right). \tag{58}$$

Now, we investigate the pitch and yaw rate dynamics. The closed-loop expression for $\dot{q}_i$ and $\dot{r}_i$ is

$$\begin{aligned}
\begin{bmatrix}\dot{q}_i \\ \dot{r}_i\end{bmatrix} = \begin{bmatrix}0 & 0 & -\frac{1}{h} \\ 0 & \frac{1}{h} & 0\end{bmatrix}\Big(&\mathbf{R}_i^{\mathrm{T}}\boldsymbol{\mu}_i + \mathcal{D}_\nu(\boldsymbol{\zeta}_{r,i}) + \mathcal{C}_\nu(\boldsymbol{\zeta}_{r,i}) \qquad (59)\\
&- \boldsymbol{\omega}_i \times \mathbf{R}_i^{\mathrm{T}}\mathbf{x}_{2,i}\Big).
\end{aligned}$$

Note that under the NSB control law, the hand velocity $\mathbf{x}_{2,i}$ converges to $\dot{\mathbf{p}}_{\mathrm{d},i} - \mathbf{v}_c$. Consider then the following Lyapunov function candidate

$$V_{\omega_i}(q_i, r_i) = \frac{1}{2}\left(q_i^2 + r_i^2\right). \tag{60}$$

In [20], it is shown that the following inequality holds for the time-derivative of V_{ω_i}

$$\begin{aligned}
\dot{V}_{\omega_i} \le &- a_y q_i^2 - a_z r_i^2 + \|\mathbf{x}_{2,i}\|\,\|[q_i, r_i]\|\left(\frac{\|\boldsymbol{\omega}_i\|}{h} + a_e\right) \\
&+ a_{xyz}p_i q_i r_i + a_{xy}\|\mathbf{x}_{2,i}\|\,p_i q_i + a_{xz}\|\mathbf{x}_{2,i}\|\,p_i r_i \\
&+ a_{ye}\|\mathbf{x}_{2,i}\|\,q_i^2 + a_{ze}\|\mathbf{x}_{2,i}\|\,r_i^2 + a_{ey}\|\mathbf{x}_{2,i}\|^2 q_i \\
&+ a_{ez}\|\mathbf{x}_{2,i}\|^2 q_i + \|[q_i, r_i]\|\,\|\boldsymbol{\mu}_i\|. \qquad (61)
\end{aligned}$$

Theorem 4: Let us define

$$\bar{p} = b_x/a_x, \qquad \bar{\mathbf{x}}_2 = \max_{t\in\mathbb{R}_{\ge 0}} \|\dot{\mathbf{p}}_{\mathrm{d},i}(t) - \mathbf{v}_c\|, \tag{62a}$$

$$\bar{\alpha}_y = a_y - \left(\frac{1}{h}\bar{\mathbf{x}}_2 + \frac{1}{2}\left|a_{xyz}\bar{p}\right| + \left|a_{ye}\bar{\mathbf{x}}_2\right|\right), \tag{62b}$$

$$\bar{\alpha}_z = a_z - \left(\frac{1}{h}\bar{\mathbf{x}}_2 + \frac{1}{2}\left|a_{xyz}\bar{p}\right| + \left|a_{ze}\bar{\mathbf{x}}_2\right|\right). \tag{62c}$$

The angular rate dynamics are ultimately bounded if $a_x, \bar{\alpha}_y, \bar{\alpha}_z > 0$.

Proof: Using the identities described in [20], we can derive the following (looser) upper bound on $\dot{V}_{\omega_i}$

$$\dot{V}_{\omega_i} \le -\alpha_y q_i^2 - \alpha_z r_i^2 + G\left(\mathbf{x}_{2,i}, \boldsymbol{\omega}_i, \boldsymbol{\mu}_i\right), \tag{63}$$

where

$$\alpha_y = \left(a_y - \left(\frac{1}{h}\|\mathbf{x}_2\| + \frac{1}{2}\left|a_{xyz}\right|\left|p_i\right| + \left|a_{ye}\right|\|\mathbf{x}_2\|\right)\right), \tag{64a}$$

$$\alpha_z = \left(a_z - \left(\frac{1}{h}\|\mathbf{x}_2\| + \frac{1}{2}\left|a_{xyz}\right|\left|p_i\right| + \left|a_{ze}\right|\|\mathbf{x}_2\|\right)\right), \tag{64b}$$

and $G(\cdot)$ represents the terms that grow at most linearly with q_i and r_i. Note that the two following limits

$$\lim_{t\to\infty}\alpha_y \ge \bar{\alpha}_y, \qquad \lim_{t\to\infty}\alpha_z \ge \bar{\alpha}_z, \tag{65}$$

hold for α_y and α_z. Therefore, if $\bar{\alpha}_y, \bar{\alpha}_z > 0$, then there exists a finite time T after which $\alpha_y, \alpha_z > 0$.

First, let us investigate the candidate Lyapunov function

for $t < T$. Since α_y and α_z may be negative, we cannot prove boundedness. However, note that the derivative of the Lyapunov function in (63) has the following form

$$\dot{V}_{\omega_i} \leq k \left\| \widehat{\omega}_i \right\|^2 + G(\cdot), \tag{66}$$

where $\widehat{\omega}_i := [q_i,\, r_i]^{\mathrm{T}}$, k is a positive constant and $G(\cdot)$ grows at most linearly with $\|\widehat{\omega}_i\|$. We can therefore conclude that the dynamics of q_i and r_i are forward complete [26].

For $t \geq T$, $\dot{V}_{\omega_i}$ has the following form

$$\dot{V}_{\omega_i} \leq -\alpha_y q_i^2 - \alpha_z r_i^2 + G(\cdot) \tag{67}$$

For sufficiently large angular velocities, the quadratic term will dominate the linear term $G(\cdot)$, and q and r will remain bounded.

The angular rate dynamics are thus ultimately bounded. ■

F. Simulation results

To validate the theoretical results, we perform a simulation where the proposed algorithm is applied to a fleet of three LAUVs [27]. In the simulated scenario, the vehicles should follow a continuous, differentiable spiral while avoiding collision with a stationary cylindrical-shaped obstacle with radius $10\,\mathrm{m}$, base circle in the xy-plane and origin $[x, y] = [100, -10]$. All position variables are here given in meters. The spiral is given by

$$\mathbf{p}_p(\xi) = \mathbf{p}_{p,0} + \left[\xi, -40\cos(\tfrac{\pi}{100}\xi), 20\sin(\tfrac{\pi}{100}\xi)\right]^{\mathrm{T}}, \tag{68}$$

where

$$\mathbf{p}_{p,0} = \left[0, -40, 35\right]^{\mathrm{T}}. \tag{69}$$

The barycenter relative formation is given by

$$\mathbf{p}_{f,1}^f = \begin{bmatrix} 0 \\ 10 \\ 5 \end{bmatrix}, \quad \mathbf{p}_{f,1}^f = \begin{bmatrix} 0 \\ -10 \\ 5 \end{bmatrix}, \quad \mathbf{p}_{f,1}^f = \begin{bmatrix} 0 \\ 0 \\ -10 \end{bmatrix}, \tag{70}$$

and we want the collision avoidance task to ensure a safe distance of $10\,\mathrm{m}$ both between vehicles in the fleet and external obstacles. Therefore, the avoidance radius of the cylinder, $\mathbf{r}_o$, is $20\,\mathrm{m}$. The vehicles are subject to an unknown ocean current

$$\mathbf{v}_c = \begin{bmatrix} 0 & 0.25 & 0.05 \end{bmatrix}^{\mathrm{T}}\ \mathrm{m/s}. \tag{71}$$

We initialize the fleet with barycenter $\mathbf{p}_b = [-5, -100, 18]^{\mathrm{T}}$ and relative positions

$$\boldsymbol{\sigma}_{2,1} = \begin{bmatrix} 0 \\ -15 \\ -7 \end{bmatrix}, \quad \boldsymbol{\sigma}_{2,2} = \begin{bmatrix} 0 \\ 15 \\ -7 \end{bmatrix}, \quad \boldsymbol{\sigma}_{2,3} = \begin{bmatrix} 0 \\ 0 \\ 14 \end{bmatrix}. \tag{72}$$

The resulting North-East trajectory of the mission is shown in Figure 5. The vehicles avoid the obstacle with a margin and return to the desired path. Figure 4(a) shows that the angular velocities remain bounded, in accordance with Theorem 4. Figure 4(b) shows that the fleet converges to the desired formation while the obstacle avoidance mode is active. Except for during the inter-vehicle collision avoidance, the convergence seems linear, which can be expected because the task velocity is saturated by $v_{2,\max}$. Figure 4(c) shows that the inter-vehicle COLAV task activates when the distance between vehicles is below d_{COLAV}, and the distance does not decrease further. Because the obstacle avoidance radius r_o was chosen $10\mathrm{m}$ wider than the obstacle, the obstacle is avoided with a $10\mathrm{m}$ margin. Figure 4(d) shows that the path-following error initially increases as the fleet avoids the obstacle because the x- and y-components of $\mathbf{v}_{LOS,d}$ and $\dot{\mathbf{v}}_{LOS,d}$ are replaced with $\mathbf{v}_{OA,d}$ and $\dot{\mathbf{v}}_{OA,d}$ given by (41), (42). As expected from Theorem 3, the error converges to zero after the obstacle is passed when the LOS task is activated again.

IV. Conclusions and future work

In this paper, we proposed an extended NSB method for double-integrator systems. The method was proved to provide GES task error dynamics. The method was demonstrated in a case study of formation path-following with underactuated AUVs. We defined the second-order kinematic tasks for collision avoidance, formation-keeping, and path-following. To force a bounded velocity, we introduced a saturation term to the formation-keeping acceleration. The closed-loop formation-error system with the reformulated formation-keeping acceleration was proved to be UGAS. The closed-loop path-following system was proved to be USGES. Simulation results demonstrate the effectiveness of our approach. Possible future work includes verifying the presented results through experiments.

References

[1] M. Soorki, H. Talebi, and S. Nikravesh, "A robust dynamic leader-follower formation control with active obstacle avoidance," in *Proc. 2011 IEEE International Conference on Systems, Man, and Cybernetics*, Oct. 2011, pp. 1932–1937.

[2] R. Cui, S. Sam Ge, B. Voon Ee How, and Y. Sang Choo, "Leader–follower formation control of underactuated autonomous underwater vehicles," *Ocean Engineering*, vol. 37, no. 17, pp. 1491–1502, Dec. 2010.

[3] Y. Wang, W. Yan, and W. Yan, "A leader-follower formation control strategy for AUVs based on line-of-sight guidance," in *Proc. 2009 International Conference on Mechatronics and Automation*, Aug. 2009, pp. 4863–4867.

[4] R. Skjetne, S. Moi, and T. Fossen, "Nonlinear formation control of marine craft," in *Proc. 41st IEEE Conference on Decision and Control, 2002.*, Dec. 2002, pp. 1699–1704.

[5] R. Ghabcheloo, A. P. Aguiar, A. Pascoal, C. Silvestre, I. Kaminer, and J. Hespanha, "Coordinated path-following control of multiple underactuated autonomous vehicles in the presence of communication failures," in *Proc. 45th IEEE Conference on Decision and Control*, Dec. 2006, pp. 4345–4350.

[6] E. Borhaug and K. Y. Pettersen, "Formation Control of 6-DOF Euler-Lagrange Systems with Restricted Inter-Vehicle Communication," in *Proc. 45th IEEE Conference on Decision and Control*, Dec. 2006, pp. 5718–5723.

[7] S. Monteiro and E. Bicho, "A dynamical systems approach to behavior-based formation control," in *Proc. 2002 IEEE International Conference on Robotics and Automation*, May 2002, pp. 2606–2611.

[8] T. Balch and R. Arkin, "Behavior-based formation control for multi-robot teams," *IEEE Transactions on Robotics and Automation*, vol. 14, no. 6, pp. 926–939, Dec. 1998.

[9] B. Das, B. Subudhi, and B. B. Pati, "Cooperative formation control of autonomous underwater vehicles: An overview," *International Journal of Automation and Computing*, vol. 13, no. 3, pp. 199–225, Jun. 2016.

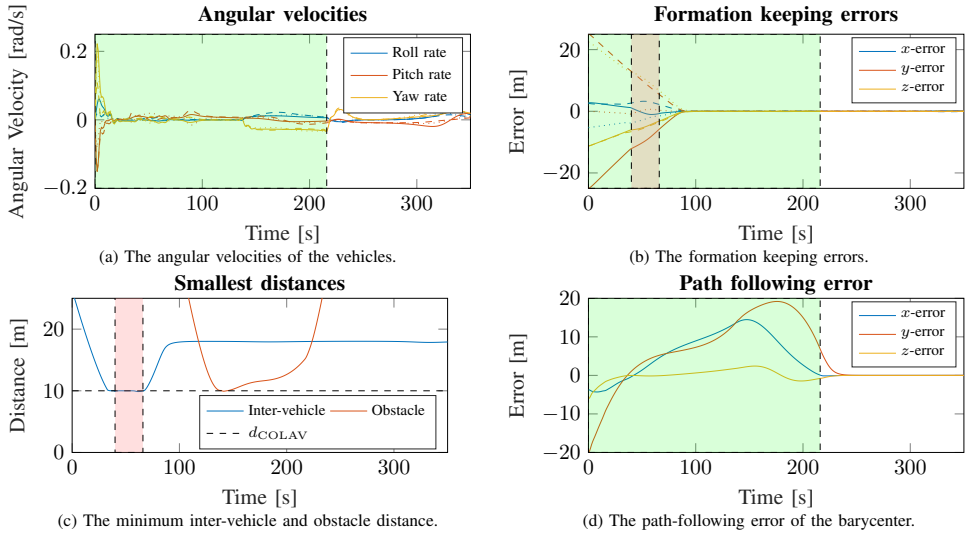

(a) The angular velocities of the vehicles.

(b) The formation keeping errors.

(c) The minimum inter-vehicle and obstacle distance.

(d) The path-following error of the barycenter.

Fig. 4. Simulation results of the path-following algorithm proposed in Section III. The full, dashed, and dotted lines correspond to the three different vehicles. The green and red rectangles represent when obstacle avoidance and inter-vehicle COLAV is active.

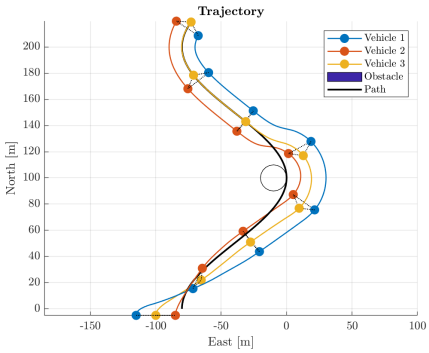

Fig. 5. The trajectory of the vehicles. The markers represent the vehicle positions every 50 seconds.

[10] F. Arrichiello, S. Chiaverini, and T. I. Fossen, "Formation Control of Underactuated Surface Vessels using the Null-Space-Based Behavioral Control," in *Proc. 2006 IEEE/RSJ International Conference on Intelligent Robots and Systems*, Oct. 2006, pp. 5942–5947.

[11] Å. Eek, K. Y. Pettersen, E.-L. M. Ruud, and T. R. Krogstad, "Formation path following control of underactuated USVs," *European Journal of Control*, vol. 62, pp. 171–184, Nov. 2021.

[12] J. Matouš, K. Y. Pettersen, D. Varagnolo, and C. Paliotta, "Singularity-free Formation Path Following of Underactuated AUVs: Extended Version," arXiv:2210.14646 [cs, eess], *To appear in Proc. 22nd IFAC World Congress, July 2023.*

[13] F. Arrichiello, H. Heidarsson, S. Chiaverini, and G. S. Sukhatme, "Cooperative caging using autonomous aquatic surface vehicles," in *Proc. 2010 IEEE International Conference on Robotics and Automation*, May 2010, pp. 4763–4769.

[14] F. J. Pereda, H. G. de Marina, J. M. Giron-Sierra, and J. Jimenez, "Towards automatic oil spill confinement with Autonomous Marine Surface Vehicles," in *OCEANS 2011 IEEE - Spain*, Jun. 2011.

[15] B. Siciliano, L. Sciavicco, L. Villani, and G. Oriolo, "Differential Kinematics and Statics," in *Robotics: Modelling, Planning and Control*, ser. Advanced Textbooks in Control and Signal Processing. London: Springer, 2009, pp. 105–160.

[16] S. Chiaverini, G. Oriolo, and I. D. Walker, "Kinematically Redundant Manipulators," in *Springer Handbook of Robotics*, B. Siciliano and O. Khatib, Eds. Berlin, Heidelberg: Springer, 2008, pp. 245–268.

[17] E. Restrepo, J. Matouš, and K. Y. Pettersen, "Tracking-in-Formation of Multiple Autonomous Marine Vehicles under Proximity and Collision-Avoidance Constraints," in *Proc. 2022 European Control Conference*, Jul. 2022, pp. 930–937.

[18] X. Cai and M. d. Queiroz, "Adaptive Rigidity-Based Formation Control for Multirobotic Vehicles With Dynamics," *IEEE Transactions on Control Systems Technology*, vol. 23, no. 1, pp. 389–396, Jan. 2015.

[19] C. Paliotta, E. Lefeber, K. Y. Pettersen, J. Pinto, M. Costa, and J. T. de Figueiredo Borges de Sousa, "Trajectory Tracking and Path Following for Underactuated Marine Vehicles," *IEEE Transactions on Control Systems Technology*, vol. 27, no. 4, pp. 1423–1437, Jul. 2019.

[20] J. Matouš, C. Paliotta, K. Y. Pettersen, and D. Varagnolo, "Trajectory tracking and path following of underactuated AUVs using the hand position concept," *Submitted to IEEE Transactions on Control Systems Technology*, 2023, preprint available at https://www.dropbox.com/s/pwyople7rpykge9/SubmittedVersion.pdf?dl=0.

[21] G. Antonelli and S. Chiaverini, "Kinematic Control of Platoons of Autonomous Vehicles," *IEEE Transactions on Robotics*, vol. 22, no. 6, pp. 1285–1292, Dec. 2006.

[22] B. Siciliano, "A closed-loop inverse kinematic scheme for on-line joint-based robot control," *Robotica*, vol. 8, no. 3, p. 231–243, 1990.

[23] G. Antonelli, F. Arrichiello, and S. Chiaverini, "Stability analysis for the null-space-based behavioral control for multi-robot systems," in *Proc. 47th IEEE Conference on Decision and Control*, 2008, pp. 2463–2468.

[24] H. K. Khalil, *Nonlinear Systems*. Prentice Hall, 2002.

[25] K. Y. Pettersen, "Lyapunov sufficient conditions for uniform semiglobal exponential stability," *Automatica*, vol. 78, pp. 97–102, Apr. 2017.

[26] D. Angeli and E. D. Sontag, "Forward completeness, unboundedness observability, and their Lyapunov characterizations," *Systems & Control Letters*, vol. 38, no. 4, pp. 209–217, Dec. 1999.

[27] A. Sousa, L. Madureira, J. Coelho, J. Pinto, J. Pereira, J. Borges Sousa, and P. Dias, "LAUV: The Man-Portable Autonomous Underwater Vehicle," *IFAC Proceedings Volumes*, vol. 45, no. 5, pp. 268–274, Jan. 2012.

References

Aguiar, A. and Pascoal, A. (2002). Dynamic positioning and way-point tracking of underactuated AUVs in the presence of ocean currents, *Proc. 41st IEEE Conference on Decision and Control*, pp. 2105–2110 vol.2.

Angeli, D. and Sontag, E. D. (1999). Forward completeness, unboundedness observability, and their Lyapunov characterizations, *Systems & Control Letters* **38**(4): 209–217.

Antonelli, G., Arrichiello, F. and Chiaverini, S. (2008). Stability analysis for the null-space-based behavioral control for multi-robot systems, *Proc. 47th IEEE Conference on Decision and Control*, pp. 2463–2468.

Antonelli, G. and Chiaverini, S. (2006). Kinematic Control of Platoons of Autonomous Vehicles, *IEEE Transactions on Robotics* **22**(6): 1285–1292.

Arrichiello, F., Chiaverini, S. and Fossen, T. I. (2006). Formation Control of Underactuated Surface Vessels using the Null-Space-Based Behavioral Control, *Proc. 2006 IEEE/RSJ International Conference on Intelligent Robots and Systems*, pp. 5942–5947.

Arrichiello, F., Heidarsson, H., Chiaverini, S. and Sukhatme, G. S. (2010). Cooperative caging using autonomous aquatic surface vehicles, *Proc. 2010 IEEE International Conference on Robotics and Automation*, pp. 4763–4769.

Balch, T. and Arkin, R. (1998). Behavior-based formation control for multirobot teams, *IEEE Transactions on Robotics and Automation* **14**(6): 926–939.

Belleter, D., Maghenem, M. A., Paliotta, C. and Pettersen, K. Y. (2019). Observer based path following for underactuated marine vessels in the presence of ocean currents: A global approach, *Automatica* **100**: 123–134.

Borhaug, E., Pavlov, A. and Pettersen, K. Y. (2007). Straight line path following for formations of underactuated underwater vehicles, *Proc. 46th IEEE Conference on Decision and Control*, pp. 2905–2912.

Borhaug, E. and Pettersen, K. Y. (2006). Formation Control of 6-DOF Euler-Lagrange Systems with Restricted Inter-Vehicle Communication, *Proc. 45th IEEE Conference on Decision and Control*, pp. 5718–5723.

Breivik, M. and Fossen, T. (2005). Principles of Guidance-Based Path Following in 2D and 3D, *Proc. 44th IEEE Conference on Decision and Control*, pp. 627–634. ISSN: 0191-2216.

Caharija, W., Pettersen, K. Y., Gravdahl, J. T. and Børhaug, E. (2012). Path following of underactuated autonomous underwater vehicles in the presence of ocean currents, *Proc. 2012 IEEE 51st IEEE Conference on Decision and Control*, pp. 528–535.

Cai, X. and Queiroz, M. d. (2015). Adaptive Rigidity-Based Formation Control for Multirobotic Vehicles With Dynamics, *IEEE Transactions on Control Systems Technology* **23**(1): 389–396.

Chiaverini, S. (1997). Singularity-robust task-priority redundancy resolution for real-time kinematic control of robot manipulators, *IEEE Transactions on Robotics and Automation* **13**(3): 398–410.

Chiaverini, S., Oriolo, G. and Walker, I. D. (2008). Kinematically Redundant Manipulators, *in* B. Siciliano and O. Khatib (eds), *Springer Handbook of Robotics*, Springer, Berlin, Heidelberg, pp. 245–268.

Cui, R., Sam Ge, S., Voon Ee How, B. and Sang Choo, Y. (2010). Leader–follower formation control of underactuated autonomous underwater vehicles, *Ocean Engineering* **37**(17): 1491–1502.

Das, J., Py, F., Harvey, J. B., Ryan, J. P., Gellene, A., Graham, R., Caron, D. A., Rajan, K. and Sukhatme, G. S. (2015). Data-driven robotic sampling for marine ecosystem monitoring, *The International Journal of Robotics Research* **34**(12): 1435–1452.

Dowdeswell, J. A., Evans, J., Mugford, R., Griffiths, G., McPhail, S., Millard, N., Stevenson, P., Brandon, M. A., Banks, C., Heywood, K. J., Price, M. R., Dodd, P. A., Jenkins, A., Nicholls, K. W., Hayes, D., Abrahamsen, E. P., Tyler, P., Bett, B., Jones, D., Wadhams, P., Wilkinson, J. P., Stansfield, K. and Ackley, S. (2008). Autonomous underwater vehicles (AUVs) and investigations of the ice–ocean interface in Antarctic and Arctic waters, *Journal of Glaciology* **54**(187): 661–672.

DUNE: Unified Navigation Environment (n.d.). `https://github.com/LSTS/dune/`. Accessed 2023-01-10.

Eek, Å., Pettersen, K. Y., Ruud, E.-L. M. and Krogstad, T. R. (2021). Formation path following control of underactuated USVs, *European Journal of Control* **62**: 171–184.

Estrela da Silva, J., Terra, B., Martins, R. and Sousa, J. (2007). Modeling and simulation of the LAUV autonomous underwater vehicle, *Proc. 13th IEEE IFAC International Conference on Methods and Models in Automation and Robotics*.

Fossen, T. I. (2021). *Handbook of Marine Craft Hydrodynamics and Motion Control*, John Wiley & Sons.

Ghabcheloo, R., Aguiar, A. P., Pascoal, A., Silvestre, C., Kaminer, I. and Hespanha, J. (2006). Coordinated path-following control of multiple underactuated autonomous vehicles in the presence of communication failures, *Proc. 45th IEEE Conference on Decision and Control*, pp. 4345–4350.

Girejko, E. and Malinowska, A. B. (2019). Leader-following consensus for networks with single- and double-integrator dynamics, *Nonlinear Analysis: Hybrid Systems* **31**: 302–316.

Khalil, H. K. (2002). *Nonlinear Systems*, Prentice Hall.

Leonard, N. E., Paley, D. A., Lekien, F., Sepulchre, R., Fratantoni, D. M. and Davis, R. E. (2007). Collective Motion, Sensor Networks, and Ocean Sampling, *Proc. of the IEEE* **95**(1): 48–74.

Li, X., Wen, C. and Chen, C. (2021). Adaptive Formation Control of Networked Robotic Systems With Bearing-Only Measurements, *IEEE Transactions on Cybernetics* **51**(1): 199–209.

Lie, E. S., Matouš, J. and Pettersen, K. Y. (2023). Formation control of underactuated AUVs using the hand position concept, *Submitted to 62nd IEEE Conference on Decision and Control*. Preprint available in Appendix B.

Loría, A. and Panteley, E. (2005). 2 Cascaded Nonlinear Time-Varying Systems: Analysis and Design, *in* F. Lamnabhi-Lagarrigue, A. Loría and E. Panteley (eds), *Advanced Topics in Control Systems Theory*, Vol. 311, Springer London, London, pp. 23–64. Series Title: Lecture Notes in Control and Information Sciences.

MATLAB (2022). *MATLAB Symbolic Math Toolbox*, The MathWorks Inc., Natick, Massachusetts.
URL: *https://se.mathworks.com/products/symbolic.html*

Matouš, J., Paliotta, C., Pettersen, K. Y. and Varagnolo, D. (2023). Trajectory tracking and path following of underactuated AUVs using the hand position concept, *Submitted to IEEE Transactions on Control Systems Technology* . Preprint available at `https://www.dropbox.com/s/pwyople7rpykge9/SubmittedVersion.pdf?dl=0`.

Matouš, J., Pettersen, K. Y., Varagnolo, D. and Paliotta, C. (2023a). Formation path following using the distributed nsb algorithm, *Submitted to IEEE Transactions on Control Systems Technology* . Preprint available at `https://www.dropbox.com/s/3as1c4pmq90yavy/SubmittedVersion.pdf?dl=0`.

Matouš, J., Pettersen, K. Y., Varagnolo, D. and Paliotta, C. (2023b). Singularity-free Formation Path Following of Underactuated AUVs: Extended Version. arXiv:2210.14646 [cs, eess], *To appear in Proc. 22nd IFAC World Congress, July 2023.*

Miao, Z. and Wang, Y. (2019). Formation Control with Connectivity Maintenance for Double-Integrator Multi-Agent Systems, *Proc. 2019 Chinese Control Conference (CCC)*, pp. 5593–5598.

Mohammadi, M., Baradarannia, M. and Farzamnia, A. (2021). Leader-following consensus of nonlinear multi-agent systems based on position and velocity estimations, *Proc. 2021 7th International Conference on Control, Instrumentation and Automation (ICCIA)*, pp. 1–7.

Montañez-Molina, C., Pliego-Jiménez, J. and Cruz-Hernández, C. (2022). Formation control for robot networks with double integrator dynamics, *Proc. 2022 IEEE Conference on Control Technology and Applications (CCTA)*, pp. 589–594.

Monteiro, S. and Bicho, E. (2002). A dynamical systems approach to behavior-based formation control, *Proc. 2002 IEEE International Conference on Robotics and Automation*, pp. 2606–2611.

OceanScan - MST (2023). LAUV – Light Autonomous Underwater Vehicle.
URL: *https://www.oceanscan-mst.com/*

Paliotta, C., Lefeber, E., Pettersen, K. Y., Pinto, J., Costa, M. and de Figueiredo Borges de Sousa, J. T. (2019). Trajectory Tracking and Path Following for Underactuated Marine Vehicles, *IEEE Transactions on Control Systems Technology* **27**(4): 1423–1437.

Pereda, F. J., de Marina, H. G., Giron-Sierra, J. M. and Jimenez, J. (2011). Towards automatic oil spill confinement with Autonomous Marine Surface Vehicles, *OCEANS 2011 IEEE - Spain*.

Pettersen, K. Y. (2017). Lyapunov sufficient conditions for uniform semiglobal exponential stability, *Automatica* **78**: 97–102.

Pomet, J.-B., Thuilot, B., Bastin, G. and Campion, G. (1992). A hybrid strategy for the feedback stabilization of nonholonomic mobile robots, *Proc. 1992 IEEE International Conference on Robotics and Automation*, pp. 129–134 vol.1.

Ren, W., Beard, R. and Atkins, E. (2005). A survey of consensus problems in multi-agent coordination, *Proc. 2005, American Control Conference, 2005.*, pp. 1859–1864 vol. 3.

Restrepo, E., Matouš, J. and Pettersen, K. Y. (2022). Tracking-in-Formation of Multiple Autonomous Marine Vehicles under Proximity and Collision-Avoidance Constraints, *Proc. 2022 European Control Conference*, pp. 930–937.

Siciliano, B., Sciavicco, L., Villani, L. and Oriolo, G. (2009). Differential Kinematics and Statics, *Robotics: Modelling, Planning and Control*, Advanced Textbooks in Control and Signal Processing, Springer, London, pp. 105–160.

Skjetne, R., Moi, S. and Fossen, T. (2002). Nonlinear formation control of marine craft, *Proc. 41st IEEE Conference on Decision and Control, 2002.*, pp. 1699–1704.

Soorki, M., Talebi, H. and Nikravesh, S. (2011). A robust dynamic leader-follower formation control with active obstacle avoidance, *Proc. 2011 IEEE International Conference on Systems, Man, and Cybernetics*, pp. 1932–1937.

Sousa, A., Madureira, L., Coelho, J., Pinto, J., Pereira, J., Borges Sousa, J. and Dias, P. (2012). LAUV: The Man-Portable Autonomous Underwater Vehicle, *IFAC Proceedings Volumes* **45**(5): 268–274.

The MathWorks Inc. (2022). *MATLAB*, Natick, Massachusetts.
URL: *https://se.mathworks.com/products/symbolic.html*

Wang, Y., Yan, W. and Yan, W. (2009). A leader-follower formation control strategy for AUVs based on line-of-sight guidance, *Proc. 2009 International Conference on Mechatronics and Automation*, pp. 4863–4867.

Wynn, R. B., Huvenne, V. A. I., Le Bas, T. P., Murton, B. J., Connelly, D. P., Bett, B. J., Ruhl, H. A., Morris, K. J., Peakall, J., Parsons, D. R., Sumner, E. J., Darby, S. E., Dorrell, R. M. and Hunt, J. E. (2014). Autonomous Underwater Vehicles (AUVs): Their past, present and future contributions to the advancement of marine geoscience, *Marine Geology* **352**: 451–468.

Zelazo, D., Rahmani, A. and Mesbahi, M. (2007). Agreement via the edge laplacian, *Proc. 2007 46th IEEE Conference on Decision and Control*, pp. 2309–2314.

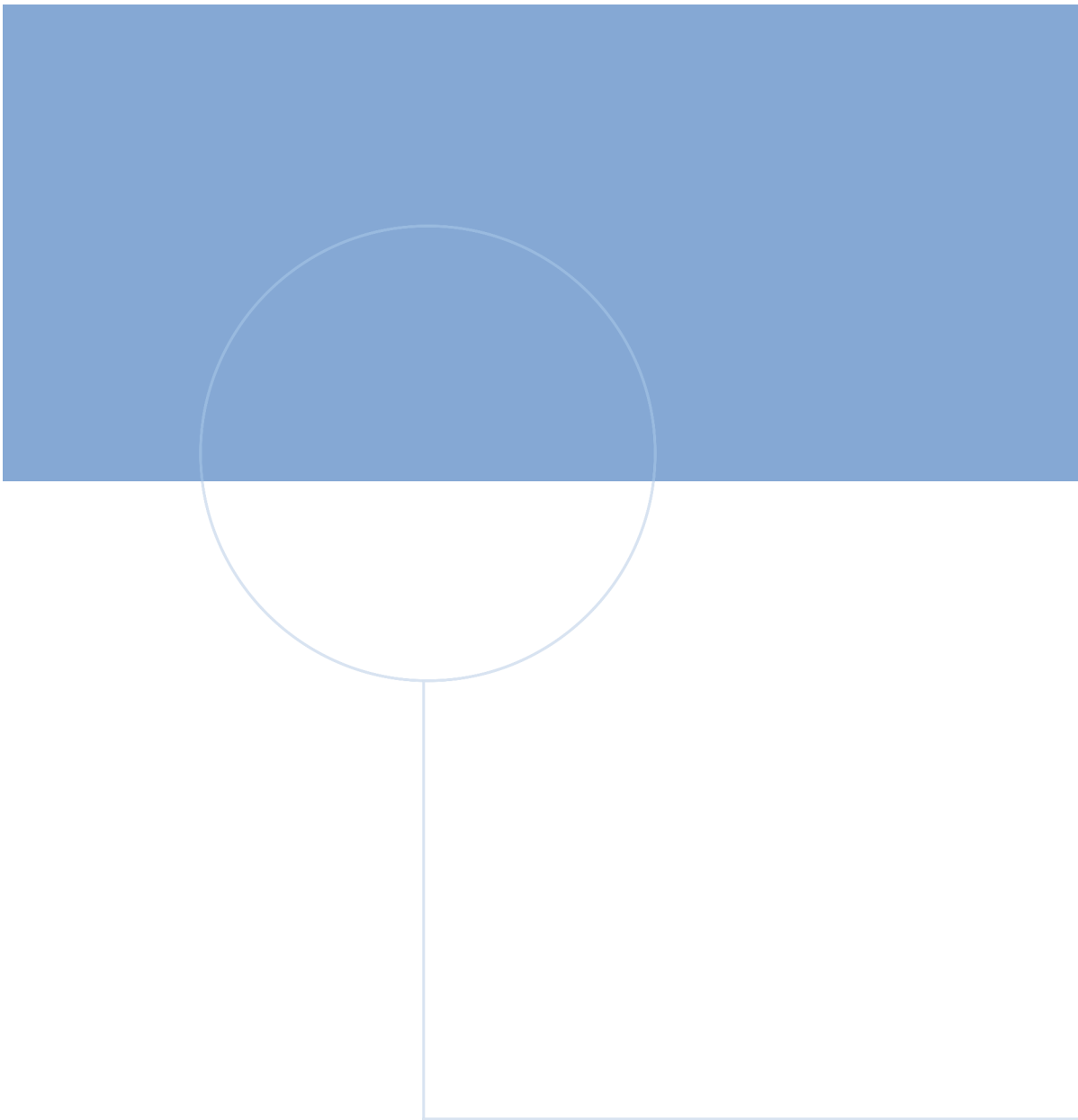

NTNU

Norwegian University of
Science and Technology